

2008

Two dimensional photonic crystals with anisotropic constituents and their propagation characteristics

Mohammad Masud Siraj
University of Dayton

Follow this and additional works at: https://ecommons.udayton.edu/graduate_theses

Recommended Citation

Siraj, Mohammad Masud, "Two dimensional photonic crystals with anisotropic constituents and their propagation characteristics" (2008). *Graduate Theses and Dissertations*. 5633.
https://ecommons.udayton.edu/graduate_theses/5633

This Dissertation is brought to you for free and open access by the Theses and Dissertations at eCommons. It has been accepted for inclusion in Graduate Theses and Dissertations by an authorized administrator of eCommons. For more information, please contact mschlange1@udayton.edu, ecommons@udayton.edu.

**TWO DIMENSIONAL PHOTONIC CRYSTALS WITH
ANISOTROPIC CONSTITUENTS AND THEIR PROPAGATION
CHARACTERISTICS**

Dissertation

Submitted to

The School of Engineering of the

UNIVERSITY OF DAYTON

in Partial Fulfillment of the Requirements for

The Degree of

Doctor of Philosophy in Electro-optics

by

Mohammad Masud Siraj

UNIVERSITY OF DAYTON

Dayton , Ohio

December, 2008

TWO DIMENSIONAL PHOTONIC CRYSTALS WITH ANISOTROPIC CONSTITUENTS AND THEIR PROPAGATION CHARACTERISTICS

APPROVED BY :



Joseph W. Haus, Ph.D.

Professor and Director

Electro-Optics Graduate Program

Committee Chairman

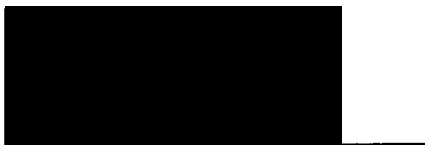


Andrew Sarangan, Ph.D.

Associate Professor

Electro-Optics Graduate Program

Committee Member




Qiwen Zhan, Ph.D.

Associate Professor

Electro-Optics Graduate Program

Committee Member

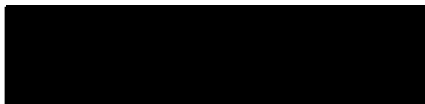


Paul Elie, Ph.D.

Professor

Department of Mathematics

Committee Member



Malcolm Daniels, Ph.D.

Associate Dean

Graduate Studies

School of Engineering



Joseph E. Saliba, Ph.D.

Dean

School of Engineering

ABSTRACT

TWO DIMENSIONAL PHOTONIC CRYSTALS WITH ANISOTROPIC CONSTITUENTS AND THEIR PROPAGATION CHARACTERISTICS

Name : Siraj, Mohammad Masud

University of Dayton , 2008

Advisor : Dr. Joseph W. Haus

Photonic crystals (PhCs) possess unique dispersion properties that can be exploited to enable novel photonic applications. These properties can also be used to significantly improve the performance of existing photonic devices. Many applications of PhCs such as waveguides, PC fibers and photonic cavities have been explored by using the presence of a photonic bandgap over a desired frequency range with a defect incorporated in the structure to allow only a desired mode to propagate. This strategy often requires a large index contrast between materials to create the band gap in the first place, which limits the materials that can be used for the photonic devices. On the other hand, many phenomena such as negative refraction, superprism, super-resolution, and slow light have been

demonstrated based on unique spatial and temporal dispersion properties of a PhC and they are often observable with materials having a low index contrast.

In my research we investigate self-collimation, another dispersion-related phenomenon of PhCs, that is manifested to some degree in all PhCs. In free space or homogeneous materials propagating electromagnetic waves spread due to diffraction effects, but a PhC in the region of self-collimation has essentially no diffraction and input beams spread over a range of input angles are collimated into a single direction. The phenomenon of beam-like propagation without divergence is important for many applications, including optical interconnects in an integrated circuit. Self-collimation provides a solution to beam control that does not require additional fabrication steps and can be used in conjunction with additional effects to further tailor the application needs.

We develop a process to investigate the range of input angles and the degree of collimation of the beam inside the photonic crystal composed of anisotropic constituents. The optical properties of a photobleached 4-dimethylamino-N-methyl-4-stilbazolium-tosylate (DAST) crystal are used in our model to demonstrate the efficacy of the self-collimation features. In DAST we identified conditions where the divergence angle over a span of incident angles of 40 degrees can be less than 1 degree and the transmission remains high over the entire span of angles.

To my beloved wife, Shimu and my daughter, Rayya and son, Ayan.

ACKNOWLEDGEMENTS

I would like to thank my advisor Dr. Joseph W. Haus for his supervision and support and for providing me with the opportunity and resources to complete my Ph.D. He is very knowledgeable, careful, accessible and patient in helping me with all the details in my research. His passion for science and technology has deeply influenced me. I am fortunate to have had him as my advisor.

I would also like to thank my committee members Dr. Andrew Sarangan, Dr. Qiwen Zhan and Dr. Paul Elie for serving on my advisory committee. They have made a lot effort in helping me from the proposal work to final defense in spite of their busy schedule. I would also like to express my deep gratitude to University of Dayton summer fellowship, Department of Physics and Electro-optics graduate program for funding my research. In addition, I would like to express my special thanks to Dr. Peter Powers .

I had like to acknowledge the friends I have made in University of Dayton for their moral support, in particular Dr. Anup Panday, Dr. Cong Deng, Dr. Aziz Mahfoud, Dr. Todd Smith, Dr. Mohammad Saleh, Zasim Mojumder, Nkorni Katte and many others who each in their own way have helped keep me grounded and have made my stay at UD an pleasurable experience.

Last but not least I would like to thank my wife, Naushin Reza, who has been giving me continuous support during the last five years and my parents , Md. Siraj Uddin and

Feroza Akhtar for nurturing my intellectual curiosity throughout the years , for the education they provided me with and for laying the foundation that eventually led me to where I am today.

Mohammad Masud Siraj

December, 2008

Dayton, Ohio

TABLE OF CONTENTS

Abstract	iii
Dedication.....	v
Acknowledgements	vi
List of Figures.....	xi
List of Tables.....	xv
List of Publications.....	xvi
Glossary of Acronyms	xvii
Chapters	
1. Introduction	1
1.1 Types of Photonic Crystals	11
1.2 Applications of Photonic Crystals	12
1.3 Outline	13
2. The study of Photonic Crystals	15
2.1 Introduction to the numerical methods.....	15
2.2 Basic Concepts behind the theory of band Structure	16
2.3 The Reciprocal Lattice and the Brillouin zone	16
2.4 The plane wave expansion method (PWM)	18
2.4.1 Two-Dimensional PWM	23
2.5 Finite Difference Time Domain Method	26

2.6 Finite Element Method(FEM)	30
3. Light Propagation in Photonic crystal	33
3.1 Origin of self-collimation	41
4. Self collimated beam in Square and Triangular isotropic photonic crystal	44
4.1 Dielectric circular rods in isotropic medium	44
4.2 .1 Photonic band structure diagram and EFS plots for 2D square lattice'	45
4.2.2 FE Modeling Results	52
4.3.1 Photonic band structure diagram and EFS plots for 2D Trinagular lattice	55
4.3.2 FE Modeling Results	63
5. Self-collimation in Photonic crystal with anisotropic constituents....	67
5.1 Structure and Properties of DAST Crystals	68
5.2 Modeling	71
5.3 Results	72
5.4 Simulation Results	77
6. Self-collimation Optimization by Rotating Crystal Axes.....	83
6.1. Theory and Formalism	83
6.2 Modeling	88
6.3 Transmission Spectra	90
6.4 Shape of EFS after rotation	91
6.5. Radius dependency	94

6.6 Effect of anisotropy	96
6.7 Simulation Result	97
7. Conclusion and Future Direction	102
7.1 Future Research Direction.....	104
References	105
Appendix.....	114

LIST OF FIGURES

1.1.	Energy diagrams for a free electron, and lattice	5
1.2.	Schematic of a 1D Photonic crystal.....	6
1.3.	Band structure of 1D Photonic crystal by variation of dielectric contrast..	7
1.4.	Schematic of a reciprocal space for a square lattice.....	9
1.5.	Schematic illustration of one-dimensional (1D), two-dimensional (2D) and three dimensional(3D) photonic crystals.....	12
2.1.	First Brillouin zone of the square lattice and the irreducible Brillouin zone for circular rods with isotropic dielectrics.....	18
2.2.	Schematic of Yee Lattice and the position of EM field in the Yee cell.....	28
3.1.	Diagram of wave vector for light incident from air ($n = 1$) to a homogeneous isotropic dielectric material.....	35
3.2.	Diagram of wave vector for light incident from air ($n = 1$) to diffraction grating	37
3.3.	Schematic of Photonic band structure of TM modes for a 2D photonic crystal made from dielectric holes in air with $r = 0.35a$ and refractive index 3.6 arranged in a triangular lattice with a lattice constant a	39
3.4.	EFS plot of TE modes for a 2D photonic crystal made from dielectric holes in air with $r = 0.35a$ and refractive index 3.6 arranged in a triangular lattice with a lattice constant a	40

3.5.	A schematic illustration of the self-collimating phenomena together with the divergence and convergence case	42
4.1.	Cross-section of the 2D square lattice composed of circular cylinders and corresponding First Brillouin zone.....	46
4.2.	3D view of the equi-frequency surface for the 1 st and 2 nd band of the Square lattice with isotropic materials. The refractive indices are $n_{\text{rod}} = 1.64$ and $n_{\text{host}} = 2.55$ and the radius of the rods $r = 0.1a$	47
4.3.	Contour representation of the equi-frequency surface for the 1 st and 2 nd band of the square lattice with isotropic materials. The refractive indices are $n_{\text{rod}} = 1.64$ and $n_{\text{host}} = 2.55$ and the radius of the rods $r = 0.1a$	48
4.4.	Graph shows the Deviation of the group velocity from normal for the scaled cylinder radius versus input angles of those where the deviation from Snell's law will be minimal.....	50
4.5.	Contour representation of the equi-frequency surface for the 1 st and 2 nd band of the square lattice with isotropic materials. The refractive indices are $n_{\text{rod}} = 1.64$ and $n_{\text{host}} = 2.55$ and the radius of the rods $r = 0.4a$	51
4.6.	Power spectrum through the square PhC from air with the incident angle of $0^0, 10^0, 12^0, 14^0$, and 15^0	55
4.7.	Cross-section of the 2D triangular lattice composed of circular cylinders and corresponding First Brillouin zone.....	56
4.8.	3D view of the equi-frequency surface for the 1 st , 2 nd and 3 rd band of the triangular lattice with isotropic materials. The refractive indices are $n_{\text{rod}} = 1.64$ and $n_{\text{host}} = 2.55$ and the radius of the rods are $r = 0.1a$	57
4.9.	Contour representation of the EFS surface for the 1 st , 2 nd and 3 rd band of the triangular lattice with isotropic materials. The refractive indices are $n_{\text{rod}} = 1.64$ and $n_{\text{host}} = 2.55$ and the radius of the rods $r = 0.1a$	58
4.10.	Contour representation of the equi-frequency surface for the 2 nd band of the triangular lattice with isotropic materials of radii, $r, 0.2, 0.3, 0.4$ and 0.5 micron . The refractive indices are $n_{\text{rod}} = 1.64$ and $n_{\text{host}} = 2.55$ and the radius of the rods $r = 0.4a$	62
4.11.	Power flow through the Triangular PhC from air with the incident angle of $0^0, 10^0, 12^0, 14^0$, and 15^0	65
5.1.	Showing the crystallographic axes and the dielectric principal axes in DAST.....	69

5.2.	EFS Contour of the Second band of the square lattice of anisotropic constituents. The index n_l is fixed at 2.55 and the values of the n_2 are (1.78 1.9, 2.2) for $r=0.2a$	74
5.3	Curve showing the maximum of the angular deviation of the group velocity for the case $r=0.15a$	75
5.4.	The maximum angular deviation of the group velocity versus the incident angle at different anisotropy. Cylinder radii are $r=0.2a$	76
5.5.	Input angle for the maximum deviation of the group velocity from normal versus the scaled cylinder radius.....	77
5.6 .	Power flow through the square PhC of anisotropic constituents from air with the incident angle of 0° . The index n_l is 2.55 and n_2 is 1.78 for $r =0.4a$	78
5.7 .	Normalized power in different region of the square PhC of anisotropic constituents from air with the incident angle of 0° . The index n_l is 2.55 and n_2 is 1.78 for $r =0.4a$	79
5.8.	Power flow through the square PhC of anisotropic constituents from air with the incident angle of $10^\circ, 15^\circ, 18^\circ, 20^\circ$ and 22° . The index n_l is 2.55 and n_2 is 1.78 for $r =0.4a$	80
5.9.	Normalized power in different region of the square PhC of anisotropic constituents from air with the incident angle of 22° . The index n_l is 2.55 and n_2 is 1.78 for $r =0.4a$	82
6.1.	Schematic of the rotation axes and the definition of the angles.....	85
6.2.	Band structure of the 2D DAST crystal of anisotropic cylinders arrayed in a square lattice of anisotropic background and $\alpha = 0^\circ$, $r=0.4a$, $n_{lb}=2.55$, $n_{2b}=1.78$, $n_{lc}=1.64$, $n_{2c} = 1.62$	89
6.3.	Band structure of the 2D DAST crystal of anisotropic cylinders arrayed in a square lattice of anisotropic background and $\alpha = 30^\circ$, $r=0.4a$, $n_{lb}=2.55$, $n_{2b}=1.78$, $n_{lc}=1.64$, $n_{2c} = 1.62$	89
6.4.	Simulated Transmission spectra for the TM mode in the ΓX direction in a 2D square DAST crystal of $\alpha = 30^\circ$, $r=0.4a$, $n_{lb}=2.55$, $n_{2b}=1.78$, $n_{lc}=1.64$, $n_{2c} = 1.62$	91
6.5.	EFS for the second and third band with rotation angles of 0° and 10° . Index parameters are $r=0.1a$, $n_{lb}=2.55$, $n_{2b}=1.78$, $n_{lc}=1.64$, $n_{2c} = 1.62$...	92

6.6.	EFS for the second and third band with rotation angles of 30^0 . Index parameters are $r=0.1a$, $n_{1b}=2.55$, $n_{2b}=1.78$, $n_{1c}=1.64$, $n_{2c}=1.62...$	93
6.7.	Graph represents the intensity profile with different radii. Index parameters are $n_{1b}=2.55$, $n_{2b}=1.78$, $n_{1c}=1.64$, $n_{2c}=1.62.....$	94
6.8.	Graph represents of deviation angles versus input angle for several radii. Rotation angle is 30^0 degrees. Index parameters are $n_{1b}=2.55$, $n_{2b}=1.78$, $n_{1c}=1.64$, $n_{2c}=1.62.....$	95
6.9.	Graph represents the intensity profile of the output beam for various anisotropy. Index parameters are $r=0.1a$, $n_{1b}=2.55$, $n_{2b}=1.78$, $n_{1c}=1.64$, $n_{2c}=1.62.....$	96
6.10.	Graph represents the deviation angles versus input angle for three anisotropy parameters. Rotation angle is 30 degrees. Index parameters are $r=0.1a$, $n_{1b}=2.55$, $n_{2b}=1.78$, $n_{1c}=1.64$, $n_{2c}=1.62.....$	97
6.11.	EFS for the second band with rotation angles of 30^0 . Index parameters are $r=0.4a$, $n_{1b}=2.55$, $n_{2b}=1.78$, $n_{1c}=1.64$, $n_{2c}=1.62.....$	98
6.12.	Schematic of the simulation result of the power flow inside the crystal of normalized frequency, $a/\lambda = 0.4$ for incident angle 0^0 , 5^0 , 10^0 , 15^0 , 20^0 , 25^0 , 30^0 , 35^0 and 40^0 . Rotation angle 30^0 degrees. Index parameters are $r=0.4a$, $n_{1b}=2.55$, $n_{2b}=1.78$, $n_{1c}=1.64$, $n_{2c}=1.62.....$	99
6.13.	Normalized power in different region of the square PhC of anisotropic constituents from air with the incident angle, θ_{in} , of 35^0 and 40^0 . The index parameters are $n_1=2.55$, $n_2=1.78$, $\alpha=30^0$ and $r=0.4a...$	101

LIST OF TABLES

5.1	Principal refractive indexes for DAST.....	70
-----	--	----

LIST OF PUBLICATIONS

1. J. W. Haus, M. Siraj, P. Prasad, and P. Markowicz, "Self-collimation in photonic crystals with anisotropic constituents," *Chin. Opt. Lett.* **5**, 527-530 (2007)
2. T. Yamada, M. Siraj, and P. H. Taylor, J. Peng, X. Hu and P. Marshall, "Rate Coefficients and Mechanistic Analysis for Reaction of OH with Vinyl Chloride between 292 and 730 K," *J. Phys. Chem. A*, **105**, 9436, 2001.
3. T. Yamada, A. El-Sinawi, M. Siraj, and P. H. Taylor, J. Peng, X. Hu and P. Marshall, "Rate Coefficients and Mechanistic Analysis for Reaction of OH with 1,1 Dichloroethene and trans-1,2 Dichloroethene Over an Extended Temperature Range," *J. Phys. Chem. A*, **105**, 7588, 2001.

GLOSSARY OF ACRONYMS

EFS	Equi- frequency surface
FDTD	Finite difference time domain method
FEM	Finite element method
PBG	Photonic Band Gap
PhC	Photonic crystal
PWM	Plane wave method
TE	Transverse electric
TM	Transverse magnetic

CHAPTER I

INTRODUCTION

Photonic crystals (PhC) have attracted a lot of interest in the past few years due to their ability to control radiation field and light propagation characteristics. A PhC is defined as a crystal such that the dielectric constant (ϵ) periodically varies spatially in specific directions. The engineering of electromagnetic (EM) modes at optical frequencies in multidimensional synthetically periodic structures was pointed out and demonstrated theoretically in two independent papers by E. Yablonovitch [1] and S. John in 1987 [2]. Yablonovitch's primary goal was to restrict the spontaneous-emission rates to only those electromagnetic modes which are absolutely necessary in the semiconductor lasers to guide the light and suppressed all spontaneous emission to additional directions or modes, where radiation field would lead to excessive losses. Motivated by the one-dimensional periodic dielectric layer that gives rise to band gap for EM waves propagating perpendicular to the patterned layers, increasing the periodicity to three dimensions may provide band gap in all directions. The density of states (DOS) is zero within the band gap and the wave vector k is evanescent. Since the spontaneous emission rates are proportional to the DOS, it is possible to inhibit the spontaneous emission by using a photonic band gap. Meanwhile, John suggested that new phenomena can be

observed by using a PhC , which includes localization of light. He argued that 3-D photonic superlattices with moderate disorder , two photon mobility edges separate high- and low-frequency extended states from an intermediate frequency pseudogap of localized states arising from remnant geometric Bragg resonances. Since 1987 many scientists started their own research work in this field. As proven later both theoretically and experimentally, these periodic structures, called photonic crystals (PhC), have the ability to prohibit the propagation of light, or allow it only in certain directions at certain frequencies, or localize light in specified areas.

One difficulty in the early studies was to create actual photonic crystal at optical wavelength scales to overcome the fabrication challenges. By 1991, Yablonovitch had demonstrated the first three-dimensional photonic band-gap in the microwave regime [3]. At optical wavelengths, Krauss first demonstrated a two-dimensional photonic crystal in 1996 [4].

Most of the earlier works on PhCs concentrated on the band gap based applications, one of the unique properties of PhCs [5-9]. I explain the origin of PhC band gaps later in this chapter. The majority of the recent papers engineer the propagation characteristics in the PhC by introducing point and line defects in the lattice. The proposed applications include: compact optical spectrometers [10], cavity resonators [11], channel drop/add filters [12], optical switches [13] , optical waveguides [14], parametric wavelength conversion, and coupled waveguide applications [15].

Due to the complex spatial and spectral dispersion properties that photonic crystals exhibited outside the band gap region little interest was shown for applications based on the behavior of modes outside the band gap. Within those regions, multiple eigenmodes

might exist, and sometimes overlap, showing various degrees of degeneracy at certain wave vectors or frequencies, and hence working within those regions was difficult and not favored by the majority of researchers in the photonic crystal community [16]. In 1998, Kosaka *et al* [17] observed the superprism effect by utilizing the dispersion surfaces of the PhC outside the band gap region. In 1999, Kosaka *et al* observed another outside-gap phenomenon exhibited by a 3D PhC showing collimated light propagation insensitive to the divergence of the incident beam [18]. This phenomenon was called self-collimation. In free space or homogeneous materials propagating electromagnetic waves spread due to diffraction effects but a PhC in the region of self-collimation has reduced diffraction and input beams spread over a range of input angles are collimated into a single direction. The phenomenon of beam like propagation without divergence is important to many applications, including optical interconnects in an integrated circuit [19]. It removed the need to build optical circuits with confining side walls and simplified the processing requirements. Witzens *et al* [20] theoretically investigated self-collimation in planar PhCs; later, Wu *et al* [21] experimentally demonstrated the phenomenon. They also combined the self-collimating phenomenon with the superprism phenomenon to make a beam deflection device. Later, several other groups studied various aspects of self-collimation in PhC structures [22–25].

In our study, we investigate the self-collimation which is manifested to some degree in all PhCs. We study PhC with mixtures of anisotropic materials; both the inclusions and the background materials may be anisotropic. Anisotropic materials in PhCs were first studied by Zabel and Stroud[26] in 1993. The authors demonstrated that the anisotropy can reduce the band gap of PhC by breaking the degeneracies of bands with different

polarizations. They even found a case where sufficient anisotropy would close the gap altogether. In 1998, Li *et al.* reported a large absolute band gap in two dimensional (2D) PhCs made of anisotropic materials [27,28]. Recently, Alagappan et al. extensively explored anisotropic materials and among other results, reported the decoupling of the two polarizations on 2D PhC made of anisotropic materials [29]. But none of these above works use the full anisotropic materials .

The basic concept is that photonic crystals can be engineered to affect photons in analogy to how semiconductor crystals can affect electrons, i.e. they create a situation whereby photons in a certain energy range cannot travel through the crystal and are reflected when impinging onto the crystal or are not allowed to propagate at all when generated inside it. [28,29,30]. A crystal is a periodic arrangement of atom or molecules; that is , a crystal lattice results when a small, basic building block of atoms or molecules is repeated in space. A crystal therefore presents a periodic potential to an electron propagating through it as shown in figure 1.1 [31], and the geometry of the crystal dictates many of the conduction properties of the crystal. Under specific conditions the lattice introduces gaps in the electron energy band structure in the crystal that forbid the electrons of certain energies to propagate in the crystal. Such waves are evanescent and the materials can be used as tunneling barriers for energies in the band gap region. The electron band gap is a separator between the conduction and the valance bands, when the lower band is filled with electrons and the conduction band is empty or only lightly populated. The electron band gap depends on the lattice potential and if the lattice potential is strong enough , the gap might extends over all possible directions, resulting in a complete band gap.

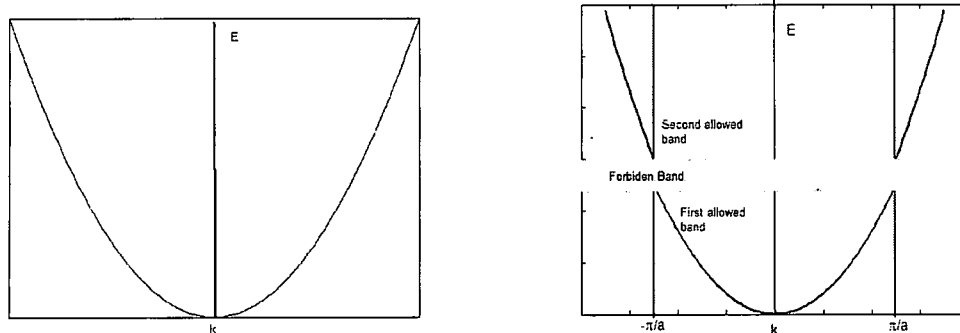


Figure 1.1: Energy diagrams (a) for a one dimensional model for a free electron, and (b) for an electron propagating through an atomic lattice a forbidden band opens up and electrons do not appear with those energies [31].

The corresponding optical material is called a photonic crystal, in which the periodic ‘potential’ is due to a lattice of macroscopic dielectric media instead of atoms or molecules. If the dielectric constants of the materials in the crystal are different enough, and the absorption of light by the material is minimal, then scattering and diffraction in this complex periodic material can produce many of the same phenomena for photons (light modes) as the atomic potential does for electrons. Frequency bands in which the EM waves are allowed to propagate freely through the structure depends on the dispersion diagram $[\omega(k) \text{ vs. } k]$. In a uniform medium, the speed of light is reduced by the index of refraction. The frequency spectrum is just the light line given by

$$\omega(k) = \frac{ck}{\sqrt{\epsilon}} \quad 1.1$$

However, for some ranges of frequencies in a periodic medium there may be no propagating modes in all directions, and such frequency ranges are called photonic band gaps (PBGs). Since the wave vector in that case has an imaginary component, the wave

amplitude decays exponentially. The physical origin of the PBG can be explained as follows. For simplicity we consider the simplest possible photonic crystal, shown in figure 1.2, consists of alternating layers of material with different dielectric constants with layer spacing of a . This structure is a stack of alternating high- and low-dielectric layers with indices n_H and n_L , respectively. Dielectric constant therefore periodically varies along the z -direction.

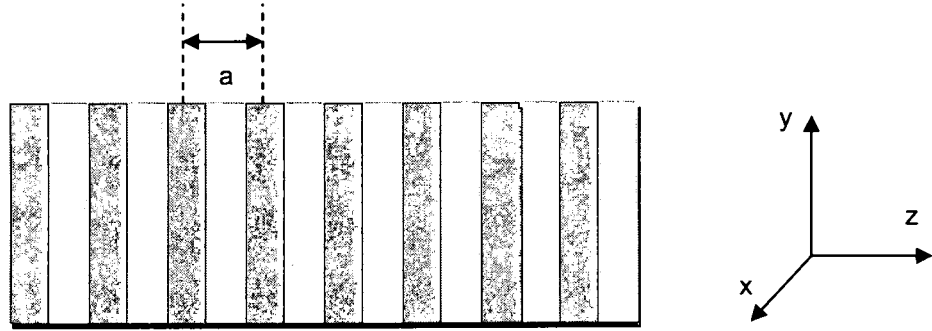
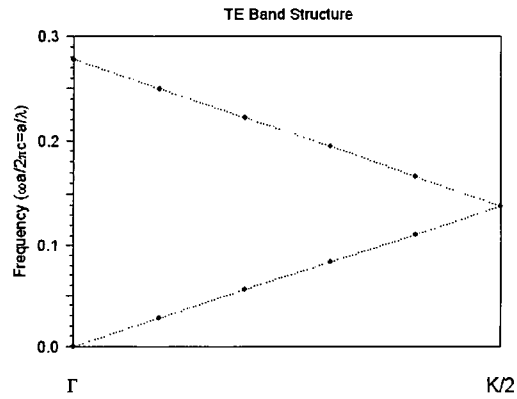
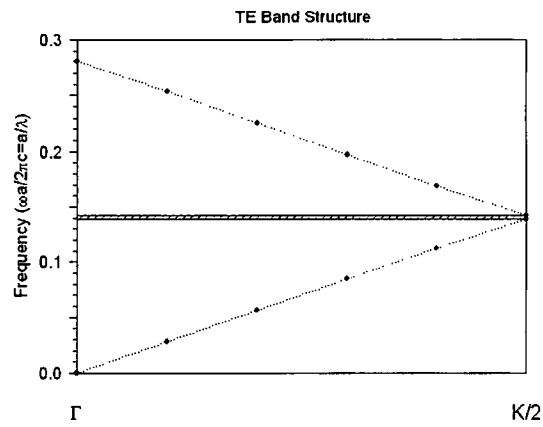


Figure 1.2 : 1D photonic crystal

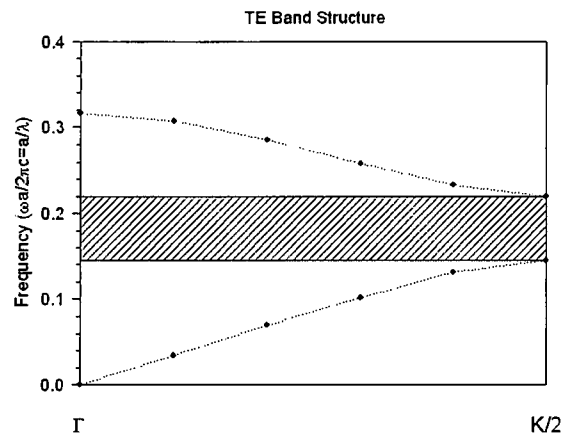
Now consider a plane wave in the form $\exp(ik \cdot r)$ propagate entirely in the z -direction crossing the layers of dielectrics at normal incidence. Now this wave is modulated by the periodic function of the lattice $\varepsilon(z) = \varepsilon(z + a)$. In this case, there is no wave vector component in the x - y plane. In figure 1.3(a-c), plots of $\omega(k)$ for three different multilayer films. First figure 1.3a is for the homogeneous medium that means no variation of dielectric constants but artificially assigned a periodicity of a . Then second plot is for a structure of alternating dielectric constants. Since k repeat itself outside the Brillouin zone, the lines fold back into the zone when they reach the edges.



(a)



(b)



(c)

Figure 1.3 :Band structure in the reduced zone scheme for (a) homogeneous medium, 1D PhC of (b)low dielectric contrast and (c) high dielectric contrast.

In the periodic medium with alternating dielectric constants, low frequency modes concentrate their energy in the high dielectric constant regions and the high frequency modes concentrate their energy in the low dielectric constant regions [28]. Therefore there is a frequency difference between the two cases which creates a gap between these frequencies [Hatched region in figure 1.3(b)] . In this case a gap mode exists, regardless of k , in the one-dimensional crystal. This gap is called a photonic band gap, but it has also been called a stop band for multi-layer periodic materials. Last plot of figure 1.3 is also for the structure of alternating dielectric constant but has a much higher dielectric contrast ratio (i.e. the ratio of the two dielectric constituents) compared to the that of center plot. By comparing these two plots it is obvious that gap widens as the dielectric contrast increased.

Like the 1D crystals, the dispersion relation of a 2D crystal with a periodic spatial variation of the dielectric constant can be well-represented by the folding of the dispersion line of the uniform material , $\omega = vk$, into the first Brillouin zone, where v is the phase velocity. The fact is that all wave vectors are not parallel to each other in 2D PhCs, which makes a significant difference between 1D and higher dimensional PhCs. As an example, figure 1.4 , shows the reciprocal lattice space of a 2D square lattice. The lattice constant is denoted by a as before. The first Brillouin zone is surrounded by a dashed line in the figure.

The elementary lattice vectors are

$$a_1 = (a, 0) \quad \text{and} \quad a_2 = (0, a) ,$$

and the elementary reciprocal lattice vectors are

$$b_1 = (2\pi/a, 0) \quad \text{and} \quad b_2 = (0, 2\pi/a) ,$$

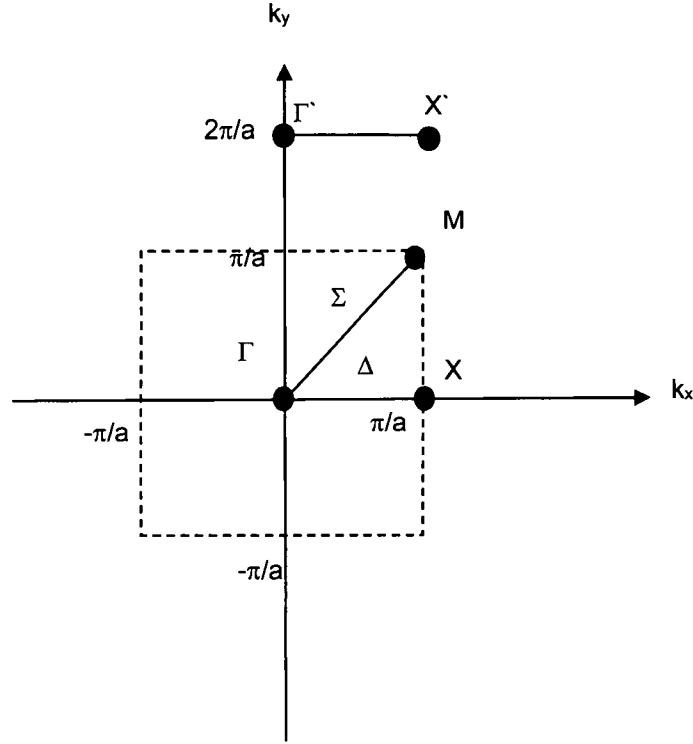


Figure 1.4 : Reciprocal lattice space of the 2D square photonic crystal with the lattice constant a . The first Brillouin zone is surrounded by a dashed line [28] .

Those wave vectors that differ from each other by the sum of a multiple of b_1 and that of b_2 should be regarded as the same. There are three high symmetry points in the first Brillouin zone, i.e., the Γ point, $(0,0)$, the X point, $(\pi/a, 0)$ and the M point, $(\pi/a, \pi/a)$. The wave vectors between Γ and X points are called the Δ points and the points between Γ and M are called the Σ points.

Now, an anomalously small group velocity occurs when the original wave vector in the uniform material is not parallel to either b_1 or b_2 . The wave vectors between Γ' and X' are [28]

$$k' = \left(k_x, 2\pi/a \right), \quad 0 \leq k_x \leq \pi/a .$$

The original dispersion relation is given by

$$\omega = v|k'| = v\sqrt{k_x^2 + \left(2\pi/a\right)^2}, \quad 1.2$$

and this should also be regarded as a good approximation to the rigorous dispersion relation of the photonic crystal for the corresponding wave vectors k in the first Brillouin zone $K=(k_x,0)$.

In next chapter, I will show how to calculate the wavefunctions of this radiation modes by using different numerical techniques. There are several parameters that characterize the radiation waves. One of them is the wave velocity. Waves have three different kinds of velocities, i.e., the phase velocity, the group velocity, and the energy velocity. These velocities may be nearly equal to each other in uniform materials with dielectric constants which are real and independent of frequency.

Phase Velocity is defined as the velocity of the propagation of an equiphase surface. In multidimensional space the phase velocity, that is the smallest speed at which the wave front propagates in the direction of the wave vector k , is defined as [29]

$$v_p = \frac{\omega}{k}. \quad 1.3$$

Now the equiphase surface can be defined without ambiguity for plane waves and spherical waves but it cannot be defined rigorously in the photonic crystal since its eigenfunction is a superposition of plane waves as I will show in next chapter. Therefore the phase velocity cannot be defined appropriately in the photonic crystal.

On the other hand, the group velocity, which is the velocity of the propagation of a

wave packet, can be defined :

$$\vec{v}_g = \frac{\partial \omega}{\partial \vec{k}}. \quad 1.4$$

The energy velocity is defined as the velocity of the propagation of the electromagnetic energy. The propagation of electromagnetic energy is described by Poynting's vector. For linear wave propagation in a homogeneous, non-dissipative media, it can be proven that the group velocity and energy velocity are equal [29,32] . The group velocity thus identifies the direction and the speed of energy propagation. This is not true in general, since in regions of anomalous dispersion the magnitude of the group velocity may become greater than the speed of light or may become negative [33-37].

1.1 Types of Photonic Crystals

Photonic crystals are classified into three simple categories, that is one dimensional (1D), two-dimensional, and three-dimensional (3D) crystals according to the dimensionality of the periodicity. [38] In the case where the variation is along one direction, it is called a 1D PhC. First figure of Fig 1.5 is shown schematics of the 1D PhC. 2D and 3D PhCs are defined corresponding to the respective cases where ϵ varies along two and three independent directions . Second and third figures of figure 1.5 are shown the 2D and 3D PhC respectively.

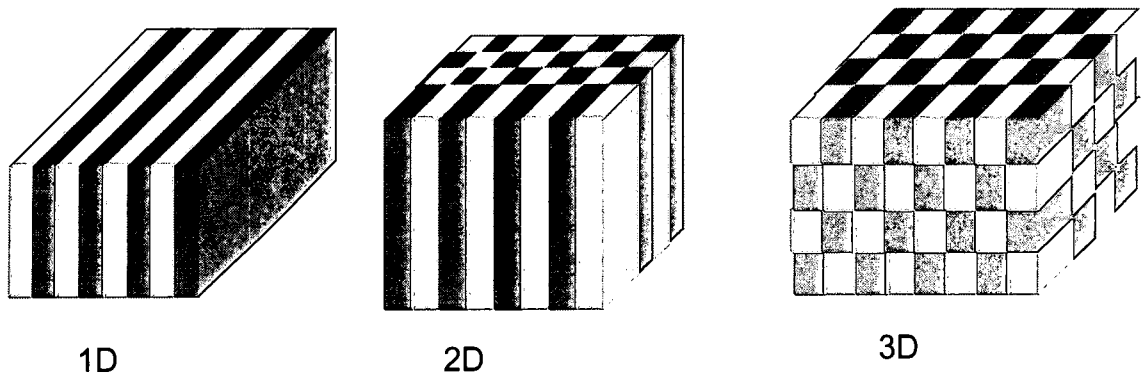


Figure 1.5 : Schematic illustration of one-dimensional (1D), two-dimensional (2D), and three-dimensional (3D) photonic crystals.

1.2 Applications of Photonic Crystals

Because of their unique properties, PhCs are very attractive for exploring new physical phenomena and developing novel and important devices in the field of optoelectronics as well. When the frequency falls in a photonic band gap, a photonic crystal becomes a perfect "optical insulator," which can be utilized to build ultra-compact mirrors, cavities, and waveguides [39-42]. On the other hand, when the photon frequency falls in a photonic band, a photonic crystal may behave like an "optical conductor," which can be utilized in optical communication [43], beam steering [44] and other applications.

In our research we concentrate on beam guiding. One of the unique properties of the PhCs is their ability to deflect the light. Under certain conditions PhCs exhibit an extraordinary large spatial dispersion in their photonic band structures which is known as the superprism phenomenon. [45-48]. The superprism effect can be used to develop a light control device where the deflection properties of the optical beam like scanners, displays and spatial optical switches[47]. Kosaka et al demonstrated in a three-

dimensional “autocloned” PhC that the angle between two beams is two orders of magnitude larger than that achieved with conventional prisms or gratings [48].

1.3 Outline

Most of the thesis is dedicated to dispersive properties of photonic crystal, with particular emphasis on self-collimation effect. In Chapter 2, we briefly explicate the basic concepts and the structure of a completely stable numerical method to solve the time-dependent Maxwell equations numerically.

We first discuss the symmetry properties of the time-dependent Maxwell equations. We discuss numerical approaches , plane-wave method (PWM) , finite-difference time-domain (FDTD) and Finite element method (FE) to analysis the PhC . We also compare the methods with one another.

In Chapter 3 we discussed the beam propagation inside the photonic crystal and how beam can be steered by the dispersion surface of the crystal . We also explain the origin of self-collimation in the photonic crystal.

In Chapter 4, we perform a systematic investigation of self-collimation in square and triangular lattice photonic crystals. We study both square and triangular photonic crystal structures made from isotropic dielectric cylindrical pillars in the background of isotropic materials. We demonstrate the wave vector diagram analysis method that for both photonic crystal structures self-collimation can be observed and are in good agreement from the result of the FDTD simulations.

In chapter 5, we perform a systematic investigation of self-collimation in square lattice photonic crystals with anisotropic constituents. In that chapter we presented

model of 2D square lattice photonic crystal with anisotropic dielectric constants. The specific dielectric parameters used in this study are motivated by recent results on DAST, which is a biaxial anisotropic crystal. We demonstrate the wave vector diagram analysis method that for both photonic crystal structures self-collimation can be observed and are in good agreement from the result of the FDTD simulations.

In chapter 6, In this chapter we introduce the rotation of crystallographic axes relative to the photonic crystal principal axes and investigated how this new degree of freedom affects on the propagation of self-collimated beam.

CHAPTER II

THE STUDY OF PHOTONIC CRYSTALS

2.1 Introduction to the numerical methods

To control the beam in the PhC, we need to select the crystal parameters. And in order to manipulate the crystal parameters, we should have the knowledge about how light would propagate through the particular PhC structure. The propagation characteristics of light in a PhC are completely determined by the band structure. For real dielectric constants a straightforward numerical method has been developed to calculate the dispersion relation for any given periodic dielectric structure. The allowable frequencies (eigenfrequencies) for light propagation in all crystal directions can be determined and the field distributions (eigen vectors, also called Bloch waves) in the crystal for any frequency of light are simply extracted, as well. There are various numerical approaches that analysis the PhC, which provide various degrees of information. Most widely used are the plane wave method (PWM), which is mostly restricted to propagation information about an infinite system, i.e. dispersion relations and polarization mode symmetry of the Bloch waves in the crystal. The transfer matrix method provides quantitative analysis of complex dielectric functions to determine the transmission and reflection characteristics, but with systems that are laterally infinite. The finite-difference time-domain (FDTD)

method has the flexibility to treat finite systems in all directions, as well as complex dielectric functions, but the programs are very intensive to write and they are memory intensive. However, commercial FDTD packages are available on the market. Another method which is less used perhaps because of its complexity is the finite element method (FE), which has many advantages over FDTD and is available as a commercial package. The following section highlights the basic formulations of the PWM, FDTD and FEM.

2.2 Basic Concepts behind the theory of band Structure

In order to study the propagation of light in a photonic crystal, we begin with Maxwell's equations. When the light propagates in the PhC, photons suffer periodic scattering and the Photonic band structure(PBS) appears in the dispersion relations of photons. PBS then represents all possible band states for a given wave vector k . Therefore before a formulation of specific methods, this section introduces the Maxwell's equation in the periodic materials to calculate the eigenmodes and explains some of the frequently used expressions.

2.3 The Reciprocal Lattice and the Brillouin zone

The mode of an electromagnetic wave in a periodic medium is modulated by a periodic function that share the same periodicity as the crystal. In PhC dielectric constant $\epsilon(\mathbf{r})$ is periodic on a lattice that is $\epsilon(\vec{r}) = \epsilon(\vec{r} + \vec{R})$ for all vectors \vec{R} that translates the lattice into itself. The set of vectors \vec{R} is called the lattice vectors. Because of the spatial periodicity we can expand $\epsilon(\vec{r})$ in Fourier series that build the periodic function out of plane waves with various wave vectors. The expansion takes form:

$$\epsilon(\mathbf{r}) = \int d\vec{h} \, g(\vec{h}) e^{i\vec{h} \cdot \vec{r}}. \quad 2.1$$

Here $g(\vec{h})$ is the coefficient on the plane wave with wave vector \vec{h} . But we need only those plane waves with wave vectors \vec{h} such that $\exp(i\vec{h} \cdot \vec{R}) = 1$ for all of the lattice vectors \vec{R} . Now $\exp(i\vec{h} \cdot \vec{R}) = 1$ equivalently, $\vec{h} \cdot \vec{R} = n2\pi$ are called reciprocal lattice vectors and are usually designated by the letter \vec{G} . They form a lattice of their own called the reciprocal lattice. Now we can express the dielectric function, $\epsilon(\vec{r})$ with an appropriate weighted sum over all of the reciprocal lattice vectors, as follows:

$$\epsilon(\vec{r}) = \sum_{\vec{G}} \epsilon_{\vec{G}} e^{i\vec{G} \cdot \vec{r}}. \quad 2.2$$

Every lattice vector \vec{R} can be written in terms of the primitive lattice vectors, which are the smallest set of vectors pointing from one lattice point to another, figure 2.1. For example, on a cubic lattice with spacing a , the vectors \vec{R} would all be of the form $\vec{R} = l\vec{a}_1 + m\vec{a}_2 + n\vec{a}_3$, where (l, m, n) are integers. In general, primitive lattice vectors are defined by \vec{a}_1, \vec{a}_2 and \vec{a}_3 . Now reciprocal lattice vectors \vec{G} can be written as $\vec{G} = l\vec{b}_1 + m\vec{b}_2 + n\vec{b}_3$ since itself creates a lattice. Primitive lattice vectors can be defined by following forms :

$$\vec{b}_1 = 2\pi \frac{\vec{a}_2 \times \vec{a}_3}{\vec{a}_1 \cdot \vec{a}_2 \times \vec{a}_3}, \quad \vec{b}_2 = 2\pi \frac{\vec{a}_3 \times \vec{a}_1}{\vec{a}_1 \cdot \vec{a}_2 \times \vec{a}_3}, \quad \vec{b}_3 = 2\pi \frac{\vec{a}_1 \times \vec{a}_2}{\vec{a}_1 \cdot \vec{a}_2 \times \vec{a}_3}. \quad 2.3$$

The Brillouin zone (BZ) represents the full symmetry of the lattice in reciprocal space. The irreducible Brillouin zone (IBZ) is the smallest region within the BZ for which the

dispersion characteristics of the lattice is not related by symmetry. The behavior of the entire crystal can be obtained by studying the unit lattice in the IBZ due to periodicity.

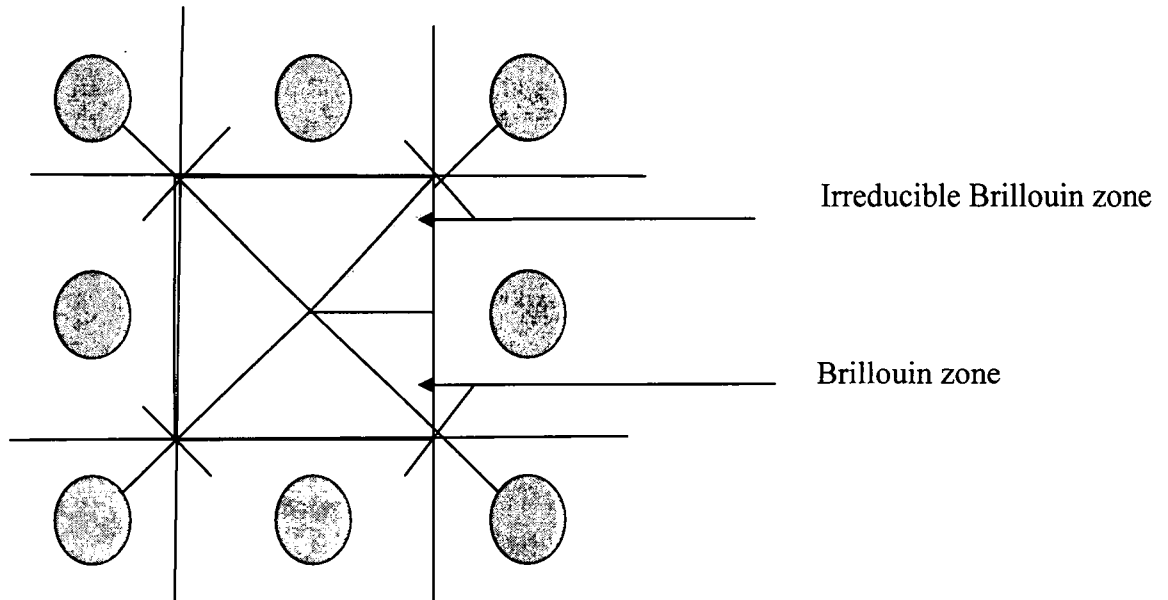


Figure 2.1: First Brillouin zone of the square lattice and the irreducible Brillouin zone for circular rods with isotropic dielectrics.

One does not obtain independent solutions if the analysis is carried out outside the IBZ because of the symmetry connection that is satisfied by reciprocal lattice vector.

2.4 The plane wave expansion method (PWM)

The numerical method, which is based on the Fourier expansion of the electromagnetic field and the dielectric function, is called the plane-wave expansion method. The basic approach for calculating the field distribution and eigenfrequency given a dielectric function and propagation vector is to first expand $\epsilon^{-1}(\mathbf{r})$ or $\epsilon(\mathbf{r})$ and the components of the appropriate electric or magnetic field vector in Fourier series. These series are then

substituted into the decoupled Maxwell's equations and the terms are reorganized into an ordinary eigenvalue problem. When the eigenvalues are calculated employing standard numerical methods (using a finite-sized matrix formed when the Fourier expansions are truncated), it is straightforward to use the eigenvalues to find the allowed propagation frequencies, and the eigenvectors to calculate the field distributions.

To implement this method we begin with Maxwell equation. Maxwell equations in the most general form are give in MKS units as follows.

$$\bar{\nabla} \cdot \bar{E}(\bar{r}, t) = \rho / \epsilon_0 \quad , \quad 2.4$$

$$\bar{\nabla} \cdot \bar{B}(\bar{r}, t) = 0 \quad , \quad 2.5$$

$$\bar{\nabla} \times \bar{E}(\bar{r}, t) = - \frac{\partial}{\partial t} \bar{B}(\bar{r}, t) \quad , \quad 2.6$$

$$\bar{\nabla} \times \bar{B}(\bar{r}, t) = \mu_0 \frac{\partial}{\partial t} \bar{D}(\bar{r}, t) + \mu_0 \bar{J} \quad . \quad 2.7$$

The standard notation for the Electric field, \bar{E} , the magnetic field \bar{H} , the electric displacement, \bar{D} , the magnetic induction, \bar{B} , free charges (ρ), and currents, \bar{J} are used in these equations. Since in our medium we will be concerned with the propagation of light will propagate, we assume that there are no charge or current sources and we can set $\rho=0$ and $\bar{J} = 0$.

In order to solve the Maxwell's equations, we need constitutive equations that relate \bar{D} to \bar{E} and \bar{B} to \bar{H} . Since we are not dealing with the magnetic materials, we can assume that the magnetic permeability of the photonic crystal is equal to that in free space , μ_0 :

$$\vec{B}(\vec{r}, t) = \mu_0 \vec{H}(\vec{r}, t) .$$

We assume the material is isotropic (We later derive the equation for the anisotropic case). Since our main focus on the self-collimating phenomena in PhC and Kosaka *et al.* showed [18] that the collimated light propagation insensitive to the divergence of the incident beam, without applying a nonlinear effect. So we can assume the field strengths are small enough to remain in the linear regime and in this situation the dielectric constant does not depend on the frequency. The electric displacement is thus given by

$$\vec{D}(\vec{r}, t) = \epsilon_0 \epsilon(\vec{r}) \vec{E}(\vec{r}, t) \quad 2.8$$

This is called a local relation connecting $\vec{D}(\vec{r})$ and $\vec{E}(\vec{r})$ of the same position by way of $\epsilon(\vec{r})$ of that point.

The periodicity of $\epsilon(\vec{r})$ implies

$$\epsilon(\vec{r} + \vec{a}_i) = \epsilon(\vec{r}) , \quad (i = 1, 2, 3)$$

where $\{\vec{a}_i\}$ are the elementary lattice vectors of the photonic crystal. With all of these assumptions in place, the Maxwell equations become

$$\vec{\nabla} \cdot \vec{E}(\vec{r}, t) = 0, \quad 2.9$$

$$\vec{\nabla} \cdot \vec{H}(\vec{r}, t) = 0 , \quad 2.10$$

$$\vec{\nabla} \times \vec{E} = -\mu \frac{\partial}{\partial t} \vec{H}(\vec{r}, t), \quad 2.11$$

$$\vec{\nabla} \times \vec{H} = \epsilon_0 \epsilon(\vec{r}) \frac{\partial}{\partial t} \vec{E}(\vec{r}, t). \quad 2.12$$

when $\vec{E}(\vec{r}, t)$ or $\vec{H}(\vec{r}, t)$ are eliminated in last two equations we obtain the following wave equations :

$$\frac{1}{\epsilon(\mathbf{r})} \bar{\nabla} \times \left\{ \bar{\nabla} \times \bar{\mathbf{E}}(\bar{\mathbf{r}}, t) \right\} = -\frac{1}{c^2} \frac{\partial^2}{\partial t^2} \bar{\mathbf{E}}(\bar{\mathbf{r}}, t), \quad 2.13$$

$$\bar{\nabla} \times \left\{ \frac{1}{\epsilon(\mathbf{r})} \bar{\nabla} \times \bar{\mathbf{H}}(\bar{\mathbf{r}}, t) \right\} = -\frac{1}{c^2} \frac{\partial^2}{\partial t^2} \bar{\mathbf{H}}(\bar{\mathbf{r}}, t), \quad 2.14$$

where c stands for the light velocity in free space :

$$c = \frac{1}{\sqrt{\epsilon_0 \mu_0}}.$$

In a stationary state the fields pattern has the following harmonic forms :

$$\bar{\mathbf{E}}(\bar{\mathbf{r}}, t) = \bar{\mathbf{E}}(\bar{\mathbf{r}}) e^{-i\omega t}, \quad 2.15$$

$$\bar{\mathbf{H}}(\bar{\mathbf{r}}, t) = \bar{\mathbf{H}}(\bar{\mathbf{r}}) e^{-i\omega t}, \quad 2.16$$

where ω is the eigen-angular frequency $\bar{\mathbf{E}}(\bar{\mathbf{r}}, t)$ and $\bar{\mathbf{H}}(\bar{\mathbf{r}}, t)$ are the eigenfunctions of the wave equations.

These eigenfunctions should thus satisfy the above two divergence and the two curl equations ;

$$\bar{\nabla} \cdot \bar{\mathbf{E}}(\bar{\mathbf{r}}) = 0, \quad 2.17$$

$$\bar{\nabla} \cdot \bar{\mathbf{H}}(\bar{\mathbf{r}}) = 0, \quad 2.18$$

$$\frac{1}{\epsilon(\bar{\mathbf{r}})} \bar{\nabla} \times \left\{ \bar{\nabla} \times \bar{\mathbf{E}}(\bar{\mathbf{r}}) \right\} = \frac{\omega^2}{c^2} \bar{\mathbf{E}}(\bar{\mathbf{r}}), \quad 2.19$$

$$\bar{\nabla} \times \left\{ \frac{1}{\epsilon(\bar{\mathbf{r}})} \bar{\nabla} \times \bar{\mathbf{H}}(\bar{\mathbf{r}}) \right\} = \frac{\omega^2}{c^2} \bar{\mathbf{H}}(\bar{\mathbf{r}}). \quad 2.20$$

The divergence equations reveal that the fields are constructed from electromagnetic plane waves that are transverse to the associated wave vector. For a given photonic crystal, to find the eigenmodes , we have to solve the the vector wave equations. If we

solve Eq. 2.18, we then find the modes $\vec{E}(\vec{r})$ for a given frequency, subject to the transversality requirements. Then use the Faraday's magnetic induction equation to recover $\vec{H}(\vec{r}) = \frac{i}{\mu_0 \omega} \vec{\nabla} \times \vec{E}(\vec{r})$. However, in this case the differential operator is not Hermitian. The Hermitian operators have real eigenvalues and orthogonal eigenfunctions. Similar derivation can be obtained by eliminating $\vec{E}(\vec{r})$ in favor of $\vec{H}(\vec{r})$ using Eq. 2.20. In this case operator will be Hermitian.

Bloch's theorem can be applied in Eqs. 2.18 and 2.19 as in the case of the electronic wave equation in ordinary crystals with a periodic potential due to the regular array of atoms, because ϵ is a periodic function of the spatial coordinate \vec{r} . To obtain the PBS, let us concentrate on the solution $\vec{H}(\vec{r})$ of Eq. 2.19. We express it as a superposition of plane waves. Expanding $\vec{H}(\vec{r})$ in terms of plane waves by means of Bloch's function :

$$\vec{H}_k(\vec{r}) = \sum_{\vec{G}} \vec{h}_k(\vec{G}) \exp[i(\vec{k} + \vec{G})\vec{r}], \quad 2.21$$

Where $\vec{h}_k(\vec{G})$ is an unknown vector amplitude of the plane wave $(\vec{k} + \vec{G})$, which is to be determined so that $\vec{H}_k(\vec{r})$ is a solution of Maxwell's equation. Bloch theorem should be satisfied by this form

$$\vec{H}_k(\vec{r} + \vec{R}) = e^{i\vec{k} \cdot \vec{R}} \vec{H}_k(\vec{r}), \quad 2.22$$

Substituting Eq. 2.2 and Eq. 2.21 in Eq. 2.20, we obtain the following eigenvalue equations for the expansion coefficients $\vec{h}_k(\vec{G})$:

$$-\sum_{\vec{G}'} \epsilon^{-1}(\vec{G} - \vec{G}') (\vec{k} + \vec{G}) \times \{(\vec{k} + \vec{G}') \times \vec{h}_k(\vec{G}')\} = \frac{\omega^2}{c^2} \vec{h}_k(\vec{G}), \quad 2.23$$

By solving this equation numerically, we can obtain the dispersion relation of the eigenmodes or the photonic band structure [49,50].

PWM is limited to simulating infinitely periodic structures, which is constrained by multiple symmetries and assumed the structure to be lossless. It also assumes the structure to be perfectly periodic, and hence, fabrication tolerances, which highly modulate the spatial and temporal response of a periodic structure, could not be easily simulated in the PWM technique. In addition, it is not capable of calculating the transmission and/or reflection spectra. Nevertheless, PWM remains a useful platform for quickly determining whether a periodic structure does or does not have a bandgap for a specific polarization, and is used for extracting the highly complex dispersive properties of such periodic structures.

2.4.1 Two-Dimensional PWM

For the two-dimensional (2D) crystals, the eigenvalue equations are much simplified if the \vec{k} vector is parallel to the 2D plane. We examine this case here. The structure is assumed to be infinitely long in the z-direction. The electromagnetic waves travel in the x-y plane and are also uniform in the z direction. Hence, $\epsilon(\vec{r})$, $\vec{E}(\vec{r})$, and $\vec{H}(\vec{r})$ are independent of the z coordinate in 2.11 and 2.12. In this case, these vectorial equations are decoupled to two independent sets of equations. The first set is

$$\frac{\partial \bar{E}_z(\bar{r}, t)}{\partial y} = -\mu_0 \frac{\partial}{\partial t} \bar{H}_x(\bar{r}, t),$$

$$\frac{\partial \bar{E}_z(\bar{r}, t)}{\partial x} = \mu_0 \frac{\partial}{\partial t} \bar{H}_y(\bar{r}, t), \quad 2.24$$

$$\frac{\partial}{\partial x} \bar{H}_y(\bar{r}, t) - \frac{\partial}{\partial y} \bar{H}_x(\bar{r}, t) = \epsilon_0 \epsilon(r) \bar{E}_z(\bar{r}, t),$$

and the second is

$$\frac{\partial \bar{H}_z(\bar{r}, t)}{\partial y} = \epsilon_0 \epsilon(\bar{r})_0 \frac{\partial}{\partial t} \bar{E}_x(\bar{r}, t),$$

$$\frac{\partial \bar{H}_z(\bar{r}, t)}{\partial x} = -\epsilon_0 \epsilon(\bar{r}) \frac{\partial}{\partial t} \bar{E}_y(\bar{r}, t), \quad 2.25$$

$$\frac{\partial}{\partial x} \bar{E}_y(\bar{r}, t) - \frac{\partial}{\partial y} \bar{E}_x(\bar{r}, t) = -\mu_0 \frac{\partial}{\partial t} \bar{H}_z(\bar{r}, t).$$

From the first set of these equations, we obtain the following equation by elimination

$\bar{E}_x(\bar{r}, t)$ and $\bar{H}_y(\bar{r}, t)$

$$\frac{1}{\epsilon(\bar{r})} \left\{ \frac{\partial^2}{\partial x^2} + \frac{\partial^2}{\partial y^2} \right\} \bar{E}_z(\bar{r}, t) = \frac{1}{c^2} \frac{\partial^2}{\partial t^2} \bar{E}_z(\bar{r}, t), \quad 2.26$$

From the second set, we obtain the wave equation for $\bar{H}_z(\bar{r}, t)$

$$\left\{ \frac{\partial}{\partial x} \frac{1}{\epsilon(r)} \frac{\partial}{\partial x} + \frac{\partial}{\partial y} \frac{1}{\epsilon(r)} \frac{\partial}{\partial y} \right\} \bar{H}_z(r, t) = \frac{1}{c^2} \frac{\partial^2}{\partial t^2} \bar{H}_z(r, t), \quad 2.27$$

Now the fields pattern has the following harmonic forms :

$$\bar{E}_z(\bar{r}, t) = \bar{E}_z(\bar{r}) e^{-i\omega t}, \quad 2.28$$

$$\bar{H}_z(\bar{r}, t) = \bar{H}_z(\bar{r}) e^{-i\omega t}. \quad 2.29$$

The eigenvalue equations are thus given by

$$\frac{1}{\epsilon(\vec{r})} \left\{ \frac{\partial^2}{\partial x^2} + \frac{\partial^2}{\partial y^2} \right\} \bar{E}_z(\vec{r}) = -\frac{\omega^2}{c^2} \bar{E}_z(\vec{r}), \quad 2.30$$

$$\left\{ \frac{\partial}{\partial x} \frac{1}{\epsilon(\vec{r})} \frac{\partial}{\partial x} + \frac{\partial}{\partial y} \frac{1}{\epsilon(\vec{r})} \frac{\partial}{\partial y} \right\} \bar{H}_z(\vec{r}) = -\frac{\omega^2}{c^2} \bar{H}_z(\vec{r}). \quad 2.31$$

These two kinds of eigenfunctions represent two independent polarizations; one is called the E polarization for which the electric field is parallel to the z-axis, and the other is called the H polarization for which the magnetic field is parallel to the z axis.

When we apply Bloch's theorem as before, we can express $\bar{E}_z(\vec{r})$ and $\bar{H}_z(\vec{r})$ as

$$\bar{E}_z(\vec{r}) = \sum_{\vec{G}} \bar{E}_z(\vec{G}) \exp[i(\vec{k} + \vec{G})\vec{r}], \quad 2.32$$

$$\bar{H}_z(\vec{r}) = \sum_{\vec{G}} \bar{H}_z(\vec{G}) \exp[i(\vec{k} + \vec{G})\vec{r}]. \quad 2.33$$

Substituting Eq.2.32 and Eq.2.33 into Eq.2.30 and Eq.2.31, we obtain the following eigenvalue equations for the expansion coefficients :

$$\sum_{\vec{G}'} \epsilon^{-1}(\vec{G} - \vec{G}') |\vec{k} + \vec{G}|^2 \bar{E}_z(\vec{G}') = \frac{\omega^2}{c^2} \bar{E}_z(\vec{G}), \quad 2.34$$

$$\sum_{\vec{G}'} \epsilon^{-1}(\vec{G} - \vec{G}') (\vec{k} + \vec{G}) \cdot (\vec{k} + \vec{G}') \bar{H}_z(\vec{G}') = \frac{\omega^2}{c^2} \bar{H}_z(\vec{G}) \quad 2.35$$

It should be noted that if the $\epsilon(\vec{r})$ is constant then the equations turn into the usual wave equations commonly employed in electromagnetic. The compact form of the permittivity function in k-space can be written as

$$\epsilon(\vec{G}) = \frac{1}{V} \int_V \epsilon(\vec{r}) e^{-i\vec{G} \cdot \vec{r}} d\vec{r} = \begin{cases} \epsilon_b + f(\epsilon_a - \epsilon_b), & G = 0 \\ (\epsilon_a - \epsilon_b) I(G), & G \neq 0 \end{cases} \quad 2.36$$

where V denotes the 2D volume of the PhC, ϵ_a and ϵ_b represent the dielectric constants of the inner and the background medium respectively, f is the filling fraction and a geometric factor $I(G)$ is defined as

$$I(\vec{G}) = \frac{1}{V} \int_V e^{-i\vec{G} \cdot \vec{r}} d\vec{r},$$

The geometric factor is in the form of $I(\vec{G}) = 2f \frac{J_1(\vec{G}\vec{R})}{\vec{G}\vec{R}}$ for square and triangular lattice

where J_1 is the first-order Bessel function of the first kind.

2.5 Finite Difference Time Domain Method

FDTD method is the formulation of Maxwell's equations in the time domain and this method was introduced by K. Yee in 1966 [51]. Chan *et al.* [52] and Pendry *et al.* [53] developed the finite difference methods to calculate the band structure of the photonic crystals. Initially there was little interest in the FDTD method, probably due to a lack of sufficient computing resources [9]. However, with the advent of low cost, powerful computers and advances to the method itself, the FDTD technique has become a popular method for solving electromagnetic problems.

In the FDTD technique the time dependent Maxwell equations are solved by propagating the electromagnetic fields in the time domain and by modeling the interaction of the electromagnetic fields with the medium. In Maxwell's differential

equations, the change in the E-field in time (the time derivative) is dependent on the change in the H-field across space (the curl). This results in the basic FDTD time-stepping relation that, at any point in space, the updated value of the E-field in time is dependent on the stored value of the E-field and the numerical curl of the local distribution of the H-field in space. The H-field is time-stepped in a similar manner. Iterating the E-field and H-field updates results in a marching-in-time process wherein sampled-data analogs of the continuous electromagnetic waves under consideration propagate in a numerical grid stored in the computer memory. This is the basic concept for 1-D, 2-D, and 3-D FDTD techniques and it has been refined and optimized for specific problems.

In Yee's algorithm the electric and magnetic field components in three-dimensional space are placed so that each E component is surrounded by four circulating H components and every H component is surrounded by four circulating E components

In this way the electromagnetic fields are sampled in a highly efficient manner. The coordinates of the fields are labeled according to $(i, j, k) = (i\Delta x, j\Delta y, k\Delta z)$, where Δx , Δy , and Δz are the mesh sizes for each dimension in this uniform cubic lattice(Figure 2.2). By choosing this specific arrangement, the three-dimensional space lattice is effectively an interlinked array of Faraday's Law and Ampere's Law contours [6] under the central-difference method.

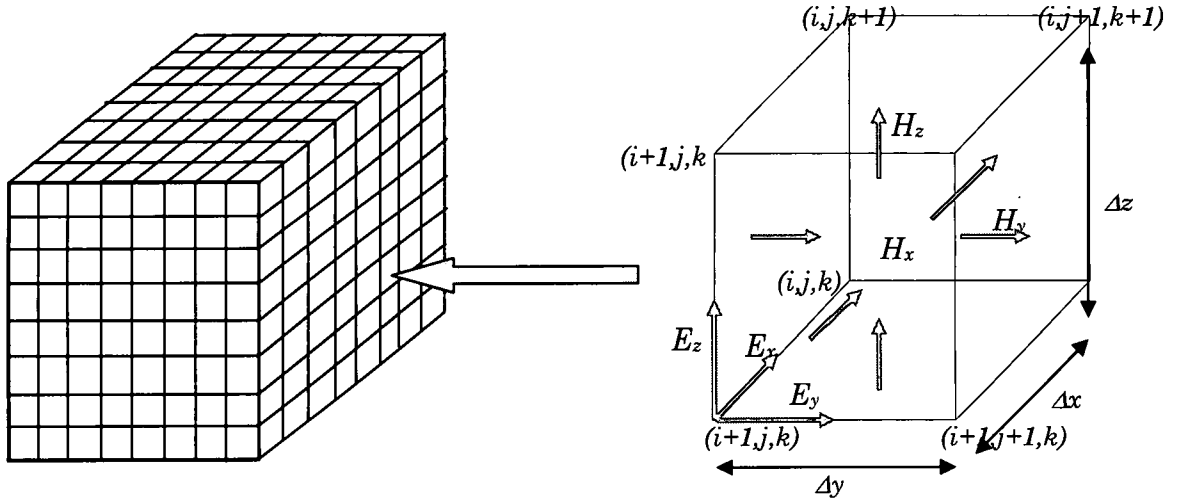


Figure 2.2: Standard Yee lattice used for FDTD and Position of the electric and magnetic field vector components in a Yee cell.

Any function, f of space and time is written as

$$f^n(i, j, k) = f(i\Delta x, j\Delta y, k\Delta z, n\Delta t) ,$$

where Δt is the time increment and n is the time index.

The spatial and temporal derivatives of f are written using central finite difference approximations as

$$\frac{\partial f^n(i, j, k)}{\partial x} = \frac{f^n(i+1/2, j, k) - f^n(i-1/2, j, k)}{\delta}, \quad 2.37$$

$$\frac{\partial f^n(i, j, k)}{\partial t} = \frac{f^{n+1/2}(i, j, k) - f^{n-1/2}(i, j, k)}{\Delta t}, \quad 2.38$$

where $\delta = \Delta x = \Delta y = \Delta z$.

Eq. 2.37 and Eq. 2.38 are applied to the Maxwell's curl equations resulting in explicit finite difference equations and electric and magnetic fields are evaluated at alternate half time steps, such that all field components are calculated in each time step Δt .

To yield accurate results, the grid spacing, δ and the time step, Δt must be choose for reasons of accuracy and stability, respectively. To ensure the accuracy of the computed results, δ must be taken as a small fraction of either the minimum wavelength expected in the model or the minimum scatterering dimension. Thus the field cannot change significantly over one space increment, and the cubic lattice approximation to the smooth scatterering surface cannot be too coarse. To ensure the stability of the time-stepping algorithm ,the stability condition is [56] :

$$v_{\max} \Delta t = \left[\frac{1}{\Delta x^2} + \frac{1}{\Delta y^2} + \frac{1}{\Delta z^2} \right]^{-1/2}, \quad 2.39$$

where v_{\max} is the maximum wave phase velocity expected within the model. A typical finite difference grid contains regions of different dielectric properties representing cell components. By specifying the dielectric properties, $\epsilon(i,j,k)$ and $\sigma(i,j,k)$, of each region, the fields within the enclosed region can be determined.

FDTD provides EM field variations in space with respect to time. The transmission and reflection spectrum of finite structures can be evaluated easily and the wave propagation trough the medium can be observed in time. This method is very powerful and flexible and more favorable to direct comparison with experiments. In addition, frequency dependence and loss can be included in this method. However, band diagram calculations are tedious with the FDTD as the selection of the initial excitation field is

important to excite all possible modes. Similarly, the detection points shouldn't be placed at a high symmetry point. Moreover, if the structure has very sharp edges then uniform meshing may not predict the characteristics well enough. It may be needed to use non-uniform meshing and as a result, the size of the computational domain increases.

2.6 Finite Element Method(FEM)

The basic concepts in the Finite Element Method(FEM) is to find the solution of a complicated problem by replacing it by a simpler one. Since the actual problem is replaced by a simpler one in finding the solution, the final solution is only an approximate solution rather than the exact solution.

Standard FEM process proceeds in three steps in order to solve the Maxwell's wave equations for either the electric or the magnetic field in the frequency domain, Eq. 2.10 or Eq. 2.11 together with appropriate boundary conditions [57]. First, Eq. 2.10 or Eq. 2.11 are identified as solutions of certain variational problems where the boundary conditions at the surface V of the computational domain V have been incorporated as additional terms in the Lagrangian L . For the electric field, the most general variational formulation reads [57]

$$L(E) = \frac{1}{2} \int_V d^3r \left[\frac{1}{\mu} (\vec{\nabla} \times \vec{E}) \cdot (\vec{\nabla} \times \vec{E}) - \frac{\omega^2}{c^2} \epsilon \vec{E} \cdot \vec{E} \right] + \int_{\partial V} dS \left[\frac{\gamma_e}{2} (\hat{n} \times \vec{E}) \cdot (\hat{n} \times \vec{E}) + \vec{E} \cdot \vec{U} \right] + i \frac{\omega}{c_0} \sqrt{\frac{\mu_0}{\epsilon_0}} \int_V d^3r \vec{E} \cdot \vec{j} . \quad 2.40$$

Here, both the magnetic permeability μ and the dielectric function ϵ may vary in space. In addition, \hat{n} denotes the outward normal at the surface ∂V and the electric field

has to satisfy the Dirichlet boundary condition $\hat{n} \times \vec{E} = 0$ on ∂S . γ_e and \vec{U} are known quantities which are used to represent various other types of boundary conditions such as impedance boundary conditions and Sommerfeld radiation conditions [57]. Finally, radiation sources within the computational domain V are described through the spatially varying current density \vec{j} .

The second and most demanding step consists of the discretization of the Lagrangian. To this end, the computational domain V is subdivided into a number of small-volume elements, the so-called finite elements. These finite elements are chosen such that all internal boundaries (surfaces) between materials are approximated by triangular elements. Within each element, the electric field is expanded into a series of certain elementary functions with unknown coefficients. In particular, using the so-called Whitney or vector elements [57], it becomes possible to approximately enforce the divergence conditions of the electric field within a given element as long as the dielectric function does not vary within this element.

In the final step, these expansions facilitate the transformation of the variational equation, Eq. 2.40 into a sparse set of linear equations via the Galerkin method. Here, care has to be taken when assembling the matrices corresponding to the different terms in Eq. 2.40. Local expansions in the individual elements have to be made globally consistent through the boundary conditions between them and an appropriate global numbering that generates well-behaved matrices has to be introduced. This matrix system can subsequently be solved via advanced linear algebra methods, either for obtaining eigenfrequencies and eigenmodes of the system of interest or to determine scattering

cross sections of complex structures as well as transmittance and reflectance through functional elements.

CHAPTER III

LIGHT PROPAGATION IN PHOTONIC CRYSTAL

In my research we studied on the propagating efficiency on self-collimated beam in a two-dimensional PhC. Self-collimation also known as auto-collimation or self-guiding-is a corollary of the anisotropic nature of PhC that confines the group velocities of the propagation modes within the self-collimation band to a small spread of directions, thus reducing diffraction. To enhance and to precisely control the profile of the self-collimated beam, it is necessary to understand the light propagation in the PhC. In conventional geometrical optics, light propagation in dielectric materials is described by the phase refractive index and Snell's law. But in periodic structures, like photonic crystals, the observed refractive effects can be quite complicated and such propagation cannot be understood as simple refraction. Therefore, the direction of the propagation wave cannot be interpreted with the use of a simple Snell's law-like formula.[57-60]. Due to the periodical nature of the structure, the wavevector, k is not conserved although the refraction phenomena relies on the k conservation. The direction of light propagation inside a photonic crystal is determined by its dispersion surfaces, which corresponds to the index ellipsoid in conventional crystalline optics. Notomi [60,61] has theoretically analyzed the light propagation phenomenon in periodic structures and photonic crystals

with the help of the band structure theory and numerical simulations. A more recent detailed systematic study of refraction phenomena occurring in two-dimensional photonic crystals based on the wave vector diagram formalism can be found in [62,63]. In this section we closely follow [60~63] to explain the wave vector diagram analysis.

Light propagation through a PhC structured is governed by its dispersion surfaces, which correspond to the index ellipsoid in conventional crystalline optics. Dispersion surfaces provide a visual representation in k -space of the spatial variation of the spectral properties of a certain band or eigenmode supported by the photonic crystal structure. To quantify the information content within a certain dispersion surface, a section of this surface is taken at a constant frequency. Such a cross section is referred to as an equi-frequency contour (EFC). EFCs provide the necessary information required to predict the response of a photonic crystal structure to a certain incident excitation at a given frequency.

we first consider a very simple example of wave vector diagram analysis shown in Figure 3.1, which graphically describes a light incident problem from air to a dielectric material. The wave vector diagram contains the EFSs that apply for the frequency of operation. For any isotropic homogeneous material, the EFS is a circle and the radius of this circle is

$$k = n\omega / c \quad 3.1$$

k being the wave number, n the refractive index of the medium, ω the working frequency, and c the velocity of light in vacuum. For conventional isotropic homogeneous dielectric materials the phase refractive index is always larger than one. Hence, the circle for the

dielectric material in Figure 3.1 is larger than the one for air which has a refractive index equal to one. The incoming wave vector \vec{k} is drawn on the reciprocal lattice such that it starts at the origin of the reciprocal lattice and points in the direction of the incident wave. The length of \vec{k} is determined by the EFS contour in air.

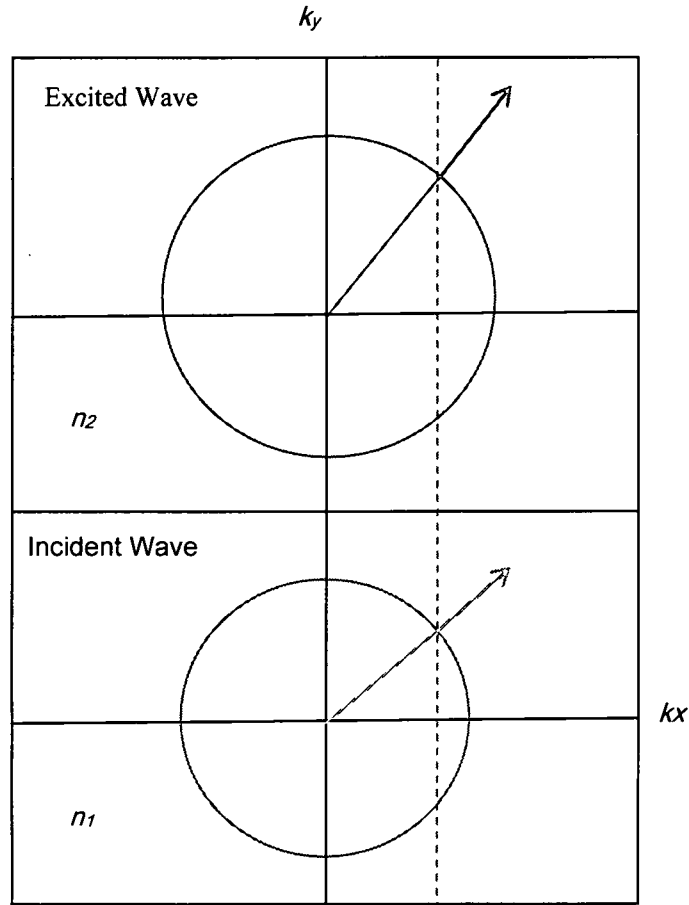


Figure 3.1: Wave vector diagram for a light incident problem from air ($n = 1$) to a homogeneous isotropic dielectric material.

The tangential components of the wave vector \vec{k} are always conserved at the interface. The conservation condition, indicated by the dotted line in Figure 3.1, determines the allowed refracted wave vectors. There are two choices for (to point either towards A or towards B). The propagation direction is determined by the group velocity

$\vec{v}_g = \vec{\nabla}_k \omega$ which is perpendicular to the EFS at the allowed \vec{k} points (point A or B) and which points towards increasing values of frequency. Since for a conventional homogeneous isotropic dielectric medium n is always larger than one, the radii of the EFS increase with increasing frequency. Hence the group velocity always points outwards and $\vec{v}_g \cdot \vec{k} > 0$. Furthermore, the correct choice of \vec{k} is the one that gives a \vec{v}_g that points away from the source. Hence, in this case \vec{k} should point to B. In fact, Figure 3.1 is simply a graphical representation of Snell's law in \vec{k} space [60,61]

$$n_1 \sin \theta_1 = n_2 \sin \theta_2 \quad 3.2$$

where n_1 and n_2 are the phase refractive indices of material 1 and 2, respectively and θ_1 and θ_2 are the angles the propagation directions in material 1 and 2 make with respect to the interface normal.

A similar graphical picture can be made to study light propagation in diffraction gratings and photonic crystals [60,61,64-72]. In figure 3.2 we depict light propagation in a diffraction grating with period of d . In this case, equifrequency circles are repeated along the periodic axis due to the grating's periodicity. And the k -conservation rule has to be generalized to satisfy the periodic boundary condition. As a result of this, applying the k conservation rule, we see that more than one non-identical beams can be excited in a grating. In the figure, wave A (on a circle centered at the origin, red arrow) corresponds to a transmitted wave and wave B (on a circle centered at a reciprocal lattice point, green arrow) is a diffracted wave because of the beam decomposition by a diffraction grating. Light propagation direction is not parallel to the k vector for a diffracted beam but it is oriented normal to the diffracted wave circle. This is a graphical representation of the formula for a diffraction grating

$$m\lambda = d(\sin \theta_1 + \sin \theta_2)$$

3.3

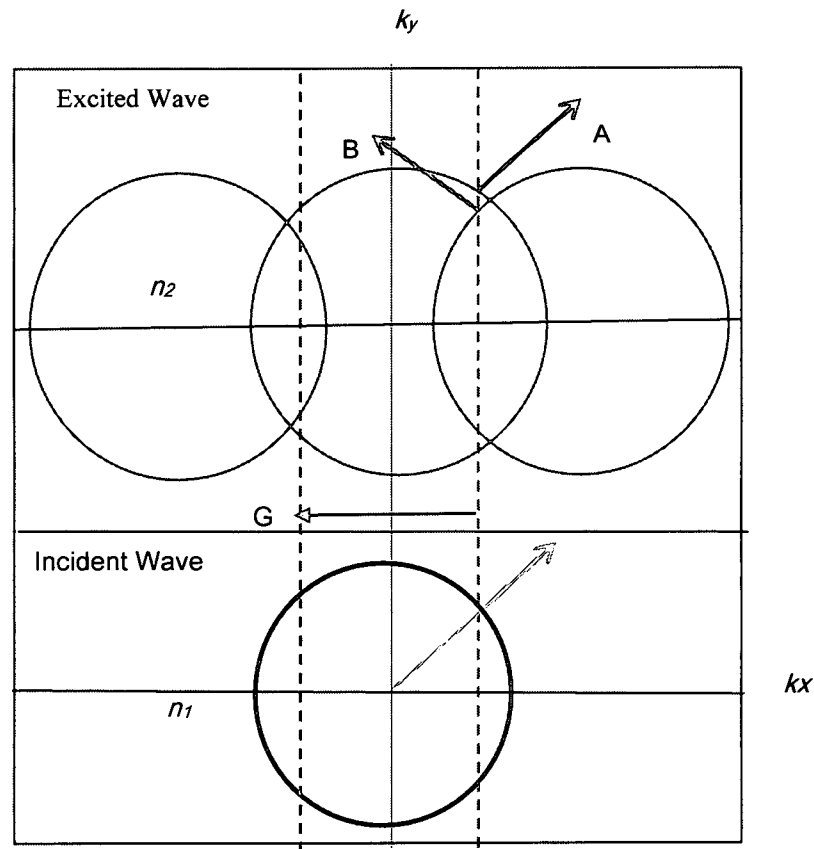


Figure 3.2: Wave vector diagram for a light incident problem from air ($n = 1$) to diffraction grating .

We now move to the case for photonic crystals. Using the vector diagram analysis, Notomi has shown that the propagation characteristics of diffraction gratings and weakly modulated photonic crystals, that is photonic crystals built from constituents with a small difference in dielectric constant ($\mu = 1$), are very similar [61,63]. For such periodic structures a phase index in terms of Snell's law cannot be defined [4,5]. If one would define a phase index, the index would strongly depend on the incident angle and therefore Snell's law loses its meaning. However, above wave vector diagram analysis for the diffraction grating can be used to explain typical features of photonic crystal [4, 5]. Also

the anomalous light propagation reported for photonic crystals such as for example the superprism effect and the ultrarefractive properties can be understood within this picture [60,61]. Thus these phenomena cannot be understood within a refraction picture and must be understood as diffraction. Note that for a complete understanding of light propagation in diffraction gratings and photonic crystals it is not sufficient to study propagation modes in the first Brillouin zone [61,63] All allowed propagation modes in the repeated zone scheme should be investigated [61,63].

However for strongly modulated photonic crystals near the photonic band gap an effective phase refractive index can be defined to explain the light propagation inside the photonic crystal using Snell's law and this in spite of the presence of strong multiple diffraction [61,63]. For simplicity of notation, we also denote this effective refractive index by n . In strongly modulated photonic crystals, the phase refractive index can be smaller than one and can also be negative. This can lead to unusual refraction phenomena such as ultra-refractivity and negative refraction .

To explain this we consider a two-dimensional photonic crystal slab made from dielectric pillars with radius $r = 0.35a$ and $n = 3.6$ arranged in a square lattice with lattice constant a [61,63]. The photonic band structure diagram for the TM-mode is depicted in figure 3.3.

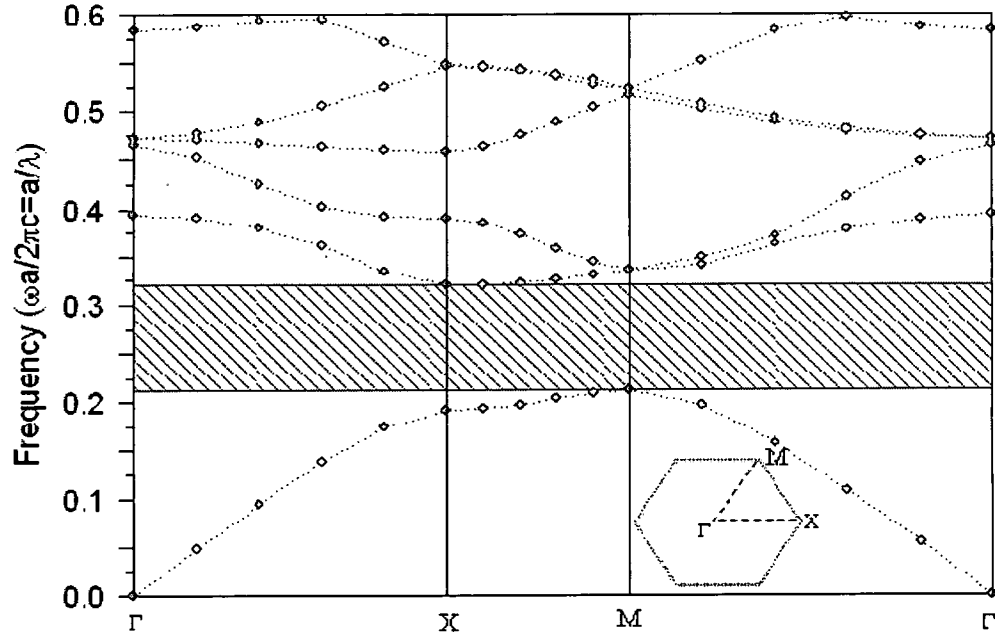


Figure 3.3: Photonic band structure diagram of TM modes for a two-dimensional photonic crystal made from dielectric holes in air with radius $r = 0.35a$ and refractive index 3.6 arranged in a triangular lattice with a lattice constant a . The first Brillouin zone of a triangular lattice and the symmetry points are shown in the inset .

For the dimensionless frequency range $f = \omega a / 2\pi c \in [.34 .46]$, we obtain the EFS depicted in Figure 3.4. From Figure 3.4 it can be seen that the shape of the EFS change from the star shape to round as the frequency increased and finally becomes circular. In the latter case, the EFS plot looks similar to that of a conventional dielectric material as shown in Figure 3.3.

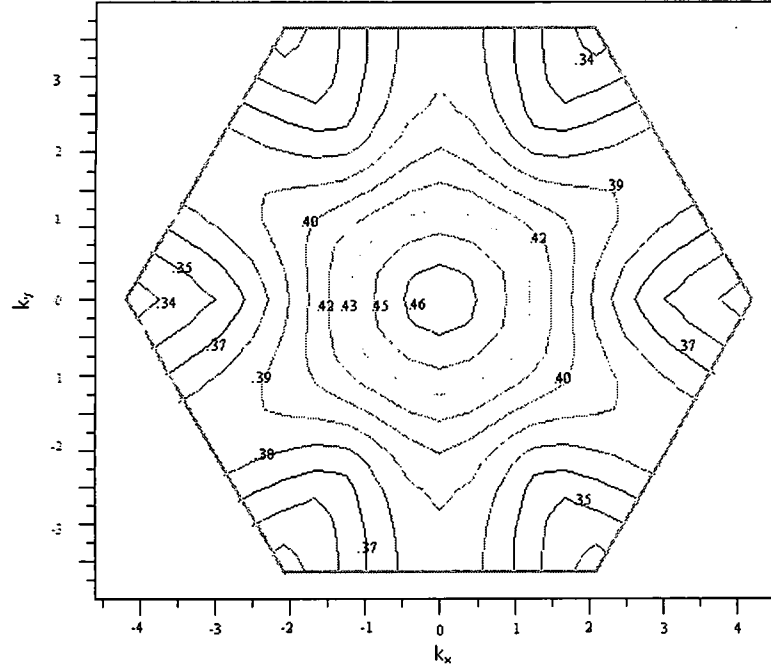


Figure 3.4: EFS plot of TE modes for a two-dimensional photonic crystal made from dielectric holes in air with radius $r = 0.35a$ and refractive index 3.6 arranged in a triangular lattice with a lattice constant a . The first Brillouin zone of a triangular lattice and the symmetry points are shown in the inset.

This means that we can define an effective refractive index n from the radius of the EFS using Snell's law, suggesting that for these frequencies the beam propagation is refraction like. However, for these frequencies there is a striking difference from conventional refraction. But in this case, the circle (equifrequency contour) for air is larger than the one for the photonic crystal (see Figure 3.2). As a consequence, for certain angles of incidence no light beam propagates in the photonic crystal since the light is totally reflected off the interface. This corresponds to total internal reflection, a phenomenon which does not occur when a light beam is incident from air to a conventional material.

The sign of n is determined from the behavior of the EFSs. In this case the EFSs move inwards with increasing frequency, as can be seen from Figure 3.4. Hence $\bar{v}_g \cdot \bar{k} < 0$. It can be proven analytically that for the infinite photonic crystal system, the direction of the group velocity coincides with the direction of the energy velocity [73]. Therefore, the group velocity vector represents the direction of propagation for the electromagnetic wave in the photonic crystal. The sign of n is given by the sign of $\bar{v}_g \cdot \bar{k}$. Thus in this case we have negative index. The propagation direction of the electromagnetic wave is inward. This results in a negative propagation angle for all incident angles. Schematically, this can be seen from figure 3.11b. Since the direction of propagation is determined by the group velocity and points away from the source, \bar{k} should point to A. The group velocity is perpendicular to the EFS at point A. Note that for this particular example, it is sufficient to study the propagation modes in the first Brillouin zone only. Therefore it is sufficient to display the EFSs in the reduced zone scheme. In what follows, we will only use the extended or repeated zone scheme if it is necessary to explain the wave propagation. The wave vector diagram analysis method is an adequate method to determine the propagation angles.

3.1 Origin of self-collimation

Curvature of the dispersion surface can indicate beam divergence or convergence, whereas the lack of curvature, or straight EFS contour lines, leads to the so-called self-collimation phenomenon. To explain this, a typical branch of a dispersion surface in reciprocal space for a PhC is schematically shown as a thick curve in figure 3.5[62]. The curvature of the dispersion surface turns from downward to upward and incident light

comes from the top of the figure. The direction of propagation light in the PhC is normal to the dispersion surface at the tie points (A, B and C). The direction in reciprocal space exactly corresponds to that in real space because of the symmetry.

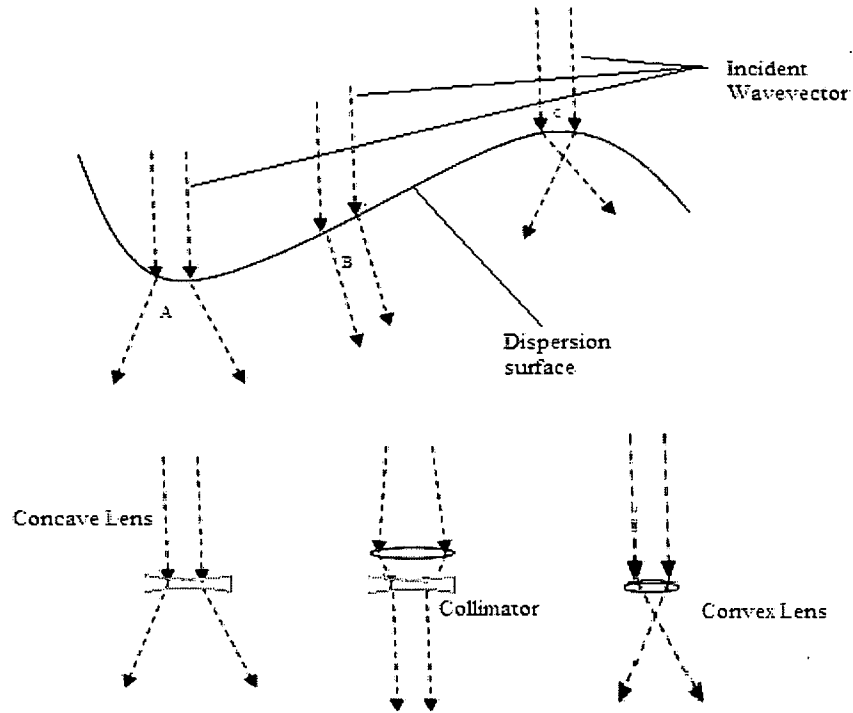


Figure 3.5 : A schematic illustration of the self-collimating phenomena(B) together with the divergence (A) and convergence case (C). Each case corresponds to respectively, the collimator(B), concave lens(A) and convex lens(C) in conventional optics.

Thus we can categorize the light propagation in a PhC into the following three cases:

- (1) at the tie point of downward curvature (point A), the light in the PhC shows divergent propagation as in a concave lens.
- (2) At the tie point of upward curvature (point C), the light shows divergent propagation after convergence as in a concave lens
- (3) At the approximately linear area around the inflection point from downward to upward

curvature (point B), the light shows almost collimated propagation. This phenomenon is analogous to a collimator, which is made with a combination of concave and convex lenses as shown in the figure 3.5[62].

In my research my main focus is at the point B where the EFS is flat. The EFS dispersion surface is affected by lattice symmetry, material parameters and the geometric shape of the constituents[74]. The dispersion surfaces of photonic crystals made with anisotropic constituent materials provide another degree of freedom for improving the performance. we changed all these parameters to enhance the self-collimated beam inside the PhC.

CHAPTER IV

SELF COLLIMATED BEAM IN SQUARE AND TRIANGULAR ISOTROPIC PHOTONIC CRYSTAL

In the previous chapter, we discussed the light propagation in photonic crystal and the possibility of observing a self –collimated beam. In this chapter, we study this phenomena in great detail for square and triangular lattice photonic crystals. We present finite-difference time domain (FDTD) simulation results for the propagation of light in isotropic photonic crystals with square and triangular lattice symmetry and use the FDTD technique described in Chapter 2 to investigate the space and time evolution of the electromagnetic waves. Photonic band structure diagrams and equifrequency surface (EFS) plots are obtained by using the Plane wave expansion method (PWM) written in MatLab .

4.1 Dielectric circular rods in isotropic medium

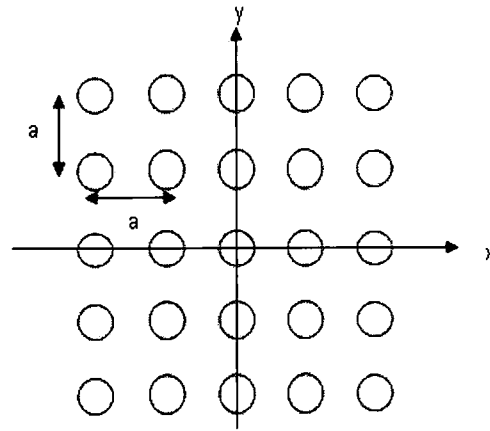
In this section, we study photonic crystal structures made from dielectric cylindrical pillars organized in square and triangular lattices. We used the background index 2.55 and pillar index 1.64 and $\mu = 1$ for the magnetic permeability and radii varied from $r = 0.1a$ μm to $0.5a$ μm , where a is the period of the lattice. This choice of material

parameters is taken from the crystalline and photobleached refractive indices of DAST, which will be discussed about selecting this material in next chapter

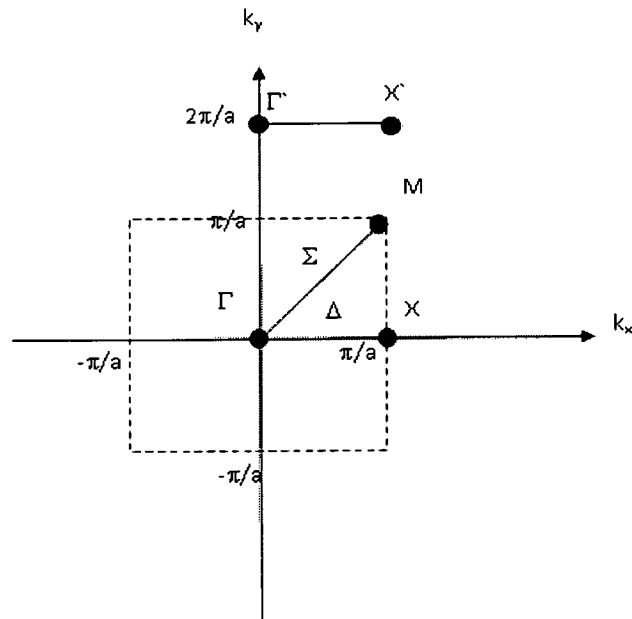
4.2 .1 Photonic band structure diagram and EFS plots for 2D square lattice

We first examine the band structure of the square lattice. It assumed that one dielectric cylinder is located at each lattice point. The following values were used for the numerical calculation: The dielectric constant of the cylinder and the background are 2.6896 and 6.5025. Fig 4.1. The first BZ corresponding to this structure is also a square lattice and belongs three high symmetry points, Γ (0,0) , X (π/a ,0) and M point (π/a , π/a).

The photonic band structure can be specified by the polarization. If the E-field parallel to the dielectric cylinders then the modes are classified as E-polarized modes or TE modes. Similarly when the H-field is parallel to the dielectric cylinders then the modes are classified as H-polarized modes or TM modes. Figure 4.1 shows the lattice structure of the photonic crystal composed of a regular square array of circular dielectric cylinders and the 2D first Brillouin zone of the square lattice.



(a)



(b)

Figure 4.1(a) Cross-section of the 2D square lattice composed of circular cylinders (b) First Brillouin zone of the square lattice

An Equi-frequency surface(EFS) of frequency ω is obtained by sweeping the wave vector in the entire BZ to look for the band states of ω . There are, in general, several

bands that can overlap in frequency space and they will simultaneously appear in constructing an EFS. In figure 4.2 we present the Equi-frequency surfaces for the first and second band of the square lattice with cylinder radius $0.1a$. The wave vector is scaled so that the first Brillouin zone lies in the range $(-\pi, \pi)$ for each component.

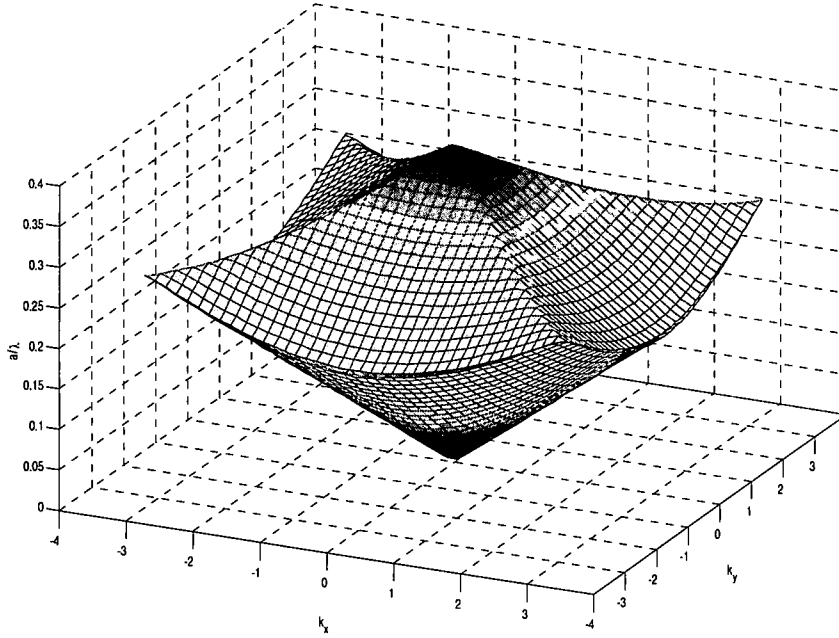
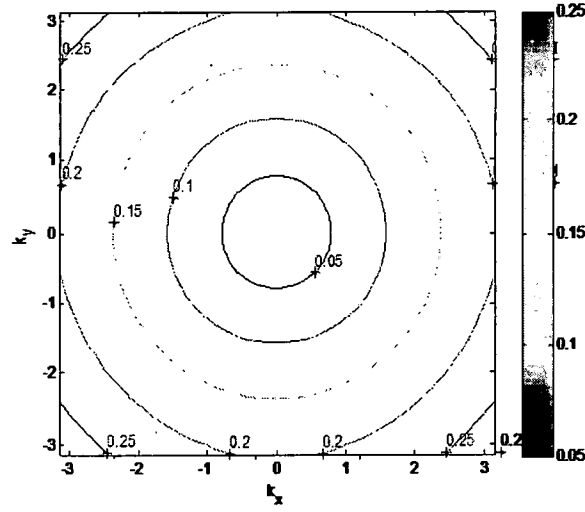


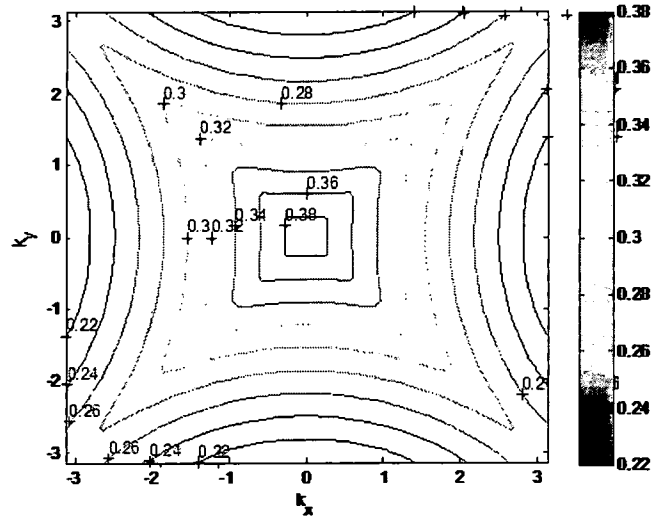
Figure 4.2 3D view of the equi-frequency surface for the 1st and 2nd band of the square lattice with isotropic materials. The refractive indices are $n_{\text{rod}} = 1.64$ and $n_{\text{host}} = 2.55$ and the radius of the rods $r = 0.1a$.

By comparison the same dispersion surfaces in figure 4.2 are shown as contours in figure 4.3(a-b). The first band has an isotropic isofrequency curve features near the center of the Brillouin zone; while the second band has a square, pyramidal shape with slight curvature and rounded edges. The frequencies of the two bands overlap in angular frequency range from $(0.22, 0.25)$. For the second band there is a frequency where the curvature is minimized over a wide range of input angles and this constitutes the optimal isofrequency value for self-collimation in the photonic crystal. As we mention previously

in Chapter 3 the extent of self-collimation is quantified by examining the group velocity, which is determined by the gradient of the frequency in the k space.



(a)



(b)

Figure 4.3 Contour representation of the equi-frequency surface for the (a) 1st and (b) 2nd band of the square lattice with isotropic materials. The refractive indices are $n_{\text{rod}} = 1.64$ and $n_{\text{host}} = 2.55$ and the radius of the rods $r = 0.1a$

The magnitude of the group velocity index near the band center for the first band is 2.0 over most of the Brillouin zone, except near the band edges, and the group velocity magnitude for the second band is also 2.0 over most of the Brillouin zone region. By inspecting the EFS, the pyramidal-shaped second band has a region where the crystal self-collimates an incident beam over a range of angles.

When such a PhC is illuminated within a low frequency range of first band, the isofrequency contours are circularly shaped and incident light on the PhC undergoes usual refraction when the wave vector is sufficiently far from the Brillouin zone boundary. However, the second band EFS have a flattened, squarer shape for a range of frequencies. For an incident beam propagating close to the y -axis, a range of transverse wave vectors, k_x , is used to determine the degree of self-collimation. For the isofrequency contour $a/\lambda = 0.34$, the beam is collimated for the range of scaled transverse wave vectors, k_x , lying between about -0.6 and $+0.6$. Since the surface is not perfectly flat then there is some deviation in the collimated beam. The divergence angle calculated by the deviation of the group velocity from vertical. The group velocity varies from vertical by about $\theta_g < 2^\circ$ (i.e., $\sin \theta_g = v_{gx}/|v_g|$). The range of the scaled transverse wave vector k_y lies between about -0.6 and $+0.6$, for light in the PhC propagating within an angle of 2° of the x -axis. The incident angle is determined by using Snell's law in the form $a/\lambda \sin(\theta_{in}) = k_x/2\pi$, the calculated maximum input angle for $a/\lambda = 0.34$ and $k_y = 0.6$ is about 6.5° . In other words, an incident light beam with a divergence up to 6.5° can be self-collimated in the PhC to within 2° . It is desirable to have a larger flatter surface so the acceptable incident angle will be larger and therefore incident light with a higher divergence can be collimated in the PhC.

The cylinder radius is one of the strong parameter affecting the dispersion surfaces. We changed the radii from r/a 0.1 to 0.5. In figure x we summarize the effect of the cylinder radii by plotting the angular deviation of the group velocity from the surface normal.

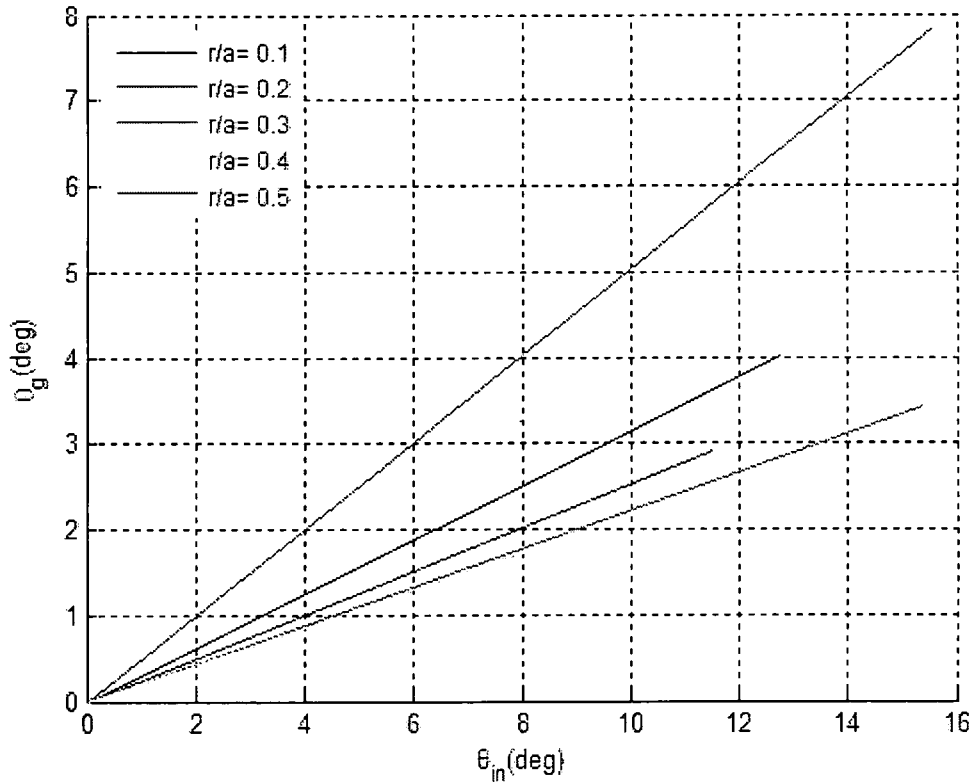


Figure 4.4 : Deviation of the group velocity from normal for the scaled cylinder radius versus input angles of those where the deviation from Snell's law will be minimal.

As seen in figure 4.4 , increasing the radii does not provide wide range of input angles but it lowers the deviation angle in other word we have more flat dispersion surface. But the turning point is $r/a= 0.5$ where the cylinders touch each other and beam is diffracted in this case. By analysis of figure 4.4, to keep the minimum deviation within

3° , we found the maximum input angle 14° for the case of $r/a = 0.4$ and for the normalized frequency of $a/\lambda = 0.4$. Figure shows the second band contour of $r/a = 0.4$.

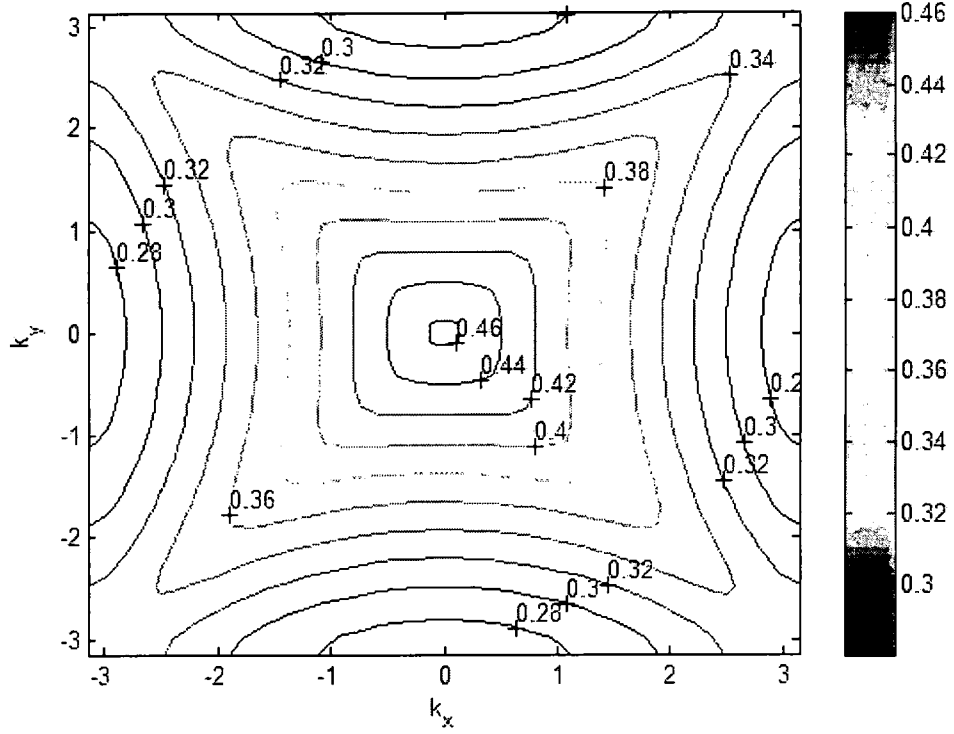
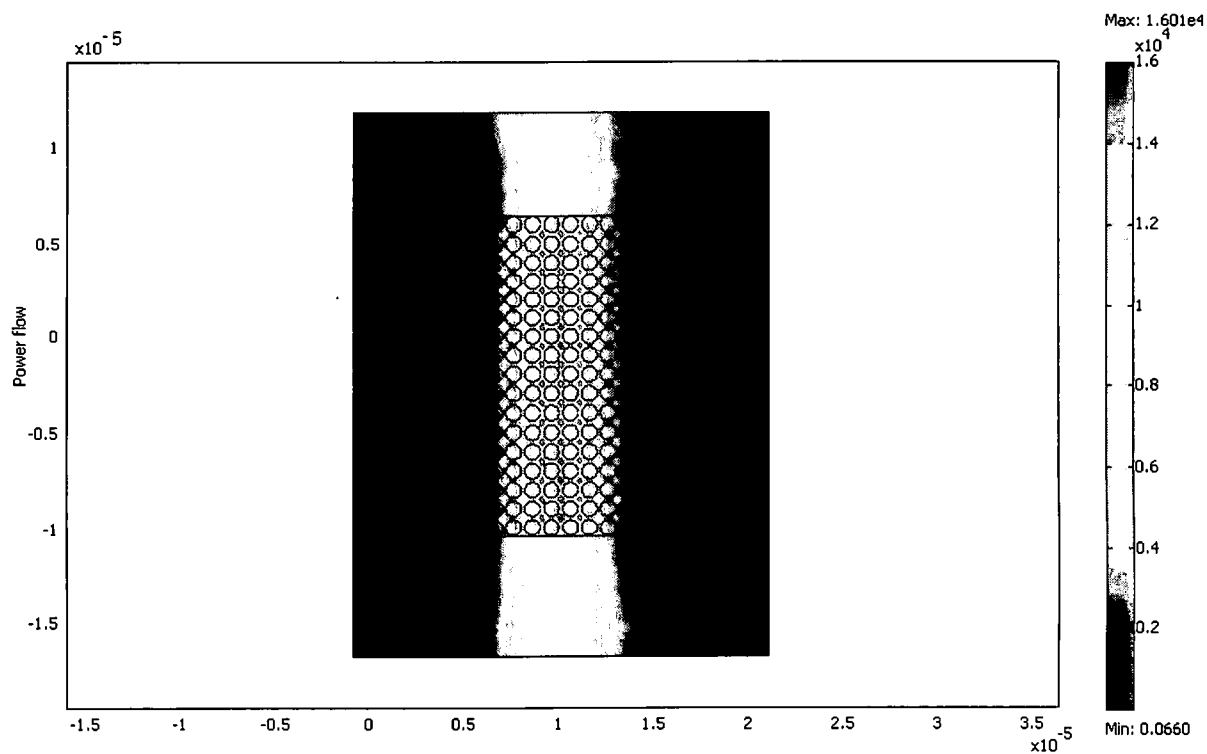


Figure 4.5 Contour representation of the equi-frequency surface for the (a) 1st and (b) 2nd band of the square lattice with isotropic materials. The refractive indices are $n_{\text{rod}} = 1.64$ and $n_{\text{host}} = 2.55$ and the radius of the rods $r = 0.4a$

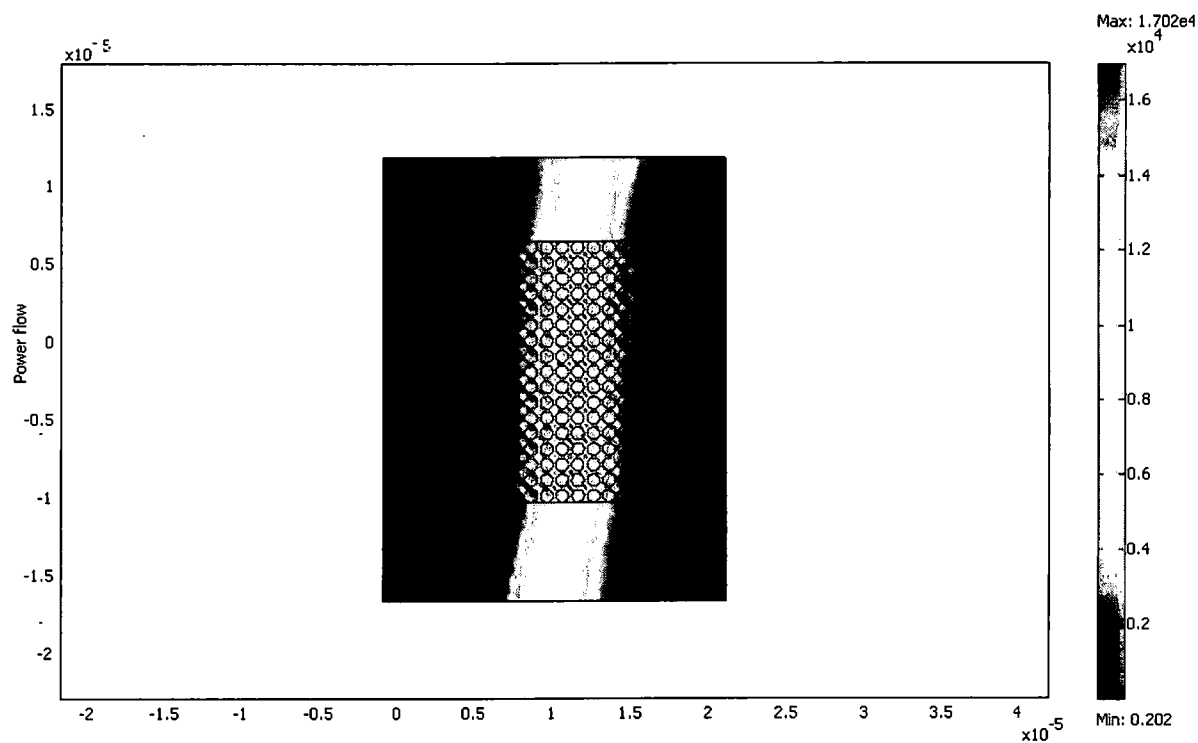
If an incident light beam propagation close to y-axis with normalized frequency of 0.4 then maximum input angle would be 14° that will be self-collimated inside PhC within 3° deviation. Now we compare our theoretical results with the simulations results by using FDTD and FE.

4.2.2 FEM Modeling Results

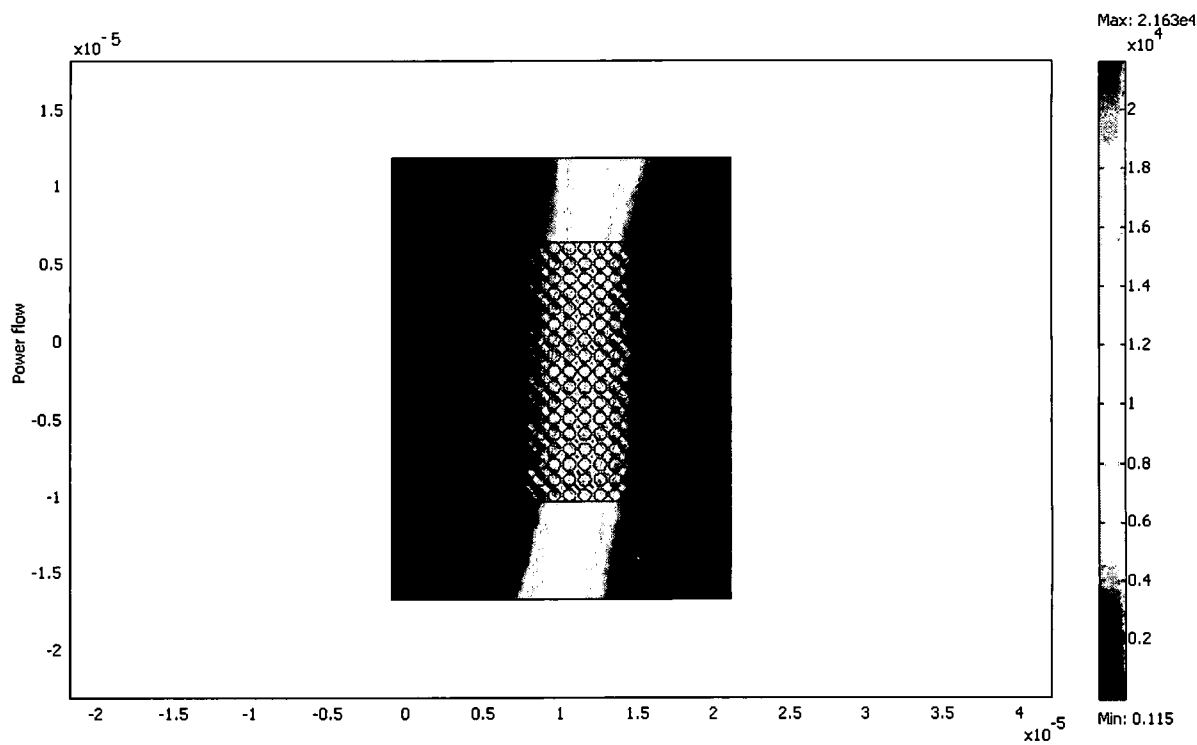
To model the beam propagation through our lattice, we simulated a $3\mu\text{m}$ wide Gaussian beam and launch it $6.375\mu\text{m}$ away from the input interface. Figure 4.5 shows the outline of the PhC used in the simulations. The width and the length of the structure is $22a$ and $17a$ respectively. The refractive index of the background host and the cylinder rod are set to the same values as in the previous calculation, i.e., 2.55 and 1.64 . The power flow through the crystal from the air for the TM mode at different angles are shown in figure 4.6.(a-e). Since the energy velocity is coincide with the group velocity, the energy velocity vector in these figures represent the direction of propagation of the electromagnetic wave in the photonic crystal. Figure 4.6 (a) is the power flow through the crystal from air with the incident angle of 0° . As it is expected no divergence of the incident beam . Now if we increase the incident angle, we find a good collimated beam till 12° the deviation of 3° . The theoretically predicted value of the self-collimation beam is 14° within this deviation range is 3° . Actually collimated beam is observed even 15° but the power is decreased almost 60% and the quality of the beam is degraded. Hence both our simulations and theoretical result agree .



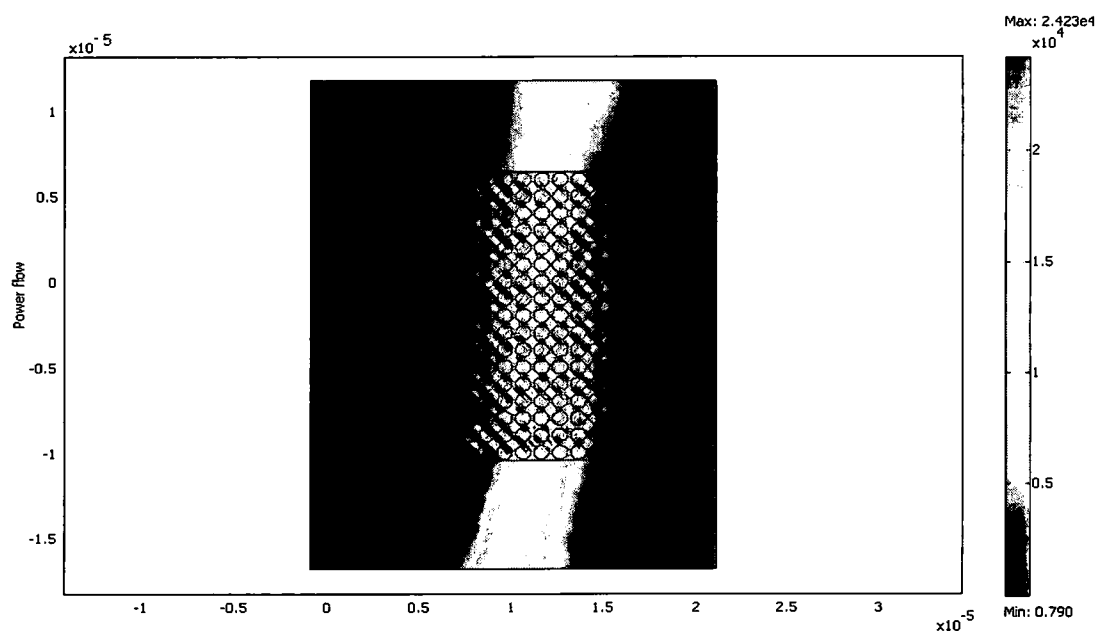
(a) Incident angle 0



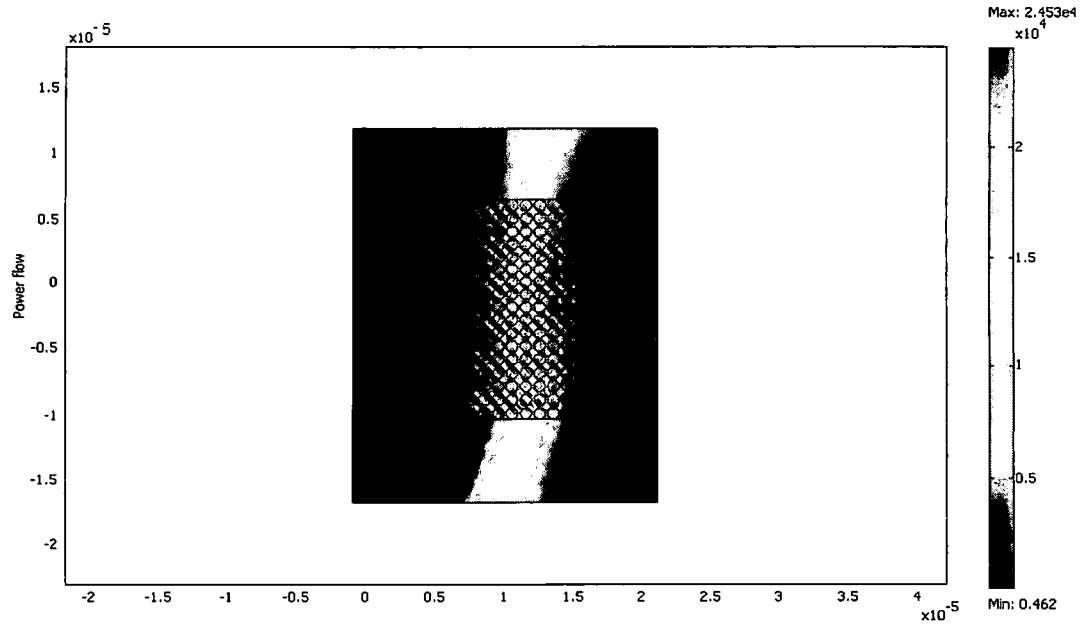
(b) Incident angle 10



(c) Incident angle 12



(d) Incident angle 14⁰



(e) Incident angle 15

Figure 4.6 : Power flow through the PhC from air with the incident angle of a) 0° , b) 10° , c) 12° , d) 14° , and e) 15° respectively.

4.3.1 Photonic band structure diagram and EFS plots for 2D Trinagular lattice

Now we examine the band structure of the isotropic triangular lattice. The following values were used for the numerical calculation: The dielectric constant of the cylinder and the background are 2.6896 and 6.5025. It assumed that one dielectric cylinder is located at each lattice point. Figure 4.1 shows the triangular lattice structure of the photonic crystal composed of circular dielectric cylinders and the 2D first Brillouin zone of the lattice. First Brillouin zone corresponding to this structure is a hexagonal lattice. The elementary lattice vectors (a_1 , a_2) are

$$a_1 = \begin{pmatrix} a \\ 0 \end{pmatrix}, \quad a_2 = \begin{pmatrix} a/2 \\ \sqrt{3}a/2 \end{pmatrix}$$

and the elementary reciprocal lattice vectors (b_1, b_2) are

$$b_1 = \begin{pmatrix} 2\pi/a \\ -2\pi/\sqrt{3}a \end{pmatrix}, \quad b_2 = \begin{pmatrix} 0 \\ 4\pi/\sqrt{3}a \end{pmatrix}.$$

In the reciprocal lattice zone, there are three highly symmetric points : the Γ point $(0,0)$, K point $(4\pi/3a, 0)$ and M point $(\pi/a, -\pi/a)$. The triangle, Γ KM created by these symmetric points is the irreducible Brillouin zone of this structure.

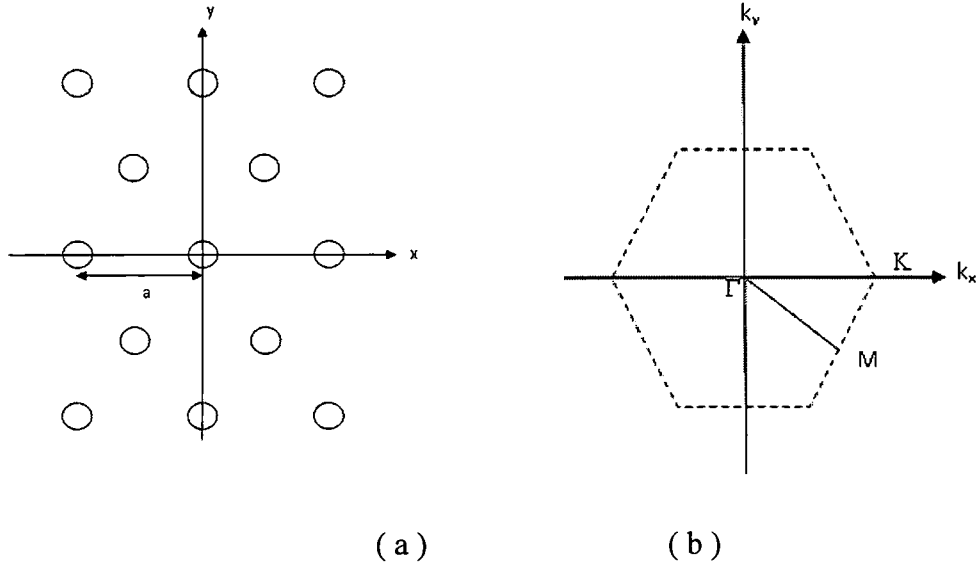


Figure 4.7(a) Cross-section of the 2D triangular lattice composed of circular cylinders (b) corresponding First Brillouin zone

In figure 4.8 we present the Equi-frequency surfaces for the first and second band of the square lattice with cylinder radius $0.1a$. The wave vector is scaled so that the first Brillouin zone lies in the range $(-\pi, \pi)$ with a cylinder radius $0.1a$.

In figure 4.9 we present the EFS for the first and second band of the square lattice with cylinder radius $0.1a$. The wave vector is scaled so that the first Brillouin zone lies in

the range $(-\pi, \pi)$ for each component. We observe here that the surface consists of several sheets and they are not at all spherical in shape and some portion of the sheet is very flat. This is the region we are mainly interesting for the self-collimation beam as we mention earlier as the direction of the group velocity is normal to the EFS..

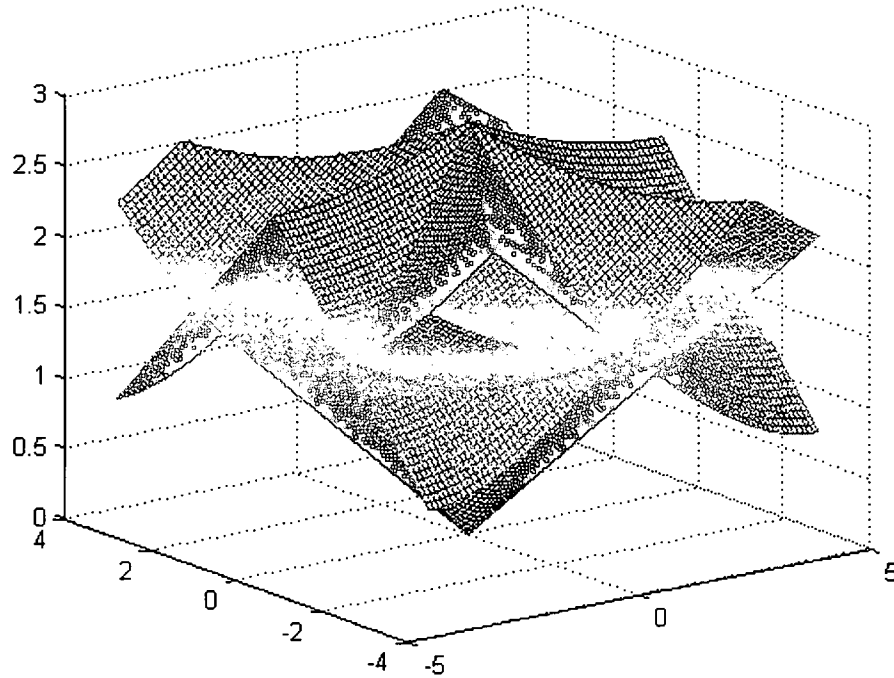
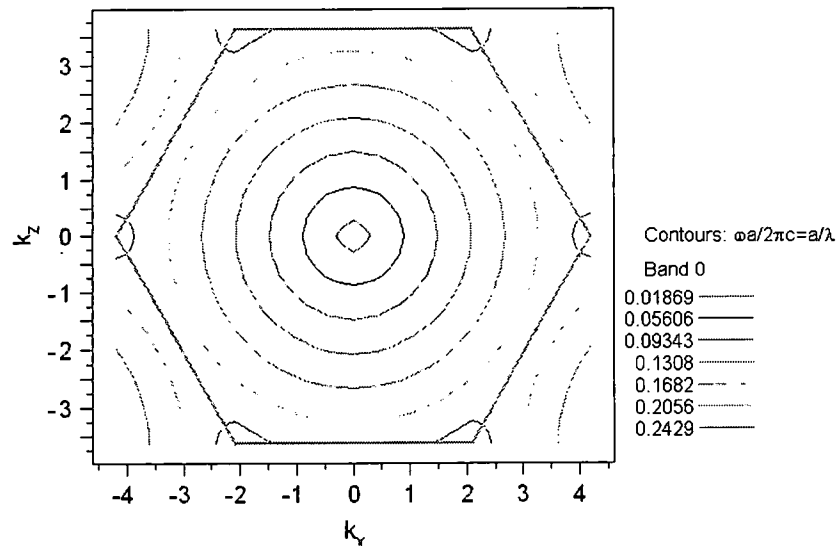
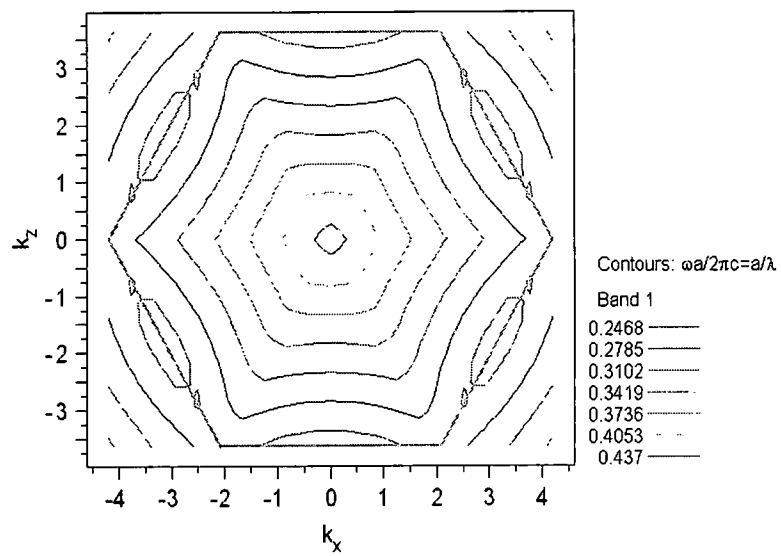


Figure 4.8: 3D view of the equi-frequency surface for the 1st, 2nd and 3rd band of the triangular lattice with isotropic materials. The refractive indices are $n_{\text{rod}} = 1.64$ and $n_{\text{host}} = 2.55$ and the radius of the rods are $r = 0.1a$.

By comparison the same dispersion surfaces in figure 4.3(a-b) are shown as contours. The first band has an isotropic isofrequency curve features; while the second band has a hexagonal shape with slight curvature and rounded edges and the 3rd band has star shape in upper frequency and pyramid shape in the lower frequency zone.



(a)



(b)

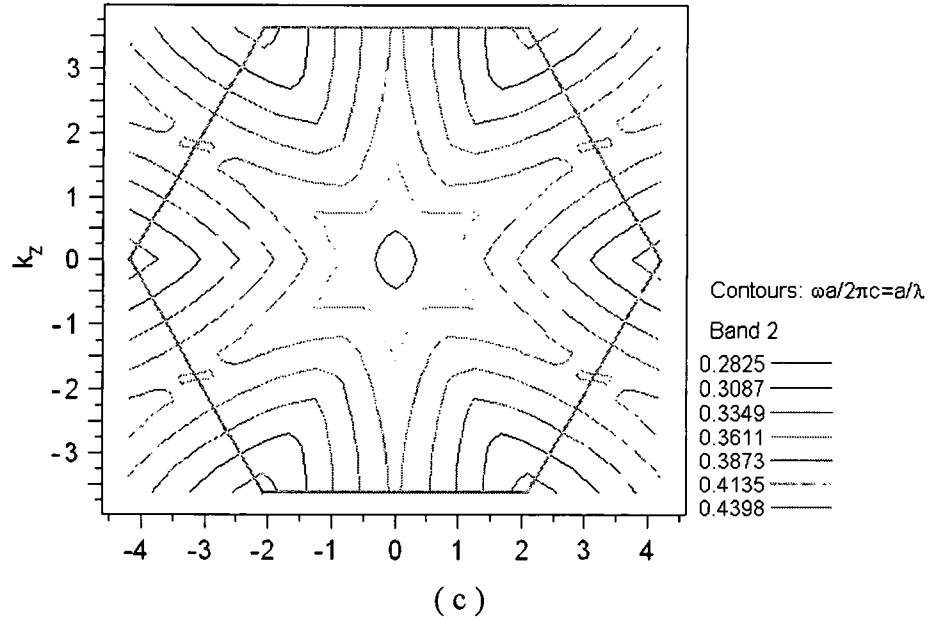
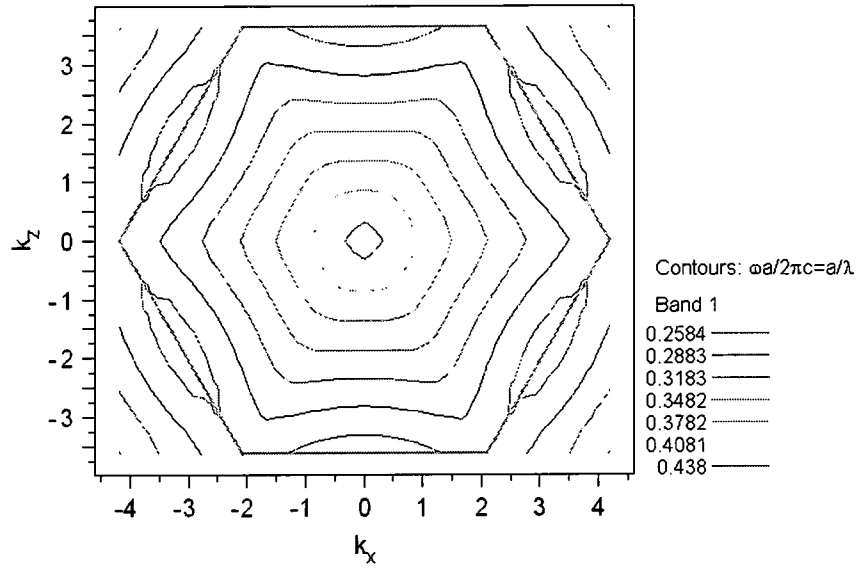


Figure 4.9: Contour representation of the EFS surface for the (a) 1st, (b) 2nd and (c) 3rd band of the triangular lattice with isotropic materials. The refractive indices are $n_{\text{rod}} = 1.64$ and $n_{\text{host}} = 2.55$ and the radius of the rods $r = 0.1a$

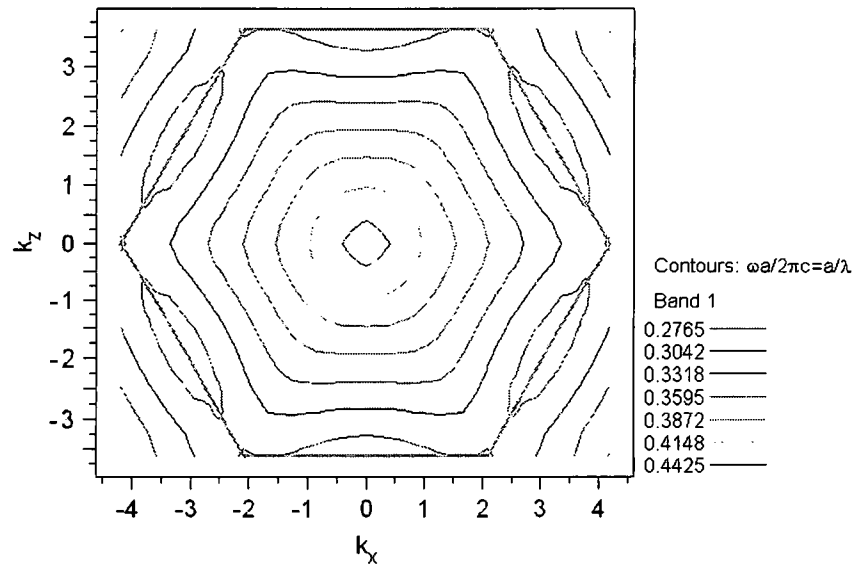
By inspecting the EFS, the hexagonal-shaped second band has a region where the crystal self-collimates an incident beam over a range of angles. When such a PhC is illuminated within frequency range of second band, the incident light on the PhC will be collimated and the quality of the collimated beam depends on the flatness of the contour. Now we want more working space that means a wider surface so wide range of incident angle will be in the range of self-collimation. However wider surface is not perfectly flat. But if the collimated beam is within the accepted range of deviation than we can consider that region of the contour. For an incident beam propagating close to the y -axis, a range of transverse wave vectors, k_x , is used to determine the degree of self-collimation. For the EFS contour of $a/\lambda = 0.37$, the beam is collimated for the range of scaled

transverse wave vectors, k_x , lying between about -0.7 and $+0.7$. The incident angle that will be collimated inside the PhC is determined by using Snell's law in the form $a/\lambda \sin(\theta_{in}) = k_x/2\pi$, the calculated maximum input angle for $a/\lambda = 0.37$ and $k_y = 0.6$ is about 6.5° . In other words, an incident light beam which is hit the surface of the PhC with 6.5° will be self-collimated inside PhC where deviation from normal is within 2° . Now in the next step we changed the cylinder radii in such of flattened wide contour of the 2nd band.

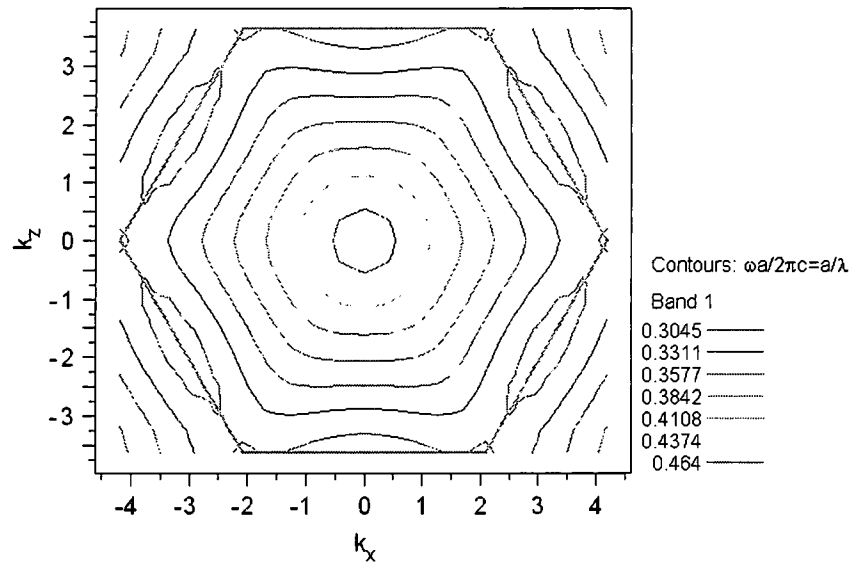
The cylinder radius is one of the strong parameter affecting the dispersion surfaces. We changed the radii from r/a 0.1 to 0.5. In Fig 4.10 represent the 2nd band of the triangular lattice for radii of 0.2 to 0.5.



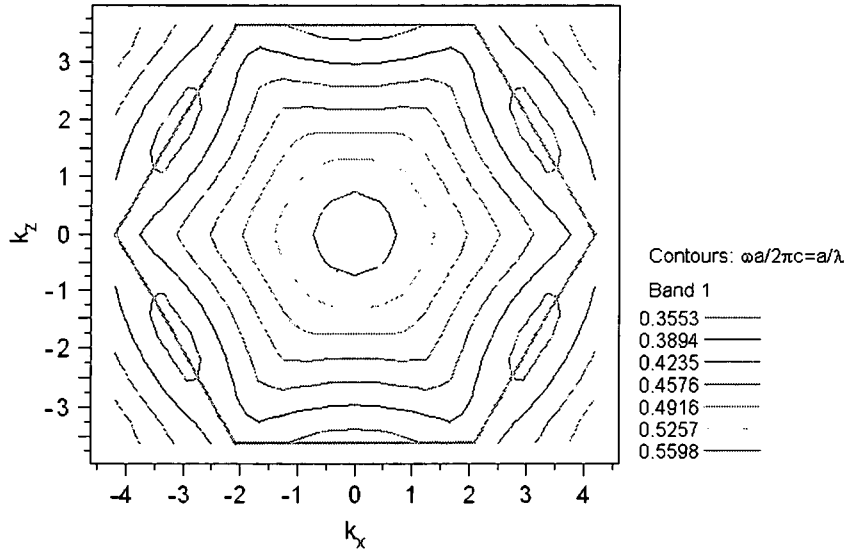
(a)



(b)



(c)



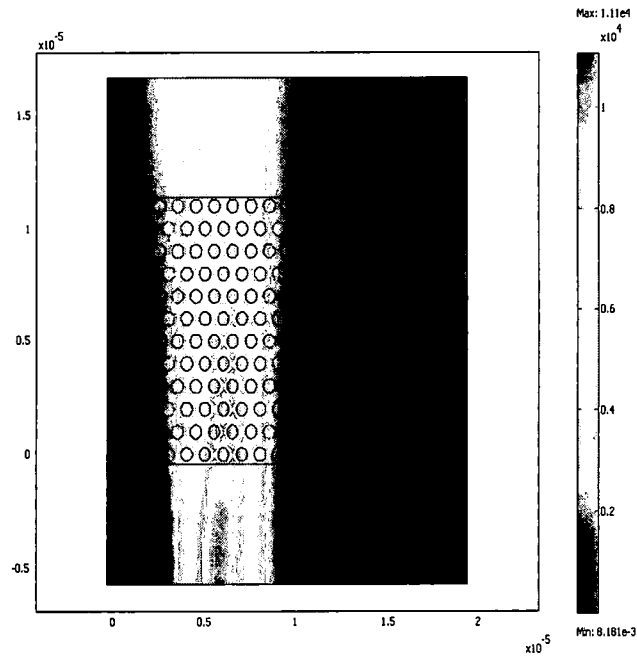
(d)

Figure 4.10 Contour representation of the equi-frequency surface for the 2nd band of the triangular lattice with isotropic materials of radii, r (a) 0.2, (b) 0.3 , (c) 0.4 and (5) 0.5 micron . The refractive indices are $n_{\text{rod}} = 1.64$ and $n_{\text{host}} = 2.55$ and the radius of the rods $r = 0.4a$

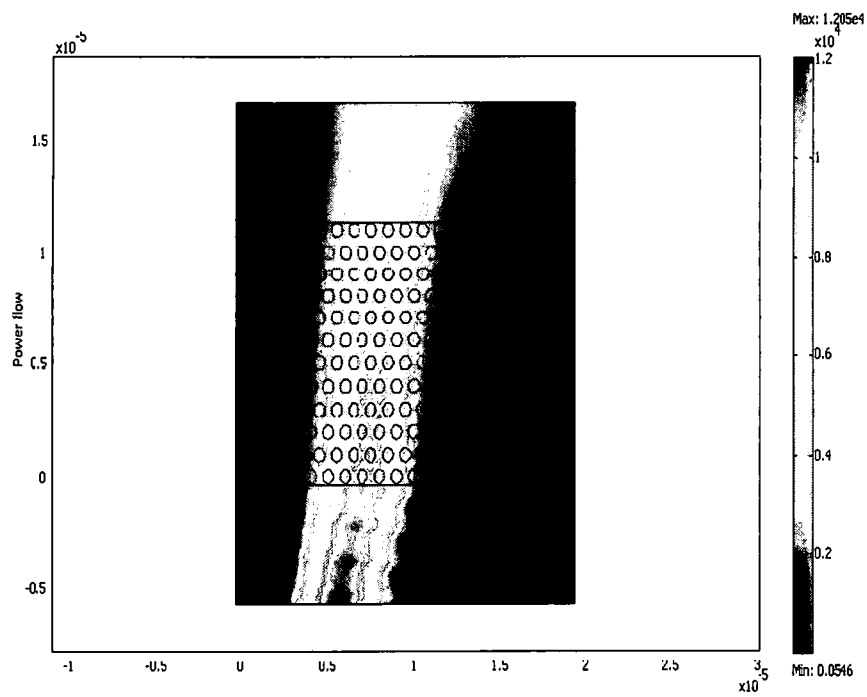
Now after analyzing the EFS of radii , 0.1 to 0.5 micron , we found that the normalized frequency, a/λ , 0.325 for radius 0.3 μ have the largest flat surface where the incident beam will be collimated within the divergence angle of 4° . In this case the maximum incident angle will be collimated within this range is 14° That means if an incident light beam propagation close to y-axis with normalized frequency of 0.325 then maximum input angle would be 14° that will be self-collimated inside PhC within 4° deviation. Now we compare our theoretical results with the simulations results by using FDTD and FE.

4.3.2:FE Modeling Results

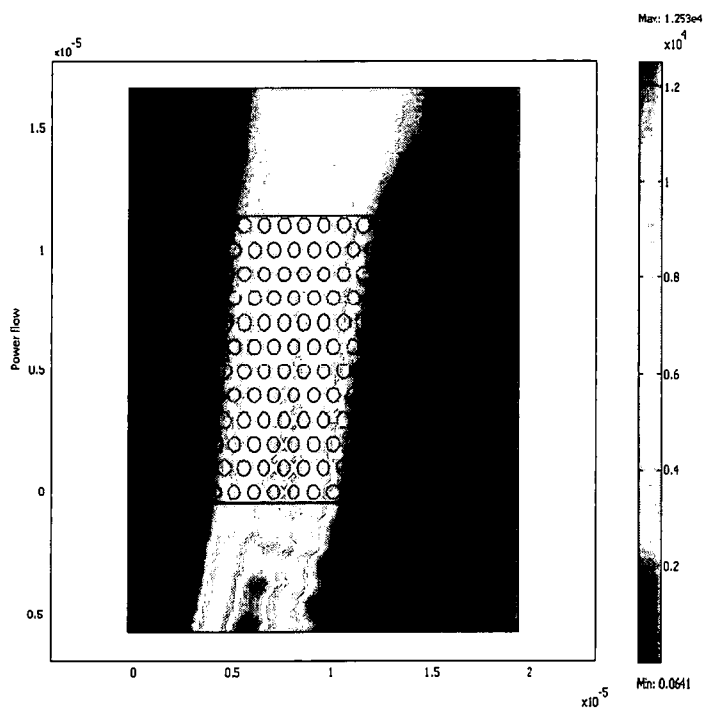
To model the beam propagation through our lattice, we simulated $3\mu\text{m}$ wide Gaussian beam and launch it $5.35\mu\text{m}$ away from the input interface. Figure 4.11 (a-e) shows the outline of the PhC used in the simulations. The width and the length of the structure is $20a$ and $12a$ respectively. The refractive index of the background host and the cylinder rod are set to the same values as in the previous calculation, i.e., 2.55 and 1.64. The field distributions for the TM mode at different angles are shown in the following series of figure 4.5(a-f).



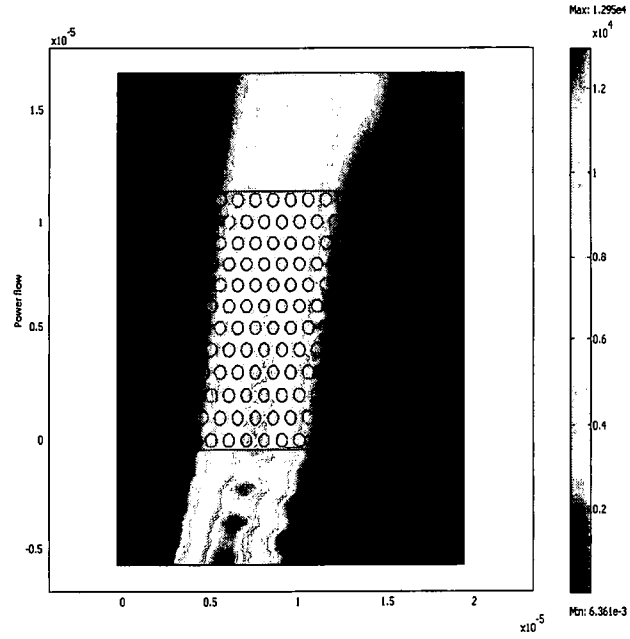
(a)



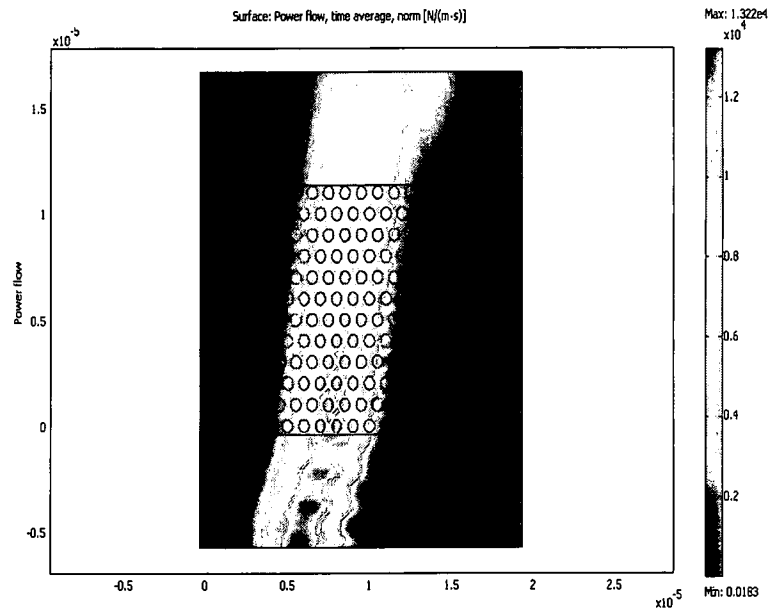
(b)



(c)



(d)



(e)

Figure 4.11 : Power flow through the Triangular PhC from air with the incident angle of a) 0° , b) 10° , c) 12° , d) 14° , and e) 15° respectively.

As we have theoretically calculated that the maximum incident angle that will be self-collimated inside the triangular lattice with minimum deviation of 4° if we chose the cylinder radius 0.3 and the normalized frequency, a/λ , 0.325. The power flow through the crystal from the air for the TM mode of incident angles of 0° , 10° , 12° , 14° and 15° are shown in figure 4.11.(a-e) respectively. We have a good collimated beam till 14° with divergence angle from normal is less than 4° . Now if the incident angle is 15° then the deviation angle is 7° . So the simulation result is confirmed our theoretical value.

CHAPTER V

SELF-COLLIMATION IN PHOTONIC CRYSTAL WITH ANISOTROPIC CONSTITUENTS

The shape of the PhC isofrequency dispersion surface is the essential feature determining the self-collimation and can be optimized and manipulated, for instance, by lattice symmetry, material parameters and the geometry shape of the constituents [2]. In constituent isotropic materials, the electric polarization and refractive index are independent of the wave propagation direction; however, in anisotropic materials, both polarization and refractive index depend on the wave propagation direction. Therefore the dispersion surfaces of PhCs made with anisotropic constituent materials provide another degree of freedom for improving the performance of photonic devices.

Anisotropic materials in the PhC were first studied by Zabel and Stroud[26] in 1993. The authors demonstrated that the anisotropy can reduce the band gap of PhC by breaking the degeneracies of bands with different polarizations. They even found a case where sufficient anisotropy would close the gap altogether. In 1998, Li *et al.* reported a large absolute band gap in two dimensional (2D) PhCs made of anisotropic materials [74,75]. Recently, Alagappan et al. extensively explored anisotropic materials and among other results, reported the decoupling of the two polarizations on 2D PhC made of anisotropic materials[76]. In our research we study PhCs with mixtures of anisotropic

materials; both the inclusions and the background may be anisotropic. To demonstrate the significance of anisotropic materials we report the results on self-collimating phenomena. In particular we examine the degree of self-collimation versus the range of input angles. Moreover, we identified a potential material, which is an anisotropic, organic ionic salt crystal that goes by the name 4-dimethylamino-N-methyl-4-stilbazolium-tosylate, which is normally referred to by the acronym DAST. Photo-induced chemical reactions can change the optical properties[77] and the refractive index of this material. However, the index contrast is modest and thus does not produce a full band gap. In DAST either or both constituent materials can be anisotropic and the anisotropy can be controlled to some degree by the radiation dose. Our choice of DAST is motivated by planned experiments on Terahertz (THz) generation, where the nonlinear optical rectification is very strong with d_{111} approximately 500 pm/V near a wavelength of 1500 nm[78].

5.1 Structure and Properties of DAST Crystals :

Depending on the growth condition, DAST crystallizes in a centrosymmetric orange colored hydrated phase or in a noncentrosymmetric red colored anhydrous phase and it belongs to the monoclinic point group m . The crystallographic a -, b - and c -axes and the dielectric x_1 , x_2 and x_3 axes are depicted in figure 5.1. The crystallographic b -axis and the dielectric x_2 axis are normal to the mirror plane. The crystallographic a -axis makes an angle of 92.2° with the crystallographic c -axis. The angles between the dielectric principal axes x_1 and x_3 and the crystallographic axes a and c are 5.4° and 3.2° respectively. The polar axis of the crystal is along x_1 .

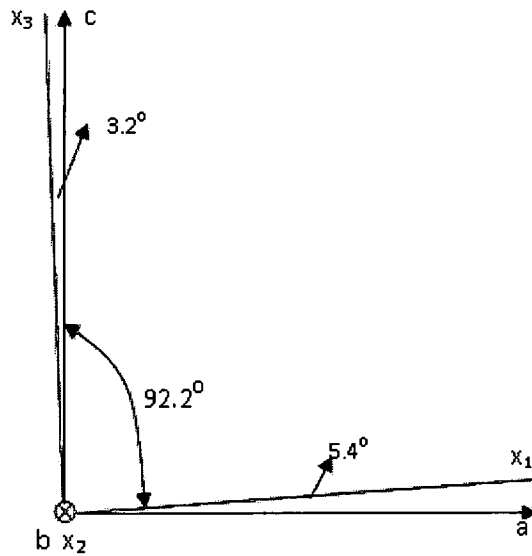


Figure 5.1 Crystallographic a, b c axes and the dielectric x_1, x_2 and x_3 principal axes in DAST.

In the present study we model a 2D square lattice photonic crystal with anisotropic dielectric constants. The specific dielectric parameters used in this paper are motivated by recent results on DAST, which is a biaxial anisotropic crystal. DAST undergoes a large change of its refractive indices when irradiated with visible light. By using the multiple-beam interference laser lithography a periodic structure can be written into the host material. By the choice of beam geometries the volume that is bleached can be either an inclusion-like region or a host medium region. To illustrate the dispersion effects of the refractive index ellipsoid we simplify the topology of the structure by using circular rods for the shape of the material embedded in the host. Bleached DAST rod-like cylinders are periodically embedded in the non-bleached DAST host material. Bleached and non-bleached regions are both anisotropic, although the bleached material is nearly isotropic.

The data in Table 5.1 illustrate the large changes induced in the refractive index for bleached and unbleached DAST. DAST crystals can be grown in relatively large sizes with good optical quality [79] and the combinations of low dielectric constant and high nonlinearity make DAST crystals interesting materials for high speed modulation and frequency mixing applications, including generation and detection of THz radiation[80]. We can exploit the relatively large change of the refractive index to modify the EFS and in particular, the angular range for acceptable self-collimation in the PhC can be improved.

Table 5.1: Principal refractive indexes for DAST Ref [9].

$\lambda(\text{nm})$	n_1		n_2		n_3	
	Crystal	Bleached	Crystal	Bleached	Crystal	Bleached
633	2.55	1.641	1.784	1.616	1.597	1.629
830	2.35	1.613	1.659	1.603	1.583	1.611
1300	2.16	1.591	1.620	1.614	1.575	1.592
1500	2.13	1.580	1.614	1.608	1.571	1.588

5.2 : Modeling

Maxwell's equations can be reduced to scalar equations under the condition that a principal axis is parallel to the rod axis. In this case we assume the spatially periodic, dielectric function has the form

$$\tilde{\epsilon}(\vec{x}) = \begin{bmatrix} \epsilon_{xx} & \epsilon_{xy} & 0 \\ \epsilon_{yx} & \epsilon_{yy} & 0 \\ 0 & 0 & \epsilon_{zz} \end{bmatrix}. \quad 5.1$$

The axis of the rods is along the z -axis and the other two axes can be rotated with respect to the x - and y axes. For 2D in-plane propagation of waves with the dielectric tensor in Eq. (1), Maxwell's equations are reduced to scalar wave equations. For the E-field parallel to the rods (along the axis labeled z), the wave equation takes the scalar form

$$\nabla_{\perp}^2 E + k^2 \epsilon_{zz} E = 0. \quad 5.2$$

This has the same solutions as the isotropic case and will be used as a comparison case in this paper. For the H field parallel to the rods the scalar wave equation takes the form

$$\bar{\nabla}_{\perp} \cdot \tilde{\eta} \bar{\nabla}_{\perp} H + k^2 H = 0.$$

5.3

The operators are restricted to the x - y plane and k is the free space wave number. The inverse of the rank 2 sub-matrix is given by

$$\tilde{\eta} = \begin{bmatrix} \epsilon_{xx} & \epsilon_{xy} \\ \epsilon_{yx} & \epsilon_{yy} \end{bmatrix}^{-1}, \quad 5.4$$

Equ. 5.3 has contributions mixing the diffraction in the x - y plane which can dramatically alter the spatial dispersion. We concentrate here on the solution of Eq. (3) by using the plane-wave expansion method and following the same steps that we previously show in chapter 2, the wave equation in the plane-wave form is written as

$$\sum_{\vec{G}'} (\vec{G} - \vec{k}) \cdot \tilde{\eta}(\vec{G} - \vec{G}') \cdot (\vec{G}' - \vec{k}) H_{\vec{G}} + k^2 H_{\vec{G}} = 0, \quad 5.5$$

The radius of the circular cylinders is r and the lattice constant is a . As usual, the lattice constant is used to scale the cylinder radius.

$$\eta_{ij}(\vec{G}) = \left(\frac{\pi r^2}{a^2} \Delta\eta_{ij} + \eta_{ij}(\text{host}) \right) \delta_{\vec{G}, \vec{0}} + 2\Delta\eta_{ij} \frac{\pi r^2}{a^2} \frac{J_1(Gr)}{Gr}, \quad 5.6$$

where $\Delta\eta_{ij} = \eta_{ij}(\text{rod}) - \eta_{ij}(\text{host})$ and $i, j = x, y$.

The solution of Eq. 5.5 and the corresponding isotropic medium case are straightforward. We construct isofrequency curves for specific case and discuss the implication for self-collimation in the following section. In particular we examine the second band, which has a self-collimation feature.

5.3 : RESULTS

Our discussion is restricted to a 2D square lattice of circular rods with radii varied from $r=0.1a$ to $0.5a$, where a is the period of the lattice. The DAST crystal index parameters are varied for n_1 between 2.55 and 1.64 and for n_2 between 1.78 and 1.62, respectively, for the background medium going from the unbleached to the bleached states. We chose the condition $\epsilon_{zz} = n_z^2$ with $n_z=2.55$ for an isotropic response (i.e. the E-field is parallel to the rods, which are oriented along the principal axis for n_1). The refractive indices of the bleached holes at a wavelength of 633 nm are $n_1 = 1.64$ and $n_2 = 1.62$, which corresponds to a nearly isotropic medium. The hole radius and the background anisotropy are varied to optimize the angular dispersion for the largest incident angle that can be self-collimated inside the crystal. In the following we present dispersion surfaces for this crystal. The birefringence ratio defined as n_1/n_2 is 1.43 for unbleached DAST at 663 nm.

For bleached DAST the birefringence ratio is reduced to 1.01.

We now turn our attention to study the effect of anisotropic dielectrics on the self-collimation of light in the PhC. We first determine the maximum input angle that is collimated to within a certain angle for a cylinder radius $0.2a$, as a function of the anisotropy ratio. The birefringence ratio, n_1/n_2 , is changed only for the background refractive indices while keeping the cylinder birefringence ratio constant. Figure 5.2 a-c shows the second-band contours while varying the index ratio. The curvature of the isofrequency curvature along the k_x axis is much larger than the curvature along the k_y axis in our figures. To achieve high collimation of the optical beams in the PhC over the largest range of incident divergence angles the propagation closer to the x-axis is desirable. We determine the angles of refraction using Snell's law. For an incident beam propagating close to the x-axis, a range of transverse wave vectors, k_y , is used to determine the degree of self-collimation. The self-collimation of the beam is defined in terms of the group velocity, as discussed in the previous chapter. The values of the refractive index in Figure 2a-2c are $n_2 = 1.78, 1.9$ and 2.2 . As n_2 decreases the shape of the EFS are elongated more along the x-axis. The contours parallel to the k_y axis for $a/\lambda = 0.38$ have sufficiently flat contours over a range of frequencies and the range becomes smaller as the birefringence ratio is reduced toward the isotropic case. The curvature of the isofrequency contours is much greater for propagation along the x-axis until the birefringence is sufficiently reduced where it approaches the value quoted above for an isotropic material, as in Figure 5.1(c).

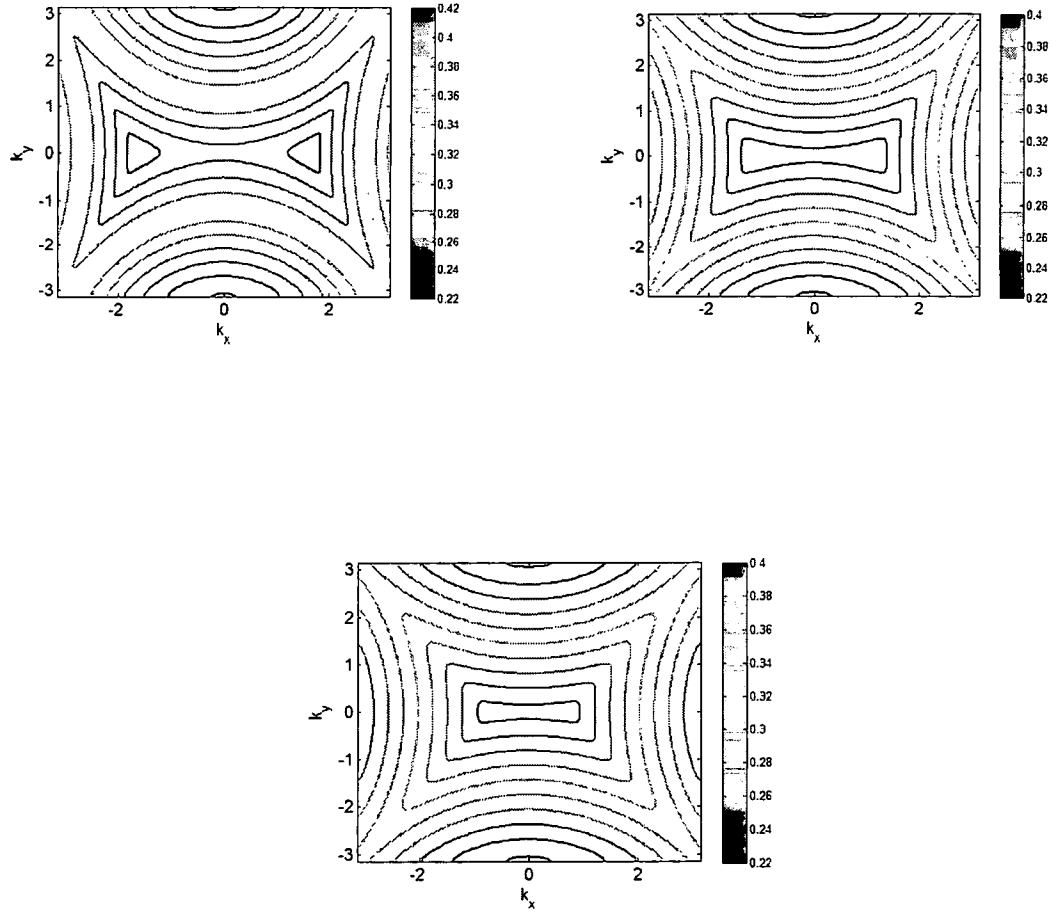


Figure 5.2: Second band isofrequency contours. The index n_1 is fixed at 2.55 and the values of the n_2 are (1.78 1.9, 2.2) for $r=0.2a$.

In figure 5.3 the dependence of the angular deviation of the group velocity from normal is plotted against the corresponding input angle. This data is extracted from the isofrequency curve by computing the gradient of the frequency. The line is nearly linear from normal incidence (0) to close to the maximum deviation of θ_g . At an input angle near 25 degrees the deviation angle is about 6 degrees, while at 12.5 degrees the deviation is about 3 degrees. Exploiting a region where large input angle ranges are found that can lead to a larger deviation angle, as in figure 5.3.

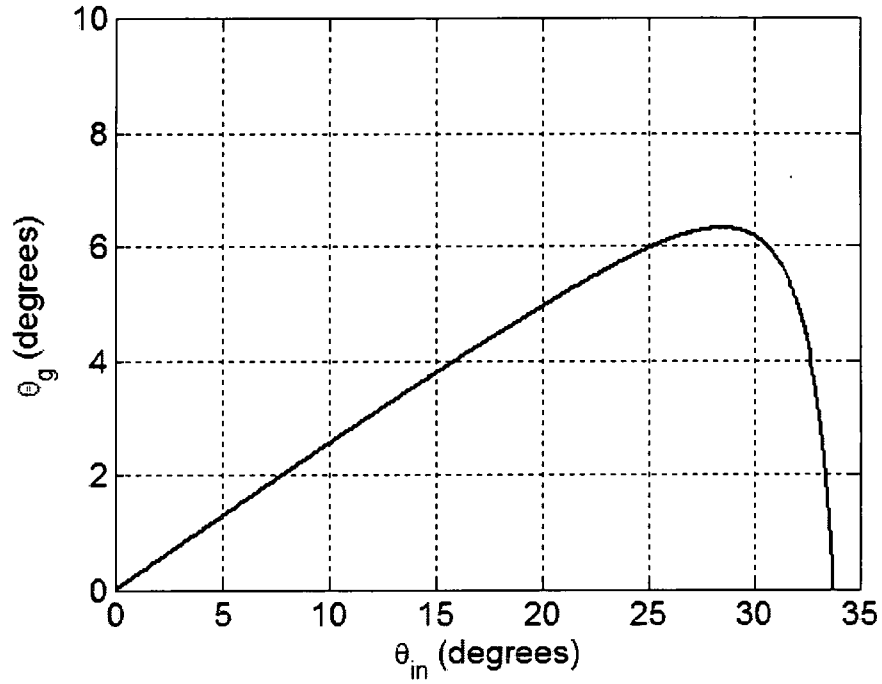


Figure 5.3: Curve for the case $r=0.15a$ showing the maximum of the angular deviation of the group velocity.

We explore the relationship between the input angles and the angular deviation of the group velocity for a range of birefringence ratios in figure 5.4. As in figure 5.3 for a fixed frequency we extract the maximum incidence angle from air to the PhC where the deviation of the group velocity from the x direction. The results for a range of parameters are summarized in figure 5.4 for the fixed frequency $a/\lambda = 0.38$ and for the fixed hole radius $0.2a$. The curves are generated by adjusting the frequency and determining the maximum of θ_g . The maxima of θ_g are almost linearly related to the input angles at the maximum. The larger anisotropies do better for larger input angles by better collimating a divergent input beam. The solid line is the isotropic case for a rod index of 2.55.

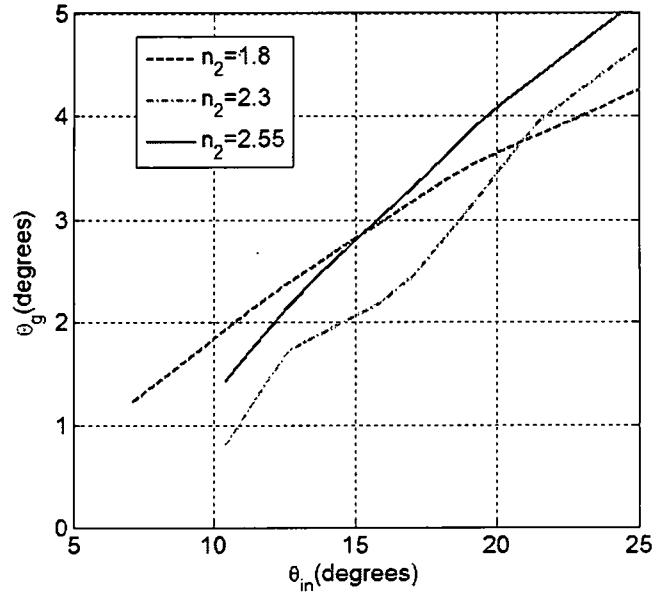


Figure 5.4: The maximum angular deviation of the group velocity versus the incident angle at that point for selected values of the index n_2 . Cylinder radii are $r=0.2a$.

The cylinder radii are another strong parameter affecting the dispersion surfaces. In figure 5.5 we summarize the affect of the cylinder radii by plotting the maximum angular deviation of the group velocity from the surface normal. Two cases of self-collimation are plotted here. The solid curve is for the isotropic medium case and the dashed curves are for the anisotropic medium case. There are two curves for each case, the upper curve allows a maximum deviation of 6.5 degrees and the lower curve allows a maximum deviation of 4.5 degrees. An input angle of 30 degrees was found for the anisotropic case and a cylinder radius around $r=0.2a$. The anisotropic and the isotropic cases are nearly identical for a radius of $0.5a$. The maximum deviation for isotropic media can be maintained for a range of radii between $0.2a$ and $0.4a$. Larger input angles are found for cylinder radii between $0.1a$ and $0.3a$.

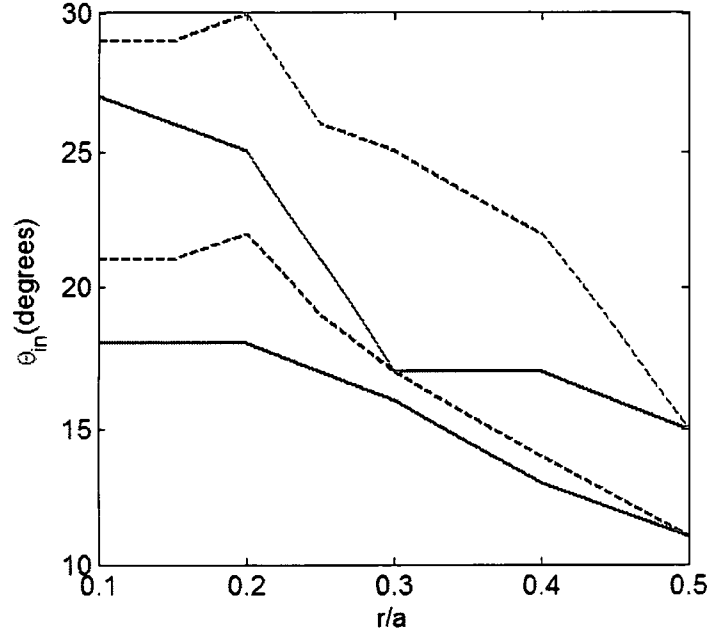


Figure 5.5: Input angle for the maximum deviation of the group velocity from normal versus the scaled cylinder radius.

5.4 : Simulation Results

In this section, we will demonstrate the self-collimating phenomenon for an incident angle as large as 18 by numerical simulation based on the finite element method . By above analysis , we found that the anisotropy ration in the background of 0.70 and $r/a = 0.2$ optimize the anisotropic square lattice to provide the self-collimated beam with the maximum incident angle of about 20 with the divergence angle maintain below 4° . We maintained the cylinder anisotropy constant of 0.98.

To model the beam propagation through our lattice, a Gaussian beam with a width of $3\mu\text{m}$ was launched $6.375\mu\text{m}$ away from the input interface along the ΓX direction. We examine the beam propagation for the H polarization which should be governed by the EFS . Normalized frequency we choose is $a/\lambda = .38$.

Now in figure 5.6 it shows the power flow for the normal incident. As expected beam will not diverge and go through the crystal . Fig 5.7 shows the normalized power in the input surface (blue) , center of the crystal (red) and output surface (green) . Power lose for from the input is only 8%.

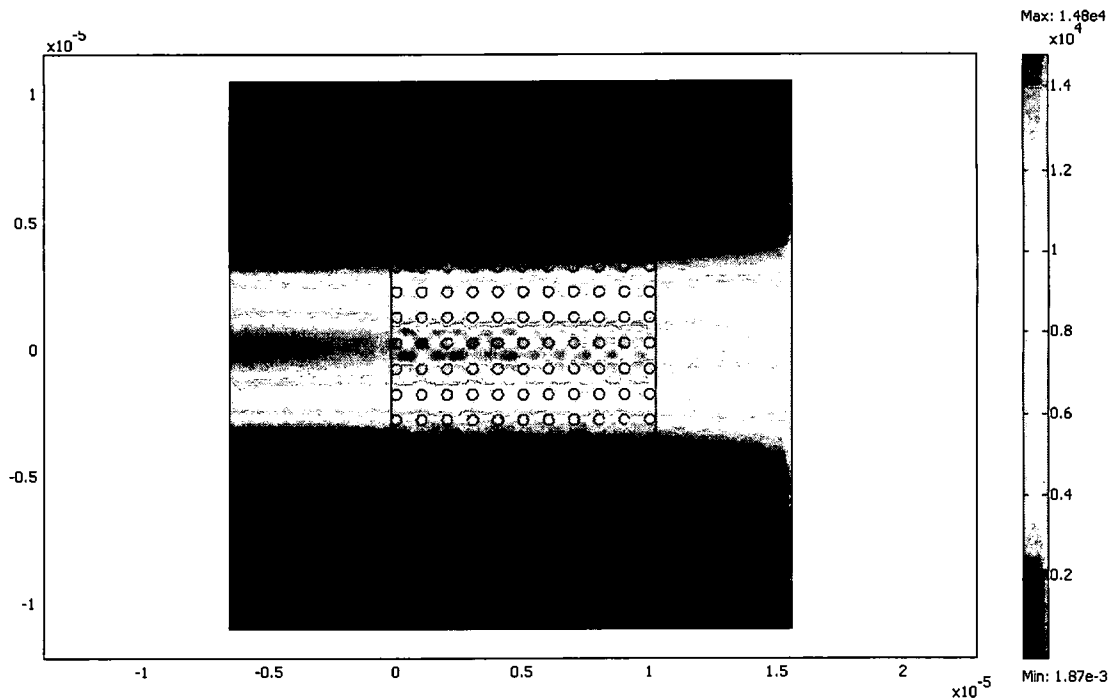


Figure 5.6 : Power flow through the square PhC of anisotropic constituents from air with the incident angle of 0° . The index n_1 is 2.55 and n_2 is 1.78 for $r = 0.4a$.

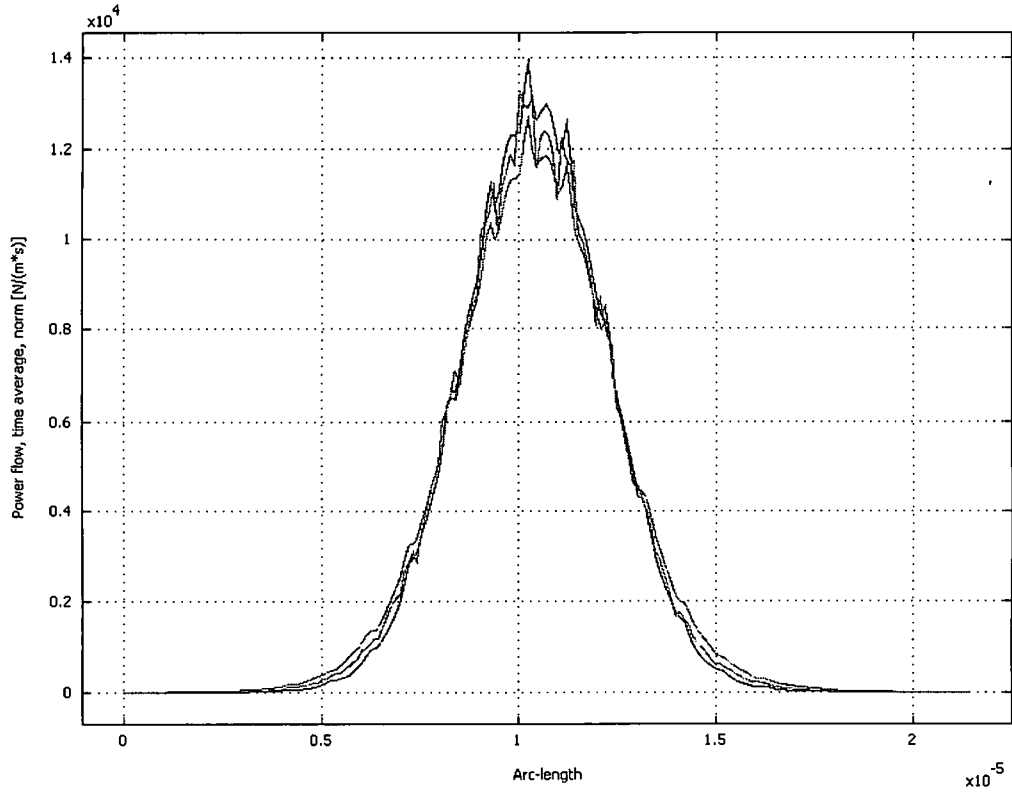
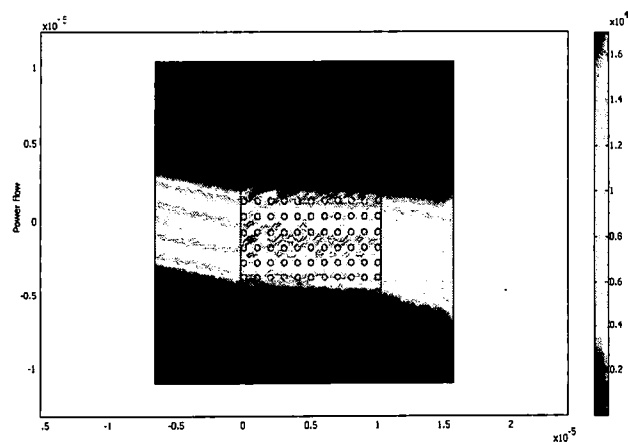
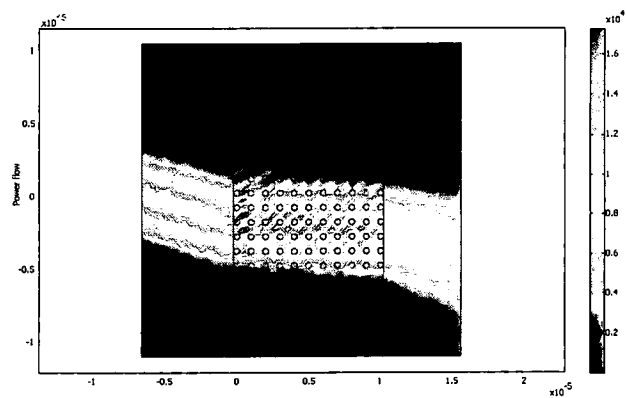


Figure 5.7 : Normalized power in different region of the square PhC of anisotropic constituents from air with the incident angle of 0° . Blue , red and green curves represent the power in entrance surface, middle of the crystal and the exit surface respectively. The index n_1 is 2.55 and n_2 is 1.78 for $r = 0.4a$.

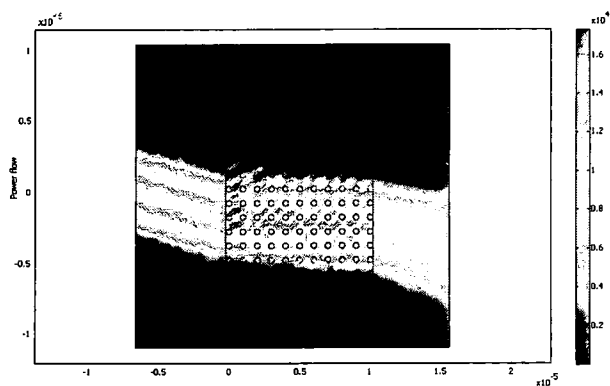
Now in figure 5.8a-d shows power flow of the Gaussian beam incident on the crystal of 10° , 15° , 18° , 20° and 22° respectively. In these cases the beam is collimated along the x-direction and the divergence angle maintain below 6.5. So our simulation result is perfectly match with our theoretical prediction. But if we increase the angle we found that the beam quality going down as the power lost for incident angle of 22° around 40% as we have depicted in figure 5.9 .



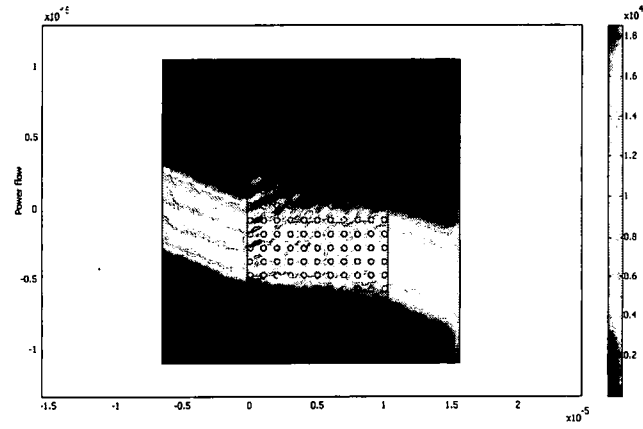
(a)



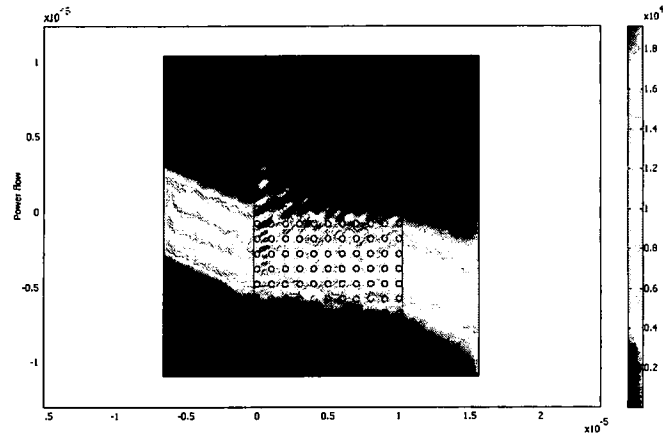
(b)



(c)



(d)



(e)

Figure 5.8 : Power flow through the square PhC of anisotropic constituents from air with the incident angle of a) 10° , b) 15° , c) 18° d) 20° and e) 22° . The index n_1 is 2.55 and n_2 is 1.78 for $r = 0.4a$.

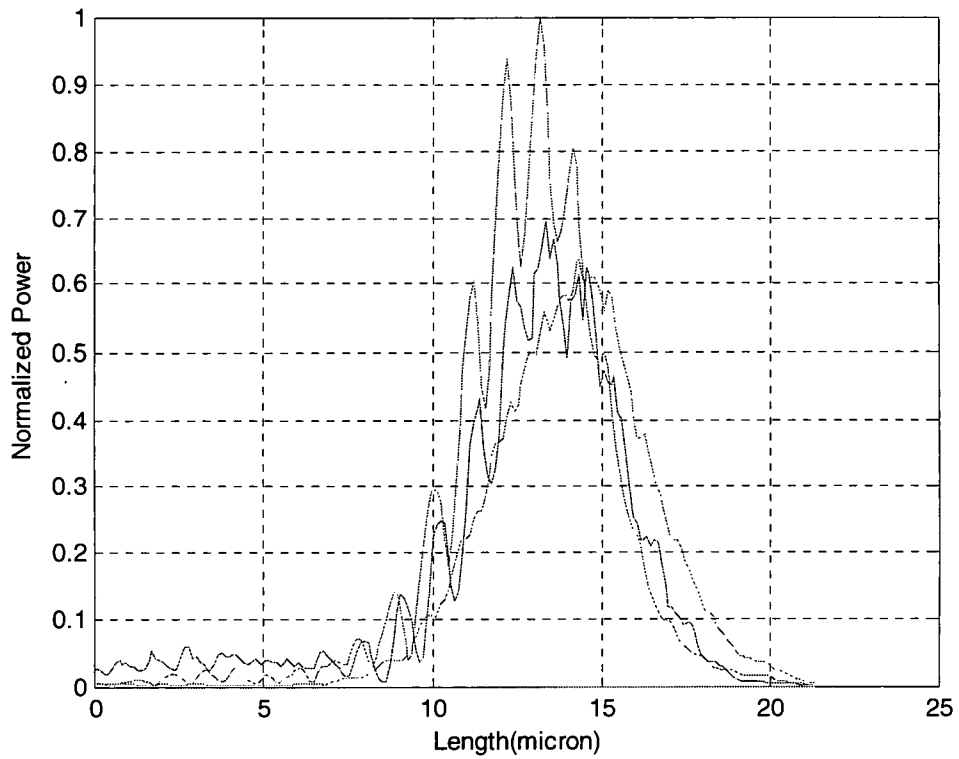


Figure 5.9 Normalized power in different region of the square PhC of anisotropic constituents from air with the incident angle of 22° . The index n_1 is 2.55 and n_2 is 1.78 for $r = 0.4a$.

Now we came to this conclusion that the advantage of introducing the anisotropy in the photonic crystal give us more working space compare to isotropic case where we will get maximum input angle for the collimated beam was 14° .

CHAPTER VI

SELF-COLLIMATION OPTIMIZATION BY ROTATING CRYSTAL AXES

In previous chapter we investigate the isofrequency curves in a highly birefringent medium with refractive index parameters chosen to correspond DAST crystal parameter [Table 5.1] . In this chapter we introduce another degree of freedom to engineer the EFS for the same DAST crystal. This additional freedom is rotating the crystallographic axes relative to the photonic crystal principal axes. In this chapter we investigate this property and how it enhances the quality of the self-collimated beam. In this chapter, we shall present a theoretical and computational analysis of the band structure and the isofrequency surfaces for the 2D DAST crystal having square lattice by rotating the orientation of the principal axes of the anisotropic material.

6.1. Theory and Formalism

For convenient we rewrite the Maxwell equations for nonmagnetic media in charge free space are :

$$\begin{aligned}\bar{\nabla} \times \bar{E}(\bar{r}, t) &= -\mu_0 \frac{\partial \bar{H}(\bar{r}, t)}{\partial t}, \\ \bar{\nabla} \times \bar{H}(\bar{r}, t) &= -\varepsilon_0 \tilde{\tilde{\varepsilon}}(\bar{r}) \frac{\partial \bar{E}(\bar{r}, t)}{\partial t},\end{aligned}\tag{6.1}$$

where ϵ_0 and μ_0 are the permeability and permittivity of the vacuum. The position dependent relative dielectric tensor, $\tilde{\epsilon}(\vec{r})$ is a 3 x 3 matrix and can be expressed as ,

$$\tilde{\epsilon}(\vec{x}) = \begin{bmatrix} \epsilon_{xx} & \epsilon_{xy} & \epsilon_{xz} \\ \epsilon_{yx} & \epsilon_{yy} & \epsilon_{yz} \\ \epsilon_{zx} & \epsilon_{zy} & \epsilon_{zz} \end{bmatrix}. \quad 6.2$$

The principal axes relative dielectric constants are expressed in terms of the refractive indices as: $\epsilon_{xx} = n_x^2$, $\epsilon_{yy} = n_y^2$ and $\epsilon_{zz} = n_z^2$. The crystallographic axis of the PhC and the principal coordinate system of the anisotropic material or the dielectric axes are defined by a,b, c axes and x_1, x_2, x_3 axes respectively as we have mention in chapter 5. As we mention in chapter 5 , the general orientation of these crystal axes is such that none of the crystallographic axes are in the along the polar axes and these can easily represented by the Eulerian angles , figure 6.1. The polar axis of the crystal is along the dielectric axes. In figure 6.2 the fixed system is denoted in lower case (a,b,c) which is representing the dielectric axes and the rotated system is denoted in upper case letters (X_1, X_2, X_3). A, α is the angle between the a-axis and the line of nodes N, β is the angle between c-axes and X_3 and the γ is the angle between X_1 and N.

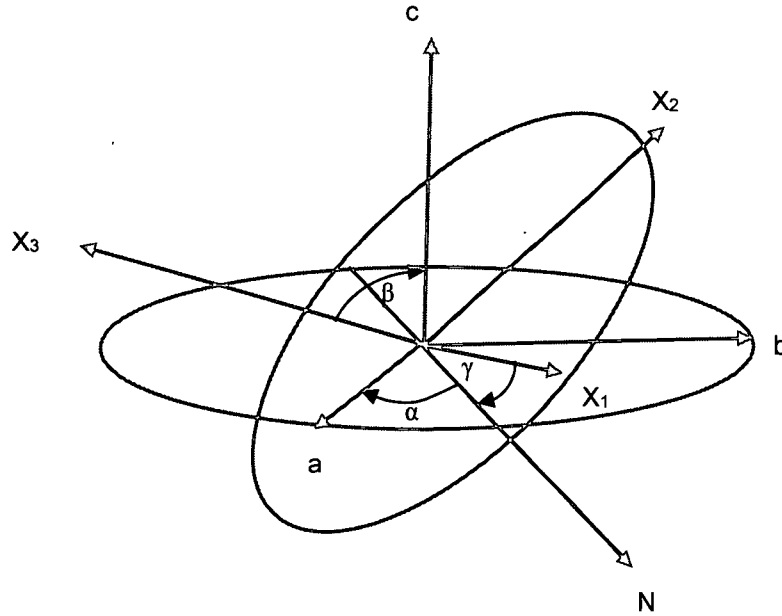


Figure 6.1: Rotation of the axes and the definition of the angles.

Now if we introduce an rotation operator , $R(\theta)$, a 3x3 rotation matrix for planar rotation around the principal axis with a clockwise rotation of angle $\theta(\alpha,\beta,\gamma)$, then it can be expressed as,

$$R(\theta) = \begin{bmatrix} \cos \gamma & -\sin \gamma & 0 \\ \sin \gamma & \cos \gamma & 0 \\ 0 & 0 & 1 \end{bmatrix} \begin{bmatrix} 1 & 0 & 0 \\ 0 & \cos \beta & -\sin \beta \\ 0 & \sin \beta & \cos \beta \end{bmatrix} \begin{bmatrix} \cos \alpha & -\sin \alpha & 0 \\ \sin \alpha & \cos \alpha & 0 \\ 0 & 0 & 1 \end{bmatrix}, \quad 6.3$$

after carrying out the matrix multiplication ,

$$R(\theta) = \begin{bmatrix} \cos \gamma \cos \beta \cos \alpha - \sin \gamma \sin \alpha & -\cos \gamma \cos \beta \sin \alpha - \sin \gamma \cos \alpha & -\cos \gamma \sin \beta \\ \sin \gamma \cos \beta \cos \alpha + \cos \gamma \sin \alpha & -\sin \gamma \cos \beta \sin \alpha + \cos \gamma \cos \alpha & -\sin \gamma \sin \beta \\ \sin \beta \cos \alpha & -\sin \beta \sin \alpha & \cos \beta \end{bmatrix}. \quad 6.4$$

since the polar axes are along the dielectric axes, we can replace the dielectric coordinate system (X_1, X_2, X_3) by the coordinate system of the PC (x, y, z) . Inserting equation 6.2 into Equ. 6.1 and 6.2 , then the Maxwell equations become,

$$\frac{\partial}{\partial y} E_z = -\mu_0 \frac{\partial H_x}{\partial t}, \quad 6.5$$

$$\frac{\partial}{\partial x} E_z = \mu_0 \frac{\partial H_y}{\partial t}, \quad 6.6$$

$$\frac{\partial}{\partial x} E_y - \frac{\partial}{\partial y} E_x = -\mu_0 \frac{\partial H_z}{\partial t}, \quad 6.7$$

$$\frac{\partial}{\partial y} H_z = \epsilon_0 \epsilon_{xx} \frac{\partial E_x}{\partial t} + \epsilon_0 \epsilon_{xy} \frac{\partial E_y}{\partial t} + \epsilon_0 \epsilon_{xz} \frac{\partial E_z}{\partial t}, \quad 6.8$$

$$\frac{\partial}{\partial x} H_z = -\epsilon_0 \epsilon_{yx} \frac{\partial E_x}{\partial t} - \epsilon_0 \epsilon_{yy} \frac{\partial E_y}{\partial t} - \epsilon_0 \epsilon_{yz} \frac{\partial E_z}{\partial t}, \quad 6.9$$

$$\frac{\partial}{\partial x} H_y - \frac{\partial}{\partial y} H_x = \epsilon_0 \epsilon_{zx} \frac{\partial E_x}{\partial t} + \epsilon_0 \epsilon_{zy} \frac{\partial E_y}{\partial t} + \epsilon_0 \epsilon_{zz} \frac{\partial E_z}{\partial t}. \quad 6.10$$

Now from the above set of equations, it is clear that all field terms are coupled. Furthermore, classifications of transverse electric (TE) polarization, corresponding to the set (H_x, H_y, E_z) and transverse magnetic (TM) corresponding to (E_x, E_y, H_z) are possible only if the tensor elements ϵ_{xz} , ϵ_{zx} , ϵ_{yz} , and ϵ_{zy} are zero [1]. If the $\beta=0$ and $\gamma=90$ which means that the z axis coincides with the c axes and b axis in the x - y plane of the PhC. Therefore rotating the principle axes in the x - y plane by an angle α the dielectric tensor becomes:

$$\tilde{\epsilon}(\vec{x}) = \begin{bmatrix} n_x^2 \cos^2 \alpha + n_y^2 \sin^2 \alpha & (n_y^2 - n_x^2) \cos \alpha \sin \alpha & 0 \\ (n_y^2 - n_x^2) \cos \alpha \sin \alpha & n_x^2 \sin^2 \alpha + n_y^2 \cos^2 \alpha & 0 \\ 0 & 0 & n_z^2 \end{bmatrix}. \quad 6.11$$

For 2D in-plane propagation of waves with the dielectric tensor in Eq. 6.11, Maxwell's equation are reduced to scalar wave equations. For the E-field parallel (TE

case) to the rods, the wave equation takes the scalar form

$$\nabla_{\perp}^2 E + k^2 \varepsilon_{zz} E = 0. \quad 6.12$$

This has the same solution as the isotropic case. Therefore, the E-field finds itself in an isotropic configuration even the tensor orientation of the anisotropic material, i.e., the E-polarization is independent of rotation of the axis. For H-field (TM) parallel to the rods the scalar wave equation takes the form

$$\bar{\nabla}_{\perp} \cdot \tilde{\eta} \bar{\nabla}_{\perp} H + k^2 H = 0. \quad 6.13$$

The operators are restricted to the x-y plane and k is the free space wave number. The inverse of the rank w sub-matrix is given by

$$\tilde{\eta} = \begin{bmatrix} \varepsilon_{xx} & \varepsilon_{xy} \\ \varepsilon_{yx} & \varepsilon_{yy} \end{bmatrix}^{-1}. \quad 6.14$$

Equation 6.13 has contributions mixing the diffraction in the x-y plane which can dramatically alter the spatial dispersion. We concentrate here on the solution of Eq.6.13 by using the plane wave expansion method. The wave equation in the plane-wave form is written as

$$\sum_{\vec{G}'} \left(\eta_{xx} (\vec{G} - \vec{G}') (k_x + G_x) (k_x + G'_x) + \eta_{yy} (\vec{G} - \vec{G}') (k_y + G_y) (k_y + G'_y) \right) - \sum_{\vec{G}'} \left(\eta_{xy} (\vec{G} - \vec{G}') \left[(k_x + G_x) (k_y + G'_y) + (k_y + G_y) (k_x + G'_x) \right] \right) - \left(\frac{\omega}{c} \right)^2 H_{\vec{G}} = 0. \quad 6.15$$

The radius of the circular cylinders is r and the lattice constant is a . As usual, the lattice constant is used to scale the cylinder radius.

$$\eta_{ij}(\vec{G}) = \left(\frac{\pi r^2}{a^2} \Delta \eta_{ij} + \eta_{ij}(\text{host}) \right) \delta_{\vec{G}, \vec{0}} + 2 \Delta \eta_{ij} \frac{\pi r^2}{a^2} \frac{J_1(Gr)}{Gr}, \quad 6.16$$

where $\Delta \eta_{ij} = \eta_{ij}(\text{rod}) - \eta_{ij}(\text{host})$.

6.2 FEM Modeling Results

A 2D square lattice of circular rods with radii varied from $r=0.1a$ to $0.4a$, where a is the period of the lattice. We used the DAST crystal parameters [Table 5.1] with refractive indices of n_1 vary from 2.55 to 1.64 and $n_2 = 1.78$ and 1.62, respectively, for the background medium going from the unbleached to the bleached states. We chose the condition the $n_1 = n_2$ for 2.55 for the hypothetical, isotropic material to compare the effects of anisotropy on the self-collimation results. The refractive indices of the bleached holes we choose are $n_{1h} = 1.62$ and $n_{2h} = 1.64$, which is a nearly isotropic medium. The hole radius, the background anisotropy are varied along with the rotation of the principal axis of 5 ,10 ,15 ,30 and 45 degrees, respectively to optimize the angular dispersion for the largest incident angle that can be self-collimated inside the crystal. The birefringence ratio is defined as n_1/n_2 .

In figure 6.2 and 6.3 we depict the TM band structure of the crystal for the H polarization where the rotation angle, α is t 0^0 and 30^0 respectively. Now compare this two figures it is clear that rotation the crystal open the band gap between 1^{st} and 2^{nd} band (the socalled direct band gap). Since we work on the 2^{nd} band , it is important to isolate the 2^{nd} band from the 1^{st} band. Otherwise both bands share the same isofrequency surfaces and then the plane wave will be coupled by both surfaces insided the crystal .

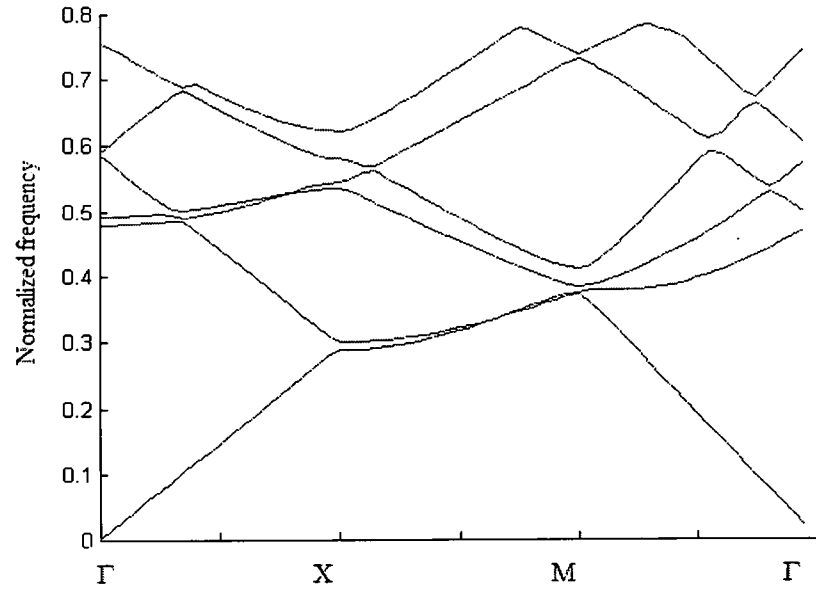


Figure 6.2: Band structure of the 2D DAST crystal of anisotropic cylinders arrayed in a square lattice of anisotropic background and $\alpha = 0^\circ$, $r=0.4a$, $n_{lb}=2.55$, $n_{2b}=1.78$, $n_{lc}=1.64$, $n_{2c}=1.62$.

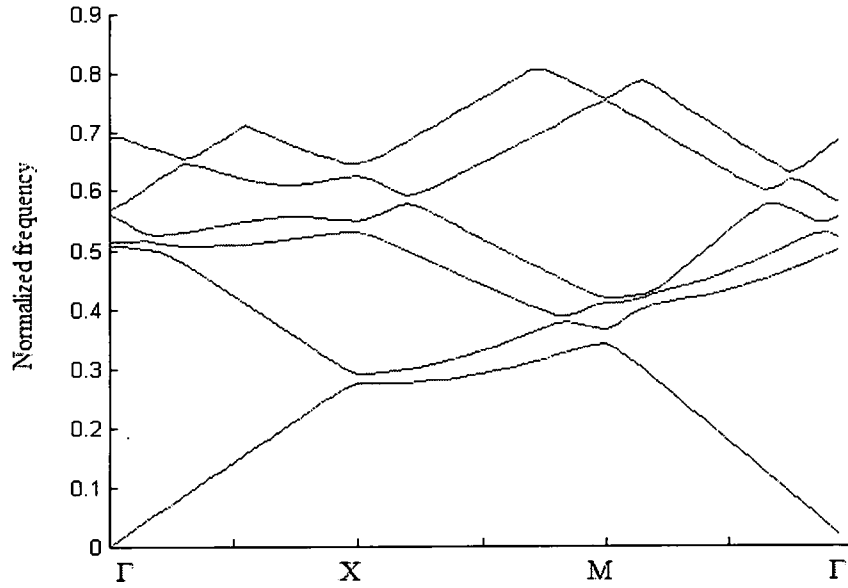


Figure 6.3 : Band structure of the 2D DAST crystal of anisotropic cylinders arrayed in a square lattice of anisotropic background and $\alpha = 30^\circ$, $r=0.4a$, $n_{lb}=2.55$, $n_{2b}=1.78$, $n_{lc}=1.64$, $n_{2c}=1.62$.

6.3 Transmission Spectra

We analyzed the transmission spectra properties by changing the thickness of the crystal from $10a$ to $40a$. The spectrum was calculated for the H polarization. The anisotropy ratio for the background is 0.69 and for the cylinder 0.98 and hole radius, r is $0.4a$. The rotation of the principal axis with respect to the dielectric axis is 30° in this case. The wave vector of the incident plane wave is parallel to the ΓX direction in this configuration. The transmission spectra of different thicknesses are presented in the figure 6.4 . In the figure blue , red and green spectra lines are for the transmission of thicknesses of $10a$, $20a$ and $40a$ respectively. In the band structure the gap between the 1st and 2nd band in the X point in the normalized frequency range from 0.28 to 0.3 . In the transmission spectra , transmittance is less than 0.15 are compared with those of the bandgaps in figure 6.3 although transmittance does not fall in this range for the thickness $10a$. However its sides become sharper and the transmission minimum becomes deeper when the number of the lattice layers is increased. Hence, the finite thickness of the assumed specimen plays an important role in defining the transmission characteristics.

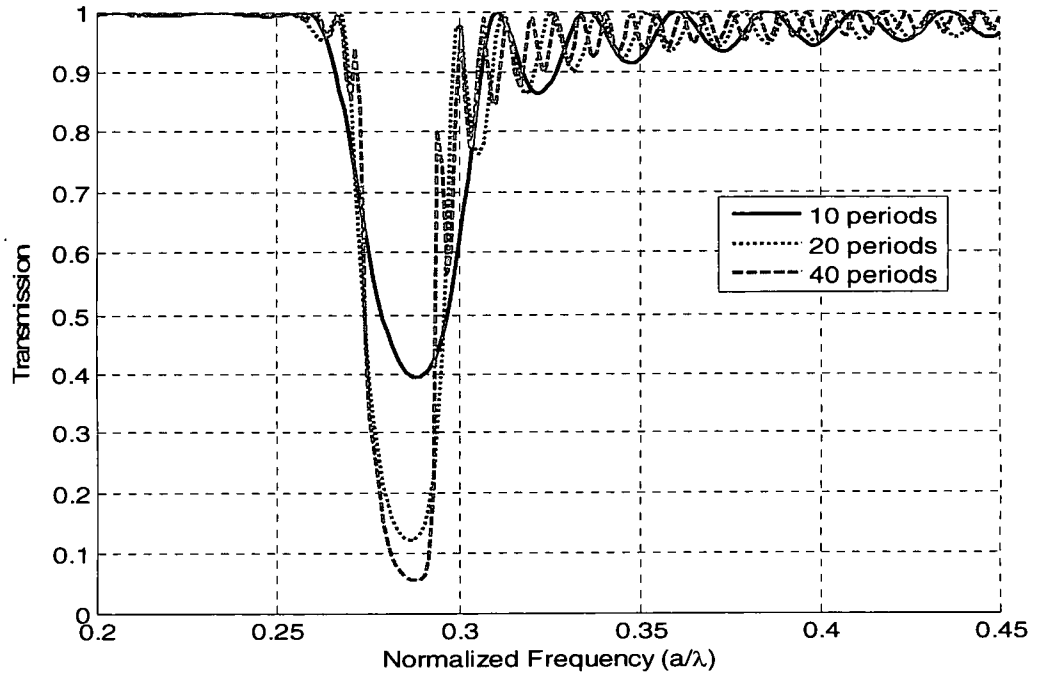


Figure 6.4: Simulated Transmission spectra for the TM mode in the ΓX direction in a 2D square DAST crystal of $\alpha = 30^\circ$, $r=0.4a$, $n_{1b}=2.55$, $n_{2b}=1.78$, $n_{1c}=1.64$, $n_{2c}=1.62$. Solid blue, dotted red and dashed green line represent the spectrum for 10, 20 and 40 layers respectively.

6.4 : Shape of EFS after rotation

Rotating the principal axis elongates the dispersion surfaces along the rotation axis. Figures 6.4a and 6.4b are the EFS of the second and third band without rotation of the crystal. In this case, EFS looks as usual that we had reported in chapter 5. Now in the 2nd band, we can find a wide flat surface at the normalized frequency of 0.38. Now we want to see how the rotation of the crystal affects this surface? If we introduced a rotation of the principal axis with respect to the dielectric axis by 10° and in figure 6.5a and 6.5b

shows 2nd and 3rd band of the EFS for this effect. Now for the 2nd band we found that the same normalized curve a/λ , 0.38 was elongated towards xy axis and more flatter than that of without rotation. Obviously this curve couple more light than without rotation. Though there is a dispersion surface of the same frequency in the 3rd band which is very small and it intercepts the corner of the same frequency surface. This is the cut off condition for the incident angle that can be collimated inside the crystal. Cylinder radius in here is $r=0.1a$.

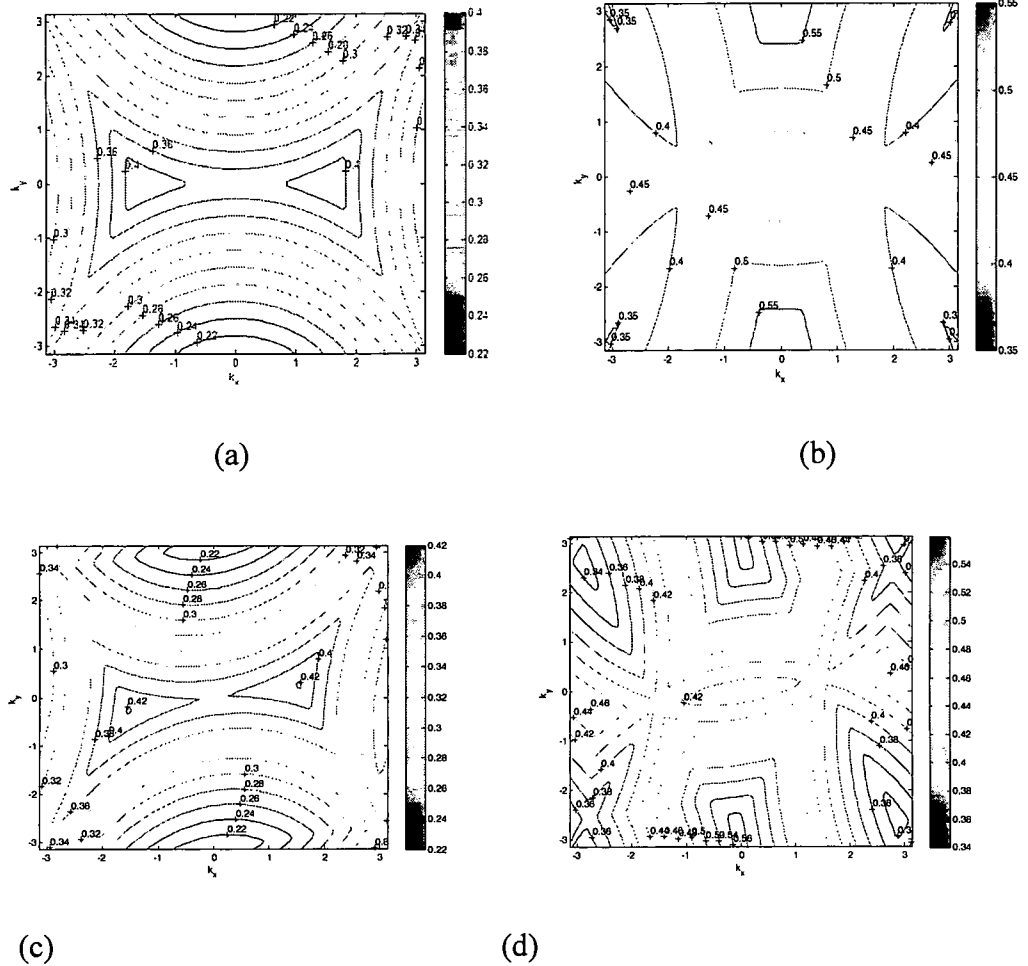
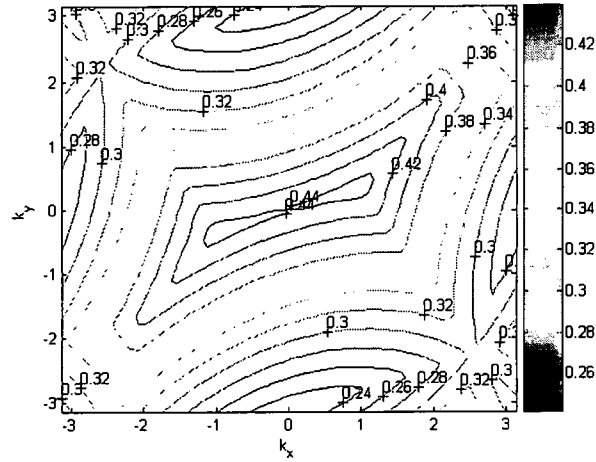
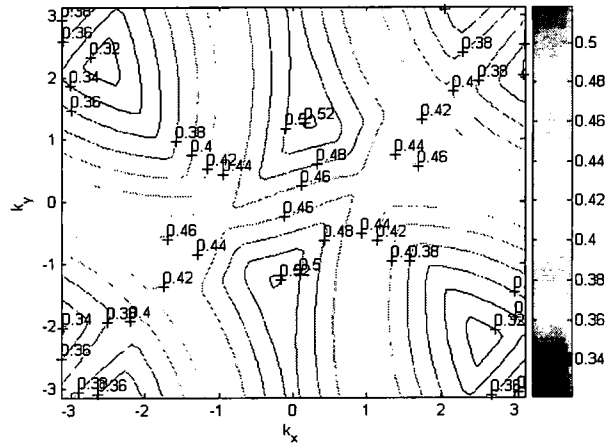


Figure 6.5: EFS for the second and third band with rotation angles of 0° (a-b), 10° (c-d). Index parameters are $r=0.1a$, $n_{1b}=2.55$, $n_{2b}=1.78$, $n_{1c}=1.64$, $n_{2c}=1.62$.

Now we oriented the crystal axes from 0^0 to 45^0 and by analysis all the curves we found that the rotation the axes by 30^0 gives wider and flatter surface for the 2nd band without overlapping the 3rd band . Now in figure 6.6a and 6.6b depict the 2nd and 3rd band after the rotation of the principal axis with respect to the dielectric axis by 30^0 .



(a)



(b)

Figure 6.6 : EFS for the second and third band with rotation angles of 30^0 (a-b). Index parameters are $r=0.1a$, $n_{1b}=2.55$, $n_{2b}=1.78$, $n_{1c}=1.64$, $n_{2c}=1.62$.

6.5 : Radius dependency

We study the effect of the size of the cylinder radius on self-collimated beam. The radius of each hole was changed from $r = 0.1a$ to $0.4a$ and the normalized frequency, a/λ we used for this case are 0.34 and the rotation angle α is 30° and the incident wave make 15° with the input surface. We compare the intensity of the exit surface of the crystal. The results for the 4 types of radius are shown in figure 4. As can be seen from the figure, the power flow is not affected by the variation of the cylinder radii. In DAST crystal, we found that intensity of the beam is not affected much by changing the cylindrical radius.

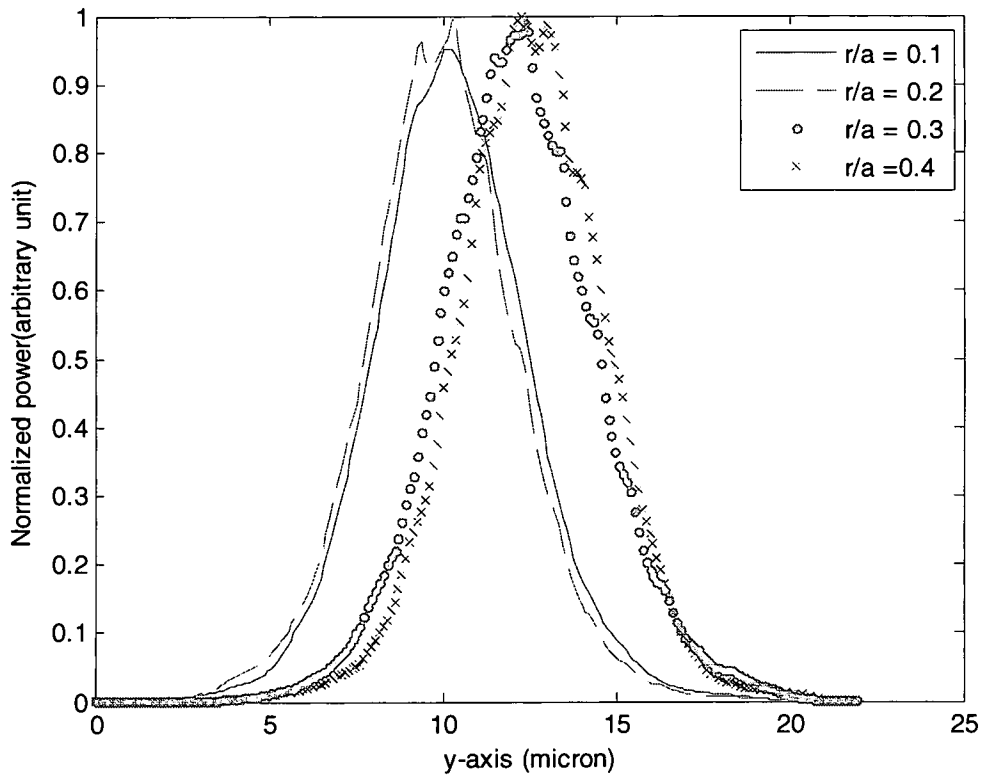


Figure 6.7: Intensity profile with different radii. Solid blue, dashed red, dotted green and crossed magenta represents the intensity profile for radius, $r = 0.1a$, $0.2a$, $0.3a$ and $0.4a$ respectively. Index parameters are $n_{1b}=2.55$, $n_{2b}=1.78$, $n_{1c}=1.64$, $n_{2c}=1.62$.

Now the broadening or change in the beam profile are 25.39 % , 12.07% , 12.55% and 11.56 % for the radius of r/a 0.1 , 0.2, 0.3 and 0.4 respectively . Therefore we can say that the beam propagate inside the crystal without any significant broadening for the larger holes . We find a significant change of the angle deviation from the normal incidence respect to radius. Figure 6.8 resent the result of the deviation angle with respect to incidence angle of different radius. The direction of the self-collimated beam remains almost constant for the radius of $r/a = 0.4$ where the deviation is nearly constant around 4° .

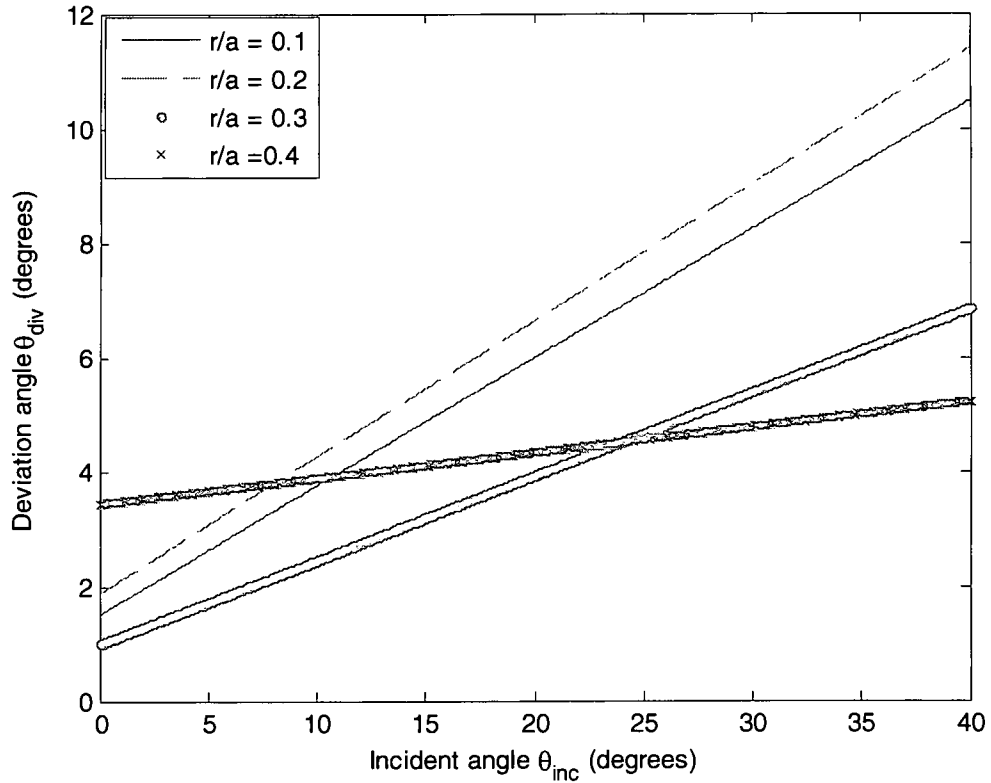


Figure 6.8: Deviation angles versus input angle for several radii. Rotation angle is 30° degrees. Solid blue, dashed red, dotted green(thicker) and crossed magenta(thickest) line represents the deviation for radius, $r = 0.1a, 0.2a, 0.3a$ and $0.4a$ respectively. Index parameters are $n_{1b}=2.55, n_{2b}=1.78, n_{1c}=1.64, n_{2c}=1.62$.

6.6: Effect of anisotropy

Anisotropy of the materials effect the beam propagation inside the crystals. We choose the $r/a = 0.3$ and vary the anisotropy from 1.43 to 1.1591 of the background y-axis. We maintain the rotation of the crystal 30° degrees. In figure 6.9 , we present the intensity profile of the beam in the exit surface. From the figure it is clear that beam intensity down significantly for the lower anisotropy.

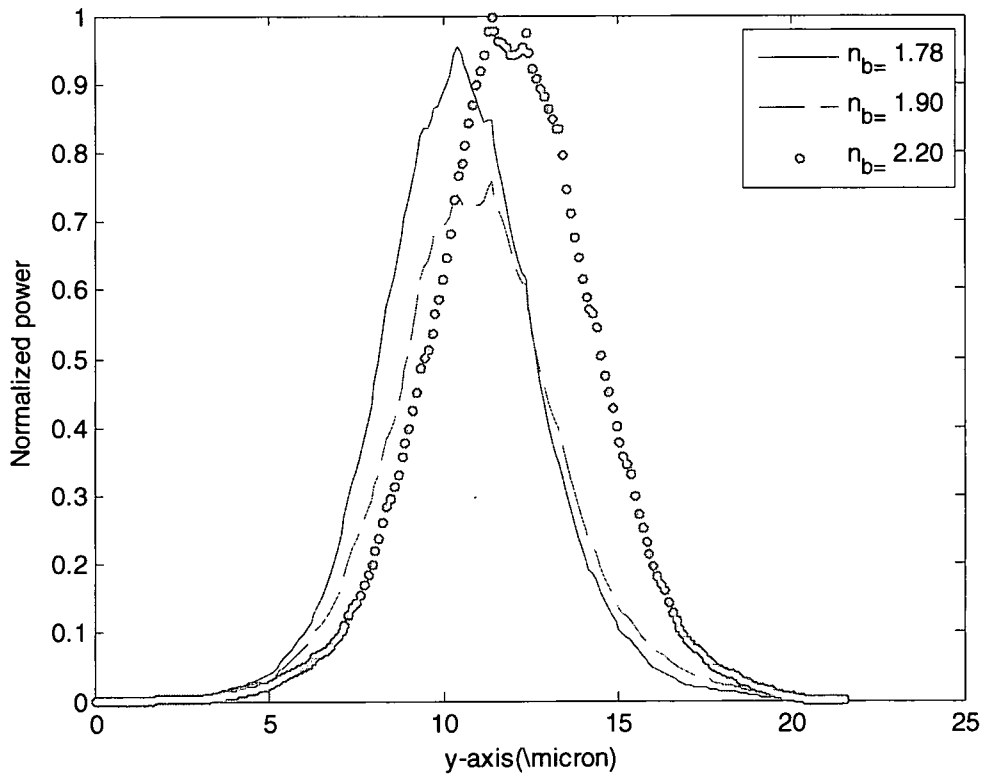


Figure 6.9: Output beam shape for three anisotropy parameters. Solid blue, dashed red, and dotted green represents the intensity profile for n_{2b} 1.78, 1.90 and 2.20 respectively. Index parameters are $r=0.1a$, $n_{1b}=2.55$, $n_{2b}=1.78$, $n_{1c}=1.64$, $n_{2c}=1.62$.

Now the deviation of the group velocity from the normal incidence also affected by the anisotropy variation. In figure 6.10 we present the result of divergence angle with

respect to the incidence angle. Higher anisotropy make the beam more collimated compare to the less anisotropy.

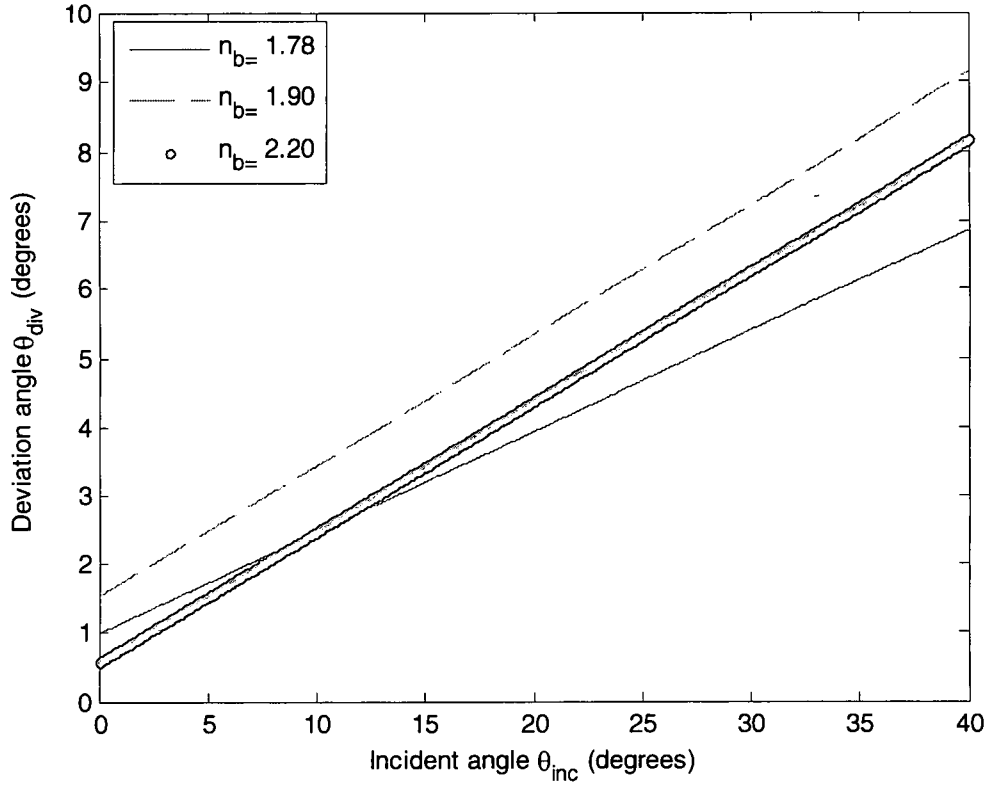


Figure 6.10: Deviation angles versus input angle for three anisotropy parameters. Rotation angle is 30 degrees. Solid blue, dotted red(thickest line) and the dashed green represents the deviation for n_{2b} of 1.78, 1.90 and 2.20 respectively. Index parameters are $r=0.1a$, $n_{1b}=2.55$, $n_{2b}=1.78$, $n_{1c}=1.64$, $n_{2c}=1.62$.

6.7: FEM Simulation Result

Now from the above analysis to get the best self-collimated beam, we choose the radii, $r/a=0.4$ and the anisotropy ratio 1.78/2.55. The EFS for the 2nd band contour we are using is depicted in figure 6.11. We excited the normalized frequency of 0.34. By

theoretically we predict that the incident beam of as large as 40° will be collimated inside the crystal with nearly constant deviation angle of 4° .

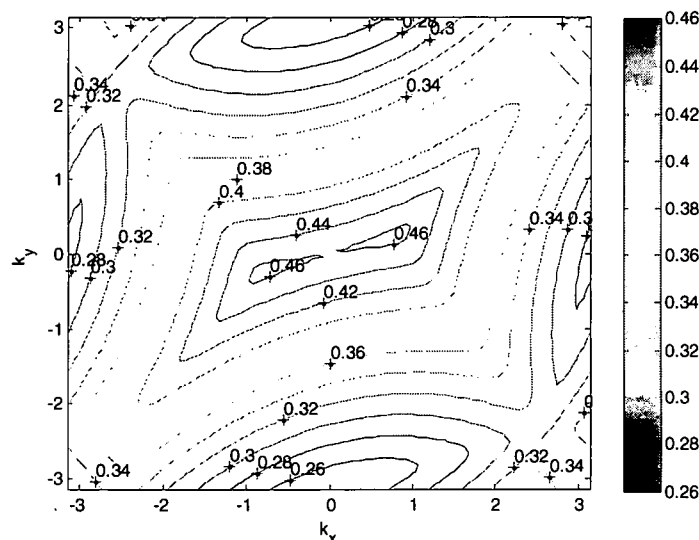
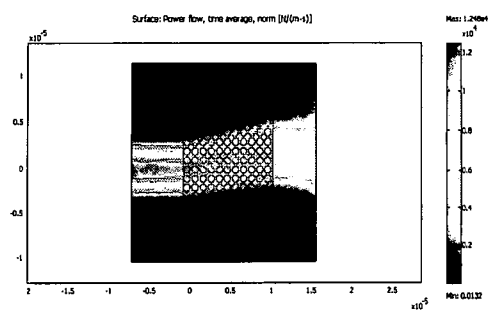
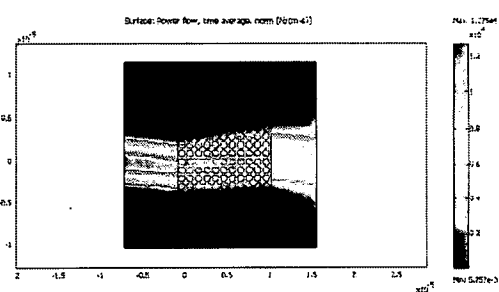


Figure 6.11: EFS for the second band with rotation angles of 30° . Index parameters are $r=0.4a$, $n_{1b}=2.55$, $n_{2b}=1.78$, $n_{1c}=1.64$, $n_{2c}=1.62$.

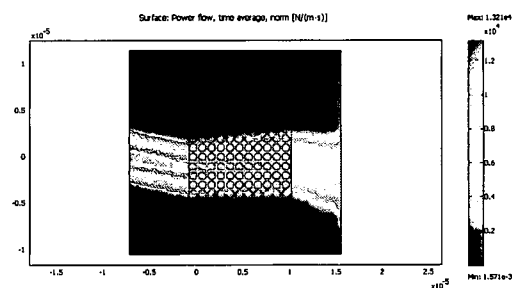
In figure 6.12(a-i), we present the power flow of the TM wave in this structure by finite element (FE) method. An incident Gaussian beam of width $3a$ propagates through the DAST crystal for the normalized frequency of 0.34. Figure 6.12a shows that the incident beam is 0° . In this case collimated beam is not go through without deviation from normal. This divergence comes as the beam hit upper corner of the curve of the contour of normalized frequency 0.34 and divergence angle is 6° . But incident angle from 5° to 40° , the beam is perfectly collimated and remain under the tolerance range of 3° .



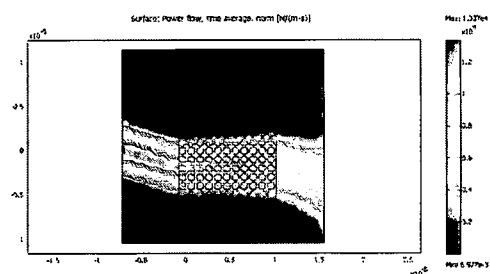
(a)



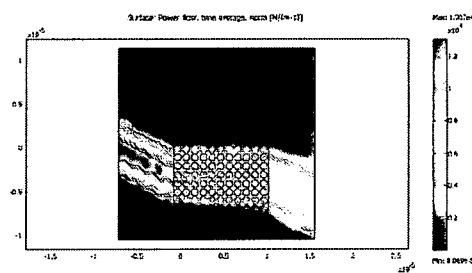
(b)



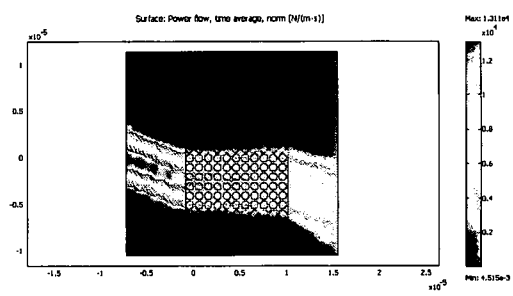
(c)



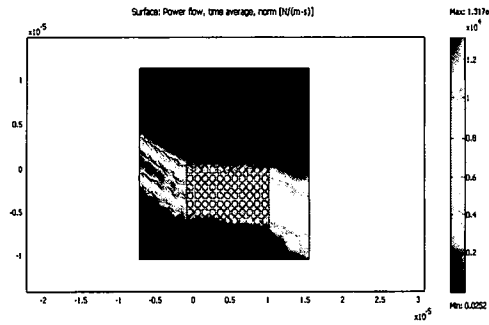
(d)



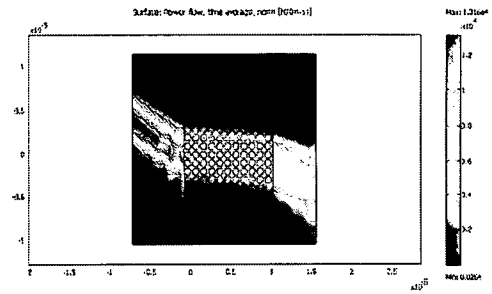
(e)



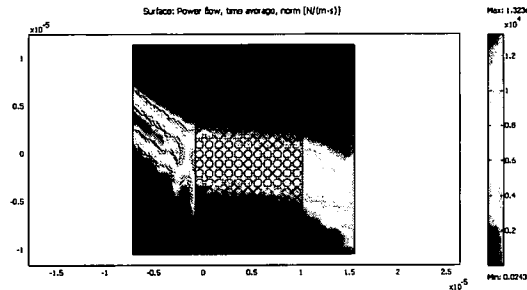
(f)



(g)



(h)



(i)

Figure 6.12: Power flow inside the crystal of normalized frequency , $a/\lambda = 0.4$ for incident angle a) 0° , b) 5° , c) 10° , d) 15° , e) 20° , f) 25° , g) 30° , h) 35° and i) 40° . Rotation angle 30° degrees. Index parameters are $r=0.4a$, $n_{1b}=2.55$, $n_{2b}=1.78$, $n_{1c}=1.64$, $n_{2c}=1.62$.

However when the incident angle is 40° it couples only 65% of the input power whereas for the incident angle of 35° it couples about 76% . Figure 6.13 represents the intensity of the beam before enter the crystal (violet solid line) , entrance surface (red for the incident 35° and green solid line for the incident angle of 40°) and the exit surface (red dashed line for the incident angle 35° and green dashed line for the incident angle of 40°)

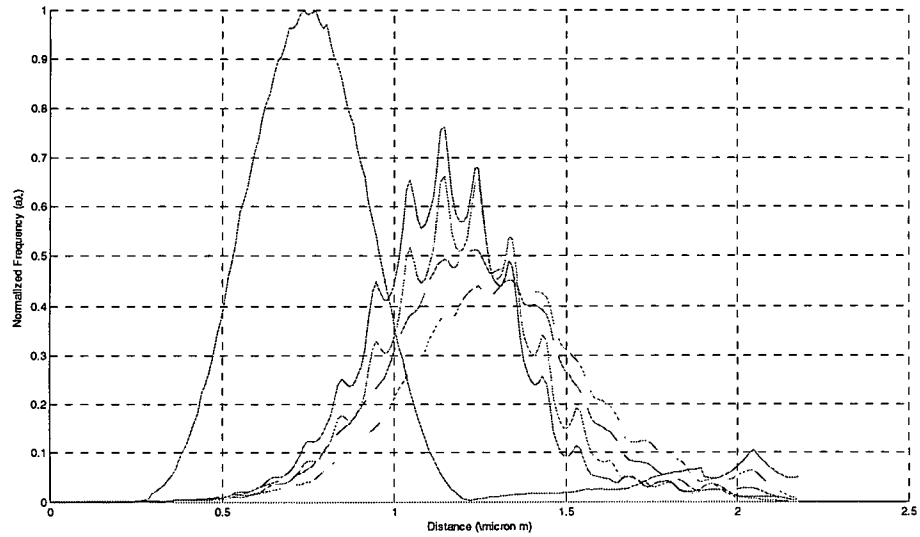


Figure 6.13 : Normalized power in different region of the square PhC of anisotropic constituents from air with the incident angle, θ_{in} , of 35° and 40° . Solid violet curve represents the input intensity. Solid red and green curve represents the intensity profile for $\theta_{in} = 35^\circ$ and 40° respectively. Dashed red and green curve represents the intensity profile for $\theta_{in} = 35^\circ$ and 40° respectively in the exit surface of the crystal. The index parameters are $n_1 = 2.55$, $n_2 = 1.78$, $\alpha = 30^\circ$ and $r = 0.4a$.

Also for the 40° incidence the output beam quality is very poor and beam is broadened inside the crystal and power loss for this case is about 55%. So now we get the conclusion that by rotation of the crystal, we can have a good self collimated beam as large as 35° with minimum divergence of 3° . This is a significant improvement compared to the case without rotation of the crystal where the maximum incident angle that would produce well collimated beam inside the crystal.

CHAPTER VII

CONCLUSION AND FUTURE DIRECTION

Increasing the range of the incident angles for self-collimation inside a 2D Photonic crystal is main topic of this dissertation. We engineered the dispersion surfaces of 2D photonic crystal to improve the incident angle by introducing of two concepts : total anisotropic photonic crystal and rotation of the principal axes of the anisotropic media relative to the symmetry axes of the photonic crystal.

First we study the self-collimated beam inside the isotropic 2D square and triangular photonic crystal. We investigate the EFS of these two types of lattice by changing the dielectric index ratio of cylinder and background and also by varying the radius of the cylinder . We found that both cases the maximum incident angle that can be coupled and collimated inside the PhC are almost same. For the square and triangular PhC consisting of isotropic materials the maximum incident angle we could use is 14° based on the DAST index parameters. We confirmed our theoretical result by using FEM simulation results. Both results are in good agreement. So we can summarize our finding that though the shape of the EFS for the PhC of square lattice and triangular lattice are different neither of them greatly increase the range of collimated incident angles for isotropic low-index contrast materials.

Next we reported the dispersion surfaces of the square PhC with anisotropic constituents. We used cylindrical rods on a square lattice embedded in a host medium, both of which could be anisotropic. The index parameters we used for our calculations are within the ranges that have already been achieved for DAST in the laboratory. We found that for relatively modest refractive index changes, the dispersion surfaces of anisotropic photonic crystals may be greatly distorted from those of a homogeneous medium. We demonstrated how the use of anisotropy for the constituents can be applied to increase the range of input angles that are self-collimated. The self-collimation is effective for two PhC geometries. In both cases the E-field parallel to the n_1 principal axis, while for the isotropic case the rods are aligned with the n_1 principal axis and for the anisotropic case the rods parallel to the n_2 principal axis. We found that the maximum input angle that will be collimated is around 22° . In conclusion, by introducing the anisotropy in the photonic crystal increase the incident angle about 57% that will be self-collimated compare to the isotropic case.

We then engineered the dispersion surfaces of the complete anisotropic PhC by rotation of the principle axes of the anisotropic media relative to the symmetry axes of the photonic crystals. We found that the rotation make the dispersion surface wider and flatter. That means more angular working space so wide range of incident angles can be coupled to the EFS and be self-collimated to a high degree inside the PhC. We found by numerical calculations of the EFS and by FEM simulations that the maximum input angle that will be self-collimated is increased to 35° . This value is a key achievement as it is increase the incident angles about 150% compare to the low-index contrast, isotropic constituent case.

Future Research Direction

Organic salt, DAST crystals often exhibit better nonlinear optical (NLO) properties, such as larger nonlinearity and wider frequency response, than those of inorganic NLO crystals [81]. DAST crystals possess significant NLO properties ($d_{11} = 1010 \pm 110$ pm/V at $\lambda = 1318$ nm) [82] and an electrooptic (EO) coefficient ($r_{11} = 92 \pm 9$ pm/V at $\lambda = 720$ nm). [83] This strong second-order nonlinearity and electrooptic coefficient of the DAST crystal can be further used to generate a strong THz signal by mixing two waves inside the sample. By managing the dispersion inside the crystal two beams incident at different angles can be collimated inside the PhC to assure a small walkoff of the beams. The generation of coherent and widely tunable terahertz- (THz-) wave radiation is of interest for a variety of applications in basic and applied physics, communication, and life sciences.

REFERENCES

1. E. Yablonovitch, "Inhibited spontaneous emission in solid-state physics and electronics," Phys. Rev. Lett. 58, 2059 (1987).
2. S. John, "Strong localization of photons in certain disordered dielectric superlattices," Phys. Rev. Lett. 58, 2486 (1987).
3. E. Yablonovitch, M. Gitter, K. M. Leung, Phys Rev Lett 67 (17), 2295(1991).
4. TF Krauss, RM DeLaRue, S. Brand "Two-dimensional photonic-bandgap structures operating at near infrared wavelengths," NATURE 383, 699 (1996).
5. J. D. Joannopoulos, P. Villeneuve, and S. Fan, Nature (London) 386, 143 (1997).
6. T. I. Weng and G. Y. Guo, "Band structure of honeycomb photonic crystal slabs," J. Appl. Phys. 99, 093102 (2006).
7. D. D. Wang, Y.S. Wang, L.E. Deng, C.X. Zhang, X. Han, "Larger complete photonic bandgaps in two-dimensional photonic crystal heterostructure," Solid State Communications 137, 74 (2006).
8. V. A. Tolmachev, "Tuning of the Photonic Band Gaps and the Reflection Spectra of a One-Dimensional Photonic Crystal Based on Silicon and a Liquid Crystal," Optics and Spectroscopy 99(5), 765 (2005).
9. Zhi-Yuan Li and Younan Xia, "Omnidirectional absolute band gaps in two-dimensional photonic crystals", Phys. Rev. B 64, 153108 (2001).

10. A Sharkawy, S. Shi and D. W. Prather, "Multichannel wavelength division multiplexing using photonic crystals," *Appl. Opt.* 40, 2247 (2001).
11. S. Fan, P. R. Villeneuve and J. D. Joannopoulos, "Microcavities in photonic crystals: mode symmetry, tunability, and coupling efficiency," *Phys. Rev. B* 54, 7837 (1996).
12. H. A. Haus, S. Fan, P. R. Villeneuve and J. D. Joannopoulos J D, "Channel drop filters in photonic crystals," *Opt. Express* 3, 4 (1998).
13. P. Tran, "Optical switching with nonlinear photonic crystal: a numerical study", *Opt. Lett.* 21, 1138–40, (1996).
14. A. Mekis, J. C. Chen, I. Kurland, S. Fan, Villeneuve P R and Joannopoulos J D, "High Transmission through sharp bends in photonic crystal waveguides," *Phys. Rev. Lett.* 77, 3787 (1996).
15. D. M. Mustai, A Sharkawy, S. Y. Shi, G. Jin , J. Murakowski and D. W. Prather D W, "Characterization and analysis of photonic crystal coupled waveguides," *J. Microlithogr. Microfabr. Microsyst.* 2 , 292 (2003).
16. D. W. Prather, S. Shi, J. Murakowski, G. J. Schneider, A. Sharkawy, C. Chen, B. Lin Miao and R. Martin, "Self-collimation in photonic crystal structures: a new paradigm for applications and device development," *J. Phys. D: Appl. Phys.* 40, 2635 (2007).
17. H. Kosaka, T. Kawashima, A. Tomita ,M Notomi, T. Tamamura, T. Sato and S. Kawakami, "Superprism phenomena in photonic crystals," *Phys. Rev. B* 58 10096, (1998).

18. H. Kosaka, T. Kawashima, A. Tomita, M. Notomi, T. Tamamura, T. Sato and S. Kawakami, "Self-collimating phenomena in photonic crystals," *Appl. Phys. Lett.* 74, 1212 (1999).
19. D. W. Prather, S. Shi, J. Murakowski, G. J. Schneider, A. Sharkawy, C. Chen and B. L. Miao, "Photonic crystal structures and applications: perspective, overview and development," *IEEE J. Sel. Topics. Quantum Elec.* 12, 1416 (2006).
20. J. Witzens, M. Loncar and A. Scherer, "Self-collimation in planar photonic crystals," *IEEE J. Sel. Top. Quantum Electron* 8, 1246 (2002).
21. L. Wu, M. Mazilu and T. F. Krauss, "Beam steering in planar-photonic crystals: from superprism to supercollimator," *J. Lightwave Technol.* 21, 561 (2003).
22. P. T Rakich, M. S. Dahlem, S. Tandon, M. Ibanescu, M. Soljacic, G. S. Petrich, J. D. Joannopoulos, L. A. Kolodziejski and E. P. Ippen, "Achieving centimetre-scale supercollimation in a large-area two-dimensional photonic crystal," *Nature Mater.* 5, 93 (2006).
23. M. Augustin, R. Iliew, C. Etrich, D. Schelle, H. J. Fuchs, U. Peschel, S. Nolte, E. B. Kley, F. Lederer and A. Tunnermann, "Self-guiding of infrared and visible light in photonic crystal slabs," *Appl. Phys. B* 81, 313 (2005).
24. T. Yamashita and C. J. Summers, "Evaluation of self-collimated beams in photonic crystals for optical interconnect," *IEEE J. Sel. Areas Commun.* 23, 1341 (2005).
25. D. N. Chigrin, S. Enoch, S. C. Torres and G. Tayeb, "Self-guiding in two-dimensional photonic crystals," *Opt. Express* 11, 1203 (2003).
26. I. H. H. Zabel and D. Stroud, *Phys. Rev. B* **48**, 5004 (1993).

27. J. D. Joannopoulos, R. D. Meade, and J. N. Winn, Photonic Crystals, Molding the Flow of Light, Princeton, New Jersey: Princeton University Press (1995).
28. K. Sakoda. Optical Properties of Photonic Crystals. 2nd edition, Springer-Verlag, New York, (2005).
29. E. Yablonovitch, "Photonic band-gap structures," J. Opt. Soc. Am. B 10, 283–295 (1993).
30. C. Kittel, Introduction to Solid State Physics, John Wiley & Sons, Inc. (1996).
31. Z. M. Zhang and K. Park, "On the Group Front and Group Velocity in a Dispersive Medium Upon Refraction From a Nondispersive Medium", J. Heat Transfer 126, 244 (2004).
32. A. Bers. Note on group velocity and energy propagation. Am. J. Phys. 68, 482 (2000).
33. Dogariu, A. Kuzmich, and L. J. Wang. "Transparent anomalous dispersion and superluminal-light-pulse propagation at a negative group velocity", Phys. Rev. A 63, 053806 (2001).
34. L. J. Wang, A. Kuzmich, and A. Dogariu, "Gain-assisted superluminal light propagation", Nature 406, 277 (2000).
35. A. Moroz. <http://www.wave-scattering.com/negative.html>.
36. H. Lamb. On group-velocity. Proc. London Math. Soc. 1, 473 (1904).
37. L. Brillouin, Wave propagation and group velocity, Academic press, New York, (1960).
38. A. Yariv, and P. Yeh, Optical Waves in Crystals, John Wiley & Sons, Inc. (1984).

39. W. Jiang and R. T. Chen, "Multichannel Optical Add-Drop Processes in Symmetrical Waveguide-Resonator Systems," *Physical Review Letters* 91, 213901 (2003).
40. Y. Jiang, W. Jiang, L. Gu, X. Chen, R. T. Chen, "80-micron interaction length silicon photonic crystal waveguide modulator," *Appl. Phys. Lett.* 87, 221105 (2005).
41. M. Imada, S. Noda, A. Chutinan, T. Tokuda, M. Murata and G. Sasaki, "Coherent two-dimensional lasing action in surface-emitting laser with triangular-lattice photonic crystal structure," *Appl. Phys. Lett.* 75, 316- 318 (1999).
42. T. Baba, K. Inoshita, H. Tanaka, J. Yonekura, M. Ariga, A. Matsutani, T. Miyamoto, F. Koyama, and K. Iga, "Strong Enhancement of Light Extraction Efficiency in GaInAsP 2-D-Arranged Microcolumns," *J. Lightwave Technol.* 17, 2113 (1999).
43. W. Jiang, R. T. Chen, and X. Lu, "Theory of light refraction at the surface of a photonic crystal," *Physical Review B* 71, 245115 (2005).
44. L. Wu, M. Mazilu, and T. F. Krauss, "Beam Steering in Planar-Photonic Crystals: From Superprism to Supercollimator," *J. Lightwave Technol.* 21, 561 (2003).
45. P. St. J. Russel, "Interference of integrated Floquet-Bloch waves," *Phys. Rev. A* 33, 3232, (1986).
46. B. Gralak, S. Enoch, and G. Tayeb, "Anomalous refractive properties of photonic crystals," *J. Opt. Soc. Am. A* 17, 1012 (2000).
47. T. Baba, M. Nakamura, "Photonic crystal light deflection devices using the

- superprism effect," IEEE J. Quantum Electron. 38, 909 (2002).
48. H. Kosaka, A. Tomita, T. Kawashima, T. Sato, S. Kawakami, "Splitting of triply degenerate refractive indices by photonic crystals," Phys. Rev. B, 62, 1477 (2000).
 49. K. M. Leung, Y.F. Liu, "Full vector wave calculation of photonic band structures in face-centered-cubic dielectric media," Phys. Rev. Lett. 65, 2646 (1990).
 50. Z. Zhang, S. Satpathy, "Electromagnetic wave propagation in periodic structures: Bloch wave solution of Maxwell's equations," Phys. Rev. Lett. vol. 65, 2650 (1990).
 51. K. Yee, "Numerical solutions of initial boundary value problems involving Maxwell's equations in isotropic media," IEEE Transactions on Antennas and Propagation AP-14, 302 (1966).
 52. C. T. Chan, Q. L. Yu, and K. M. Ho., "Order- N spectral method for electromagnetic waves," Phys. Rev. B 51, 16 635 (1995).
 53. J. Arriaga, A. J. Ward, and J. B. Pendry, "Order- N photonic band structures for metals and other dispersive materials," Phys. Rev. B 59, 1874 (1999).
 54. A. Taflove and S.C. Hagness, Computational Electrodynamics-The Finite-Difference Time Domain Method, 3rd Edition, Artech House, Boston, (2005).
 55. A. Taflove and M. E. Brodwin "Numerical solution of steady-state electromagnetic scattering problems using the time-dependent Maxwell's equations". Microwave Theory and Techniques, IEEE Transactions 23, 623 (1975).
 56. J. Jin, The Finite Element Method in Electromagnetics, 2nd Edition, Wiley, New York, (2002).

57. K. Busch, G. von Freymann, S. Linden, S.F. Mingaleev, L. Tkeshelashvili, M. Wegener, "Periodic nanostructures for photonics", *Physics Reports* 444, 101 (2007).
58. J. P. Dowling and C. M. Bowden, "Anomalous index of refraction in photonic bandgap materials," *J. Mod. Opt.* 41 345(1994).
59. S. Y. Lin, V. M. Hietala, L. Wang and E. D. Jones, "Highly dispersive photonic band-gap prism," *Opt. Lett.* 21, 1771 (1996).
60. K. T. Ohtaka, Ueta and Y. Tanabe, "Analogy of optics of photonic crystals to that of anisotropic crystals," *J. Phys. Soc. Jpn.* 65, 3068 (1996) .
61. M. Notomi, "Negative refraction in photonic crystal," *optical and Quantum Electronics* vol. 34, 133(2002).
62. M. Notomi. "Theory of light propagation in strongly modulated photonic crystals: Refraction like behavior in the vicinity of the photonic band gap," *Phys. Rev. B* 62, 10696 (2000).
63. H. Kosaka, T. Kawashima, A. Tomita, M. Notomi, T. Tamamura, T. Sato, and S. Kawakami, "Photonic crystals for micro lightwave circuits using wavelength-dependent angular beam steering," *Appl. Phys. Lett.* 74, 1370 (1999).
64. S. Foteinopoulou and C. M. Soukoulis, "EM wave propagation in two-dimensional photonic crystals: a study of anomalous refractive effects," *Cond.mat/0403542* (2004).
65. I.V. Lindell, S. A. Tretyakov, K. I. Nikoskinen, and S. Ilvonen, " BW media with negative parameters, capable of supporting backward waves. *Micro. Opt. Tech. Lett.* 31, 129(2001).

66. S. Foteinopoulou, E. N. Economou, and C. M. Soukoulis, "Refraction in Media with a Negative Refractive Index," *Phys. Rev. Lett.* 90, 107402(2003).
67. X. Zhang, "Image resolution depending on slab thickness and object distance in a two dimensional photonic-crystal-based superlens," *Phys. Rev. B* 70, 195110 (2004).
68. C. Luo, S. G. Johnson, J. D. Joannopoulos, and J. B. Pendry, "All-angle negative refraction without negative effective index," *Phys. Rev. B* 65, 201104 (2002).
69. P. S. J. Russell, "Optics of Floquet-Bloch waves in dielectric gratings," *Appl. Phys. B* 39, 231(1986).
70. R. Zengerle, "Light Propagation in Singly and Doubly Periodic Planar Waveguides," *J. of Mod. Opt.* vol. 34, 1987 (1987).
71. Z. Ruan, M. Qiu, S. Xiao, S. He, and L. Thylen, "Coupling between plane waves and Bloch waves in photonic crystals with negative refraction," *Phys. Rev. B* 71, 045111 (2005).
72. K. Sakoda. *Optical Properties of Photonic Crystals*. 2nd Edition, Springer-Verlag, New York, (2005).
73. S. Noda and T. Baba, "Roadmap to Photonic Crystals,eds. (Kluwer, Boston, 2003).
74. Z.-Y. Li, B.-Y. Gu, and G.-Z. Yang, *Phys. Rev. Lett.* 81, 2574 (1998).
75. Z.-Y. Li, J. Wang, and B.-Y. Gu, *Phys. Rev. Lett.* 81, 2574 (1998).
76. G. Alagappan, X. W. Sun, P. Shum, and M. B. Yu, *J. Opt. Soc. Am. B* 23, 1478 (2006).
77. Bin Cai, Toshiaki Hattori, Hui Hua Dong, Kyoji Komatsu, Crsipin Zawadzki, Norbert Keil and Toshikuni Kaino, " Refractive index control and grating

- fabrication of 4-N,N –dimethylamion-N-methyl-4 stilbazolium Tosylate Crstal,”
Jpn. J. Appl. Phys. 40, L964(2001).
78. A. Schneider, M. Neis, M. Stillhart, B. Ruiz, R. U. A. Khan, and P. Günter,
"Generation of terahertz pulses through optical rectification in organic DAST
crystals: theory and experiment," J. Opt. Soc. Am. B **23**, 1822(2006).
 79. C. Bosshard, R. Spreiter, and P. Günter, "Microscopic nonlinearities of two-
component organic crystals," J. Opt. Soc. Am. B **18**, 1620 (2001).
 80. K. Kawase, M. Mizumo, S. Sohma, H. Takahashi, T. Taniuchi, Y. Urata, S.
Wada, and H. Tashiro, "Difference-frequency terahertz-wave generation from 4-
dimethylamino-N-methyl-4- stilbazolium-tosylate by use of an electronically
tuned Ti:sapphire laser ,” Opt. Lett. **24**, 1065 (1999).
 81. H. Adachi, T. Taniuchi, M. Youshimura, S. Brahadeeswaran, T. Higo, M. Takagi,
Y. Mori, T. Sasaki and H. Nakanishi, “ High-quality organic 4-Dimethylamino-N-
methyl-4-stilbazolium Tosylate (DAST) crystals for THz wave generation,” Jap. J.
Appl. Phys. **43**, L 1121(2004).
 82. U. Meier, M. Bosch, Ch. Bosshard, F. Pan and P. Günter, “Parametric interactions
in the organic salt 4-N,N-dimethylamino-4'-N'- methyl-stilbazolium tosylate at
telecommunication wavelengths,” J. Appl. Phys. Vol. **83** 3486(1998).
 83. F. Pan, G. Knoöpfe, Ch. Bosshard, S. Follonier, R. Spreiter, M. S. Wong and P.
Günter, “Electro-optic properties of the organic salt 4-N,N-dimethylamino-4'-N'-
methyl- stilbazolium tosylate,” Appl. Phys. Lett. Vol. **69** 13(1996).

APPENDIX

Matlab Programs

Program 1 : Band Structure Calculation for 2D Isotropic Square Lattice (PWEM)

```
N1 = 100; % Number of Plane Wave
pi = acos(-1.0);
d=1.;
a=.3; % Cylinder Radius
bbeta = 3.14159*a*a/d/d*2.0/sqrt(3.0);
EPSA=1.64^2.; % ROD DIELECTRIC
EPSB=2.55^2.; % MATRIX DIELECTRIC

% The major symmetry points in the Brillouin zone are defined
gxg = 0.0; gyg = 0.0;
gxx = 0.0; gyx = 2.0*pi/sqrt(3.0);
gxj = 2.0*pi/3.0; gyj = 2.0*pi/sqrt(3.0);

% The itinerary around the brillouin zone is laid out.
gxi(1) = gxg; gyi(1) = gyg;
gxi(2) = gxx;
gyi(2) = gyx;
gxi(3) = gxj;
gyi(3) = gyj;
gxi(4) = gxg;
gyi(4) = gyg;

% Construct the wave vectors used in the plane wave calculation    L=0;
gx1 = 2.0*pi;
gy1 = -2.0*pi/sqrt(3.0);
gx2 = 0.0;
gy2 = 2.0*pi*2.0/sqrt(3.0);

%Generate all the wavevectors within a hexagon of diameter 2*n1.
for ii=-N1:N1;
```

```

for j=-N1:N1;
    if ( -(N1+1)<(ii+j)) & ((ii+j)<(N1+1))),
        L=L+1;
        gx(L) = gx1*ii + gx2*j;
        gy(L) = gy1*ii + gy2*j;
    end;
end;
end;
L

% Construct the dielectric matrix

vcel = sqrt(3.0)/2.d0*d*d;
for ii = 1:L;
    EPS(ii,ii) = bbeta/EPsA + (1.D0-bbeta)/EPsB;
end;
for ii=1:L;
    i1 = ii + 1;
    for j=i1:L;
        x1 = gx(ii) - gx(j);
        x2 = gy(ii) - gy(j);
        x = sqrt(x1*x1+x2*x2)*a/d;
        EPS(ii,j) = 2.d0*pi*(1/EPsA-1/EPsB)*a*a/(vcel) * besselj(1,x)/x;
    end;
end;

% The matrix is symmetric
    EPS(j,ii) = EPS(ii,j);
end;
end

% Use the itinerary constructed above to move around the Brillouin zone
n=L;
% Counter for the number of points in the itinerary
nknt = 1;
for nk = 1:3;
    nk1 = nk+1
    nmax= 20;
    for l=1:nmax;
        dkx =(l-1)*(gxi(nk1)-gxi(nk))/(nmax) + gxi(nk);
        dky =(l-1)*(gyi(nk1)-gyi(nk))/(nmax) + gyi(nk);
        for ii=1:n;
            a(ii,ii) = EPS(ii,ii)*((dkx+gx(ii))^2 + (dky+gy(ii))^2)/4.d0/pi/pi;

```

```

        for j=ii+1:n;
            a(ii,j) = EPS(ii,j)*((dkx+gx(ii))*(dkx+gx(j)) + (dky+gy(ii))*(dky+gy(j)))/4.d0/pi/pi;
            a(j,ii) = a(ii,j);
        end
    end

% Find the eigenvalues
v=eig(a);
% Store the lowest 10 eigenvalues for plotting
for li=1:10;
    rr(nknt,li)=sqrt(v(li));
    kxx(nknt)=nknt-1;
end

    nknt = nknt + 1;
end
end

% Plot lowest six eigenvalues
figure(1)
hold on;
plot(kxx,rr(:,1),'r');
plot(kxx,rr(:,2),'r');
plot(kxx,rr(:,3),'r');
plot(kxx,rr(:,4),'r');
plot(kxx,rr(:,5),'r');
plot(kxx,rr(:,6),'r');
hold off;

```

Program 2 :

Eqfrequency Surfaces Calculation for 2D Anisotropic Square Lattice for H Pol. (PWEM)

```

close all
%PBG plane wave 2D anisotropic H
N1 = 30;
pi = acos(-1.0);
d=0.;
a=0.3;
d1=1;
d2=1;
bbeta = pi*a*a/d1/d2;
EPSAx=2.55^2; % ROD DIELECTRIC x

```

```

EPSBx=1.64^2;% MATRIX DIELECTRIC x
EPSAy=1.78^2; % ROD DIELECTRIC y
EPSBy=1.62^2;% MATRIX DIELECTRIC y
etax=(1 /EPSAx-1 /EPSBx);
etay=(1 /EPSAy-1 /EPSBy);

% The major symmetry points in the Brillouin zone are defined
gxg = 0.0; gyg = 0.0;
gxx = 0.0; gyx = pi/d2;
gxm = pi/d1; gym = pi/d2;
% The itinerary around the Brillouin zone is laid out.
gxi(1) = gxx; gyi(1) = gyx;
gxi(2) = gxg;
gyi(2) = gyg;
gxi(3) = gxm;
gyi(3) = gym;
gxi(4) = gxx;
gyi(4) = gyx;

% Construct the wave vectors used in the plane wave calculation

L=0;
gx1 = 2.0*pi/d1;
gy1 = 0;
gx2 = 0.0;
gy2 = 2.0*pi/d2;
% Generate all the wavevectors within a hexagon of diameter 2*n1.

for ii=-N1:N1;
    for j=-N1:N1;
        if ( -(N1+1)<(ii+j) & ((ii+j)<(N1+1))),
            L=L+1;
            gx(L) = gx1*ii + gx2*j;
            gy(L) = gy1*ii + gy2*j;
        end;
    end;
end;
L

% Construct the dielectric matrix

```

```

    vcel = d1*d2;
    for ii = 1:L;
        EPSx(ii,ii) = bbeta*1/EPsAx + (1.D0-bbeta)/EPsBx;
        EPSy(ii,ii) = bbeta*1/EPsAy + (1.D0-bbeta)/EPsBy;
    end;

    for ii=1:L;
        i1 = ii + 1;
        for j=i1:L;
            x1 = gx(ii) - gx(j);
            x2 = gy(ii) - gy(j);
            x = sqrt(x1*x1+x2*x2)*a;
            EPSx(ii,j) = 2.d0*etax*pi*a*a/(vcel) * besselj(1,x)/x;
            EPSy(ii,j) = 2.d0*etay*pi*a*a/(vcel) * besselj(1,x)/x;
% The matrix is symmetric
            EPSx(j,ii) = EPSx(ii,j);
            EPSy(j,ii) = EPSy(ii,j);
        end;
    end
end

% Use the itinerary constructed above to move around the Brillouin zone
n=L;
% Counter for the number of points in the itinerary
nmax=40;
for nk = 1:nmax; % x direction in the BZ
    for nl=1:nmax; % y direction in the BZ
        dkx(nk) = 2*(nk-1)*pi/(nmax-1)/d1-pi/d1;
        dky(nl) = 2*(nl-1)*pi/(nmax-1)/d2-pi/d2;
        for ii=1:n;
            a(ii,ii) = (EPSx(ii,ii)*(dkx(nk)+gx(ii))^2 + EPSy(ii,ii)*(dky(nl)+gy(ii))^2)/4.d0/pi/pi;
%            b(ii,ii)=EPS(ii,ii);
            for j=ii+1:n;
                a(ii,j) = (EPSx(ii,j)*(dkx(nk)+gx(ii))*(dkx(nk)+gx(j)) +
EPSy(ii,j)*(dky(nl)+gy(ii))*(dky(nl)+gy(j)))/4.d0/pi/pi;
                a(j,ii) = a(ii,j);
            end
        end
    end
end
end

```



```

    end
% Find the eignevalues
    v=eig(a);
    rr1(nk,nl)=sqrt(v(1));
    rr2(nk,nl)=sqrt(v(2));
    rr3(nk,nl)=sqrt(v(3));
    rr4(nk,nl)=sqrt(v(4));
    rr5(nk,nl)=sqrt(v(5));
    rr6(nk,nl)=sqrt(v(6));
end

end
% Plot the eignevalues
figure(1);
s1=contour(dkx,dky,rr1);
xlabel('k_x');ylabel('k_y');
title('H Band 1 square lattice a=0.3 d=1 ');
clabel(s1)
figure(2);
s2=contour(dkx,dky,rr2);
xlabel('k_x');ylabel('k_y');
title('H Band 2 square lattice a=0.3 d=1.0');
clabel(s2)
figure(3);
s3=contour(dkx,dky,rr3);
xlabel('k_x');ylabel('k_y');
title('H Band 3 square lattice a=0.3 d=1');
clabel(s3)
figure(4);
s4=contour(dkx,dky,rr4);
xlabel('k_x');ylabel('k_y');
title('H Band 4 square lattice a=0.3 d=1');
clabel(s4)
figure(5);
mesh(dkx,dky,rr1);
hold on
mesh(dkx,dky,rr2);
xlabel('k_x');ylabel('k_y');zlabel('a/\lambda');
hold on
mesh(dkx,dky,rr3);
xlabel('k_x');ylabel('k_y');zlabel('a/\lambda');

```

```

mesh(dkx,dky,rr4);
xlabel('k_x');ylabel('k_y');zlabel('a/\lambda');
title('H Bands anisotropic square lattice a=0.3 d=1');

```

Program 3 :

Groupvelocity calculation for 2D Anisotropic Square Lattice for H Pol. (PWEM)

```

N1 = 25;
pi = acos(-1.0);
d=1.;
a=0.5;
d1=1;
d2=1;
bbeta = pi*a*a/d1/d2;
EPSAx=2.55^2; % ROD DIELECTRIC x
EPSBx=1.64^2;% MATRIX DIELECTRIC x
EPSAy=2.2^2; % ROD DIELECTRIC y
EPSBy=1.62^2;% MATRIX DIELECTRIC y
etax=(1/EPSAx-1/EPSBx);
etay=(1/EPSAy-1/EPSBy);

% The major symmetry points in the Brillouin zone are defined
gxx = 0.0; gyg = 0.0;
gxx = 0.0; gyx = pi/d2;
gxm = pi/d1; gym = pi/d2;
% The itinerary around the brillouin zone is laid out.
gxi(1) = gxx; gyi(1) = gyx;
gxi(2) = gxg;
gyi(2) = gyg;
gxi(3) = gxm;
gyi(3) = gym;
gxi(4) = gxx;
gyi(4) = gyx;

%Construct the wave vectors used in the plane wave calculation
L=0;
gx1 = 2.0*pi/d1;
gy1 = 0;
gx2 = 0.0;
gy2 = 2.0*pi/d2;

```

% Generate all the wavevectors within a hexagon of diameter 2*n1.

```
for ii=-N1:N1;
    for j=-N1:N1;
        if ( -(N1+1)<(ii+j) & ((ii+j)<(N1+1))),
            L=L+1;
            gx(L) = gx1*ii + gx2*j;
            gy(L) = gy1*ii + gy2*j;
        end;
    end;
end;
L
```

% Construct the dielectric matrix

```
vcl = d1*d2;
for ii = 1:L;
    EPSx(ii,ii) = bbeta*1/EPsAx + (1.D0-bbeta)/EPsBx;
    EPSy(ii,ii) = bbeta*1/EPsAy + (1.D0-bbeta)/EPsBy;
end;

for ii=1:L;
    i1 = ii + 1;
    for j=i1:L;
        x1 = gx(ii) - gx(j);
        x2 = gy(ii) - gy(j);
        x = sqrt(x1*x1+x2*x2)*a;
        EPSx(ii,j) = 2.d0*etax*pi*a*a/(vcl) * besselj(1,x)/x;
        EPSy(ii,j) = 2.d0*etay*pi*a*a/(vcl) * besselj(1,x)/x;
    % The matrix is symmetric
        EPSx(j,ii) = EPSx(ii,j);
        EPSy(j,ii) = EPSy(ii,j);
    end;
end
```

% Use the itinerary constructed above to move around the Brillouin zone

```
n=L;
% Counter for the number of points in the itinerary
nmax=600;
kx(1) = 0.;
ky(1) = -1.1103 ;
```

```

ks=0.0025;
ddk=.0001;
dx(1)=0.; % center point
dy(1)=0.; % center point
dx(2)=ddk; % right point
dy(2)=0.; % right point
dx(3)=-ddk; % left point
dy(3)=0.; % left point
dx(4)=0.; % bottom point
dy(4)=-ddk; % bottom point
dx(5)=0.; % top point
dy(5)=ddk; % top point
for nk=1:(nmax-1);
for nl=1:5;
    dkx(nl)=kx(nk)+dx(nl);
    dky(nl)=ky(nk)+dy(nl);
    for ii=1:n;
        a(ii,ii) = (EPSx(ii,ii)*(dkx(nl)+gx(ii))^2 + EPSy(ii,ii)*(dky(nl)+gy(ii))^2)/4.d0/pi/pi;
%    if (ii<n)
        for j=ii+1:n;
            a(ii,j)=(EPSx(ii,j)*(dkx(nl)+gx(ii))*(dkx(nl)+gx(j)) +
EPSy(ii,j)*(dky(nl)+gy(ii))*(dky(nl)+gy(j)))/4.d0/pi/pi;
            a(j,ii)=a(ii,j);
        end
    end
% end
end
% Find the eignevalues
v=eig(a);
rr2(nl)=sqrt(v(2));
end
% gradient operator
gradx(nk)=(rr2(2)-rr2(3))/2/ddk;
grady(nk)=(rr2(5)-rr2(4))/2/ddk;
% unit vector perpendicular to the gradient operator;
mag(nk)=sqrt(gradx(nk)*gradx(nk)+grady(nk)*grady(nk));
hx=grady(nk)/mag(nk);
hy=-gradx(nk)/mag(nk);
% next wave vector along the isofrequency curve is calculated
kx(nk+1)=kx(nk)+ks*hx;
ky(nk+1)=ky(nk)+ks*hy;
omega(nk)=rr2(1);
nk=nk+1;

```

R702034943

```
end
    omega(nmax)=omega(1);

% Plot the eigenvalues
figure(1);plot(kx,ky);
xlabel('k_x');ylabel('k_y');title('isofrequency contour');
figure (2); plot(omega);
figure(3); plot(kx(1:nk-1),gradx./mag);grid;
```